The Pennsylvania State University

The Graduate School

College of Earth and Mineral Sciences

THE INFLUENCE OF CRYSTAL DEFECTS ON DOMAIN WALL MOTION IN THIN FILM $Pb(Zr,Ti)O_3$

A Dissertation in

Materials Science and Engineering

by

Daniel M. Marincel

Submitted in Partial Fulfillment
of the Requirements
for the Degree of

Doctor of Philosophy

December 2014

The dissertation of Daniel M. Marincel was reviewed and approved* by the following:

Susan Trolier-McKinstry
Professor of Ceramic Science and Engineering
Dissertation Advisor
Chair of Committee

Clive A. Randall
Professor of Materials Science and Engineering
Dissertation Co-advisor

Long-Qing Chen
Distinguished Professor of Materials Science and Engineering

Sergei V. Kalinin
Special Member
Center for Nanophase Materials Sciences
Oak Ridge National Laboratory

Qiming Zhang
Distinguished Professor of Electrical Engineering

Suzanne Mohney
Professor of Materials Science and Engineering and Electrical Engineering
Chair, Intercollege Graduate Degree Program in Materials Science and Engineering

*Signatures are on file in the Graduate School.

Abstract

This work describes the interactions of domain walls in ferroelectric $Pb(Zr,Ti)O_3$ with grain boundaries and PbO non-stoichiometry. This was studied for a variety of Zr:Ti ratios by analyzing the local piezoelectric response using band excitation piezoresponse force microscopy. Measurements were conducted on a variety of tilt and twist bicrystals with angles ranging from 10° to 30°. For the >15° tilt and ≥10° twist grain boundaries, a local minimum in the nonlinear response was observed at the grain boundary. The 10° tilt grain boundaries exhibited a maximum nonlinear response at the grain boundary.

Variations in the nonlinear response at a 24° tilt grain boundary was measured for three different Zr:Ti ratios. Films with a ratio of 20:80, far into the tetragonal regime, exhibited a complex distribution of nonlinear response alternating between low and high with distance from the grain boundary. Films with a ratio of 45:55 and 52:48, tetragonal and near morphotropic phase boundary rhombohedral, respectively, exhibited a minimum in nonlinear response at the grain boundary neighbored by a maximum in nonlinear response.

The nonlinear response was correlated to the domain structure. The domain structure was characterized before and after poling using piezoresponse force microscopy and transmission electron microscopy. It was found that the domain structure was controlled by the local strain and electric field for the largest angle grain boundaries. Domain walls were pinned at the grain boundary by the local strain and electric field. At 360-650 nm from the grain boundary, domain wall – domain wall interactions dominated the nonlinear response. A smaller width of reduced nonlinear response for the film with Zr:Ti ratio of 52:48 was attributed to enhanced relaxation of the local strain and electric field due to the small ~6 nm domain size.

Phase field models were used to determine the primary factors involved in forming domains at large angle tilt grain boundaries. The models suggest that domains form to minimize the local change in strain across the grain boundary, explaining correlated domain organization in neighboring grains previously observed by piezoresponse force microscopy and transmission electron microscopy. However, strain compatibility could not account for the observed formation of head to head domain structures observed at the grain boundary for $Pb(Zr_{0.2}Ti_{0.8})O_3$; it is believed that these are stabilized by built-in charge or additional stress compensation.

It was demonstrated that the pinning for 24° tilt angle grain boundaries influences domain wall motion over a longer lateral distance (0.45 – 0.80 μm) than 30° twist angle grain boundaries (~0.35 μm). Additionally, the pinning energy reduced with the grain boundary angle. The maximum in nonlinear response observed for small angle tilt grain boundaries ($\leq 10°$) was attributed to an increased concentration of low energy pinning sites reducing the reversible response and increasing the irreversible response. Similarly, minimal variation in the nonlinear response was observed at the grain boundary for intermediate grain boundary angles (15° tilt) due to the grain boundary energy being similar to other defects present in the film.

A furnace providing a controlled PbO atmosphere was developed so that the effect of PbO defects on the functional properties of $Pb(Zr,Ti)O_3$ could be determined. Minimal variation in the permittivity, Rayleigh parameters, and aging rates was observed for films with a range of PbO contents. A decreasing remanent polarization was observed with increasing PbO content in minor polarization – electric field hysteresis loops. An increase in the area of low nonlinear response regions with decreasing PbO content was measured by band excitation piezoresponse force microscopy. This suggests that PbO deficiencies act to reduce domain wall motion where it

is already low. It was determined that $V_{Pb}'' - V_O^{\cdot\cdot}$ defect dipoles, if they exist, have only a modest influence on domain wall motion compared to defects already present in the film.

This work helps to determine the mechanisms responsible for emergent properties in ferroelectric materials and, as such, provides a basis for superior models representing the functional properties of ferroelectric materials. The measurements of the effect of grain boundaries and PbO concentration on nonlinear response support the framework for the representations of mobile interfaces interacting with defects in materials. By correlating measurements by various characterization and modeling methods, a deeper understanding of ferroelectric materials is provided.

Table of Contents

List of Figures

List of Tables

Preface

Section 1.3 has previously been published in *Advanced Functional Materials*[1] as a part of a review paper entitled “Polarization dynamics in ferroelectric capacitors: Local perspective on emergent collective behavior and memory effects.” The section included was written by DMM and STM.

Chapter 2 has previously been published in *Advanced Functional Materials*.[2] Authorship includes D. M. Marincel, H. R. Zhang, A. Kumar, S. Jesse, S. V. Kalinin, W. M. Rainforth, I. M. Reaney, C. A. Randall, and S. Trolier-McKinstry.

Chapter 3 was written as a journal article and will be submitted for publication. Authorship on the paper will include D. M. Marincel, H. R. Zhang, J. Britson, A. Belianinov, S. Jesse, S. V. Kalinin, L. Q. Chen, W. M. Rainforth, I. M. Reaney, C. A. Randall, and S. Trolier-McKinstry.

Chapter 4 was written as a journal article and will be submitted for publication. Authorship on the paper will include D. M. Marincel, H. R. Zhang, S. Jesse, A. Belianinov, M. B. Okatan, S. V. Kalinin, W. M. Rainforth, I. M. Reaney, C. A. Randall, and S. Trolier-McKinstry.

Chapter 5 was written as a journal article and will be submitted for publication. Authorship on the paper will include D. Marincel, S. Jesse, A. Belianinov, M. B. Okatan, S. V. Kalinin, T. N. Jackson, C. A. Randall, and S. Trolier-McKinstry.

For all work, contribution was distributed as follows: DMM prepared the samples and conducted electrical and electromechanical characterization, TNJ consulted on PbO furnace design, HRZ conducted transmission electron microscopy, JB conducted phase field modeling,

DMM, AK, AB, MBO, SJ, and SVK conducted band excitation piezoresponse force microscopy, DMM, HRZ, SVK, WMR, IMR, CAR, and STM analyzed the data, DMM, HRZ, IMR, CAR, and STM wrote the articles, and SVK, IMR, and STM designed the project.

Acknowledgements

First, I would like to acknowledge the guidance and support I have received over the past four and a half years from my advisor, Professor Susan Trolier-McKinstry. The individual focus she manages to provide for every student and every research project astounds me. Not only was I fortunate enough to receive advice in terms of research, but her guidance in teaching provided me the opportunity to develop and improve my own teaching style. I would also like to thank my co-advisor, Professor Clive Randall, for his differing advising style. Whenever I was up against a wall and saw nowhere to go with research, he always provided an alternative, necessary view that helped develop new interpretations.

This work would not have been possible without the assistance of the scanning probe microscopy specialists at the Center for Nanophase Materials Sciences at Oak Ridge National Laborartory: Amit Kumar, Alex Belianinov, M. Baris Okatan, Stephen Jesse, and Sergei Kalinin. Thank you for your technical expertise and for helping me stay sane (and awake!) through the days, nights, and weekends so that data could be collected around the clock.

Collaboration with the transmission electron microscopy experts at the University of Sheffield raised this work to the next level by providing incredible micrographs and thoughtful analysis. Special thanks go to Huairuo Zhang, for his late night microscopy sessions, and Professor Ian Reaney, for his insightful skype discussions.

Conversations with people from other areas of expertise improved the quality of this research. The knowledge gained through discussions with Jason Britson and Professor Long-Qing Chen led to a phase field modeling component in this work.

A new piece of equipment was built for this research and, as always happens, would not have been successful without the support from various people. Professor Tom Jackson provided insight to help design the furnace, Chris Jabco in the Materials Research Laboratory machine shop and Russ Rogers from the Chemistry Building glassblowing shop provided parts for the furnace, Charlie Cole and Jake Lyons constructed a cabinet to safely contain the hazardous materials, Jeff Long helped to install interlocks, and David Sarge made sure there were no safety issues.

Technical support from the Materials Characterization Laboratory and the Nanofabrication facility made sure that the instruments were functioning properly and answered any questions I had. Special thanks go to Bill Drawl, Chad Eichfeld, Beth Jones, Tim Klinger, Jeff Long, and Derek Wilke.

Research is a collaborative process, with knowledge shared through conversation, and so I would like to thank the Trolier-McKinstry and Randall research groups for their assistance throughout the PhD process: Betul Akkopru Akgun, Seth Berbano, Srowthi "Raja" Bharadwaja, Jon Bock, Trent Borman, Jason Chan, Lyndsey Denis, Enkhee Dorjpalam, Lauren Garten, Flavio Griggio, Damoon Heidary, Raegan Johnson, Ryan Keech, Song Won Ko, Sun Young Lee, Russell Maier, Lizz Michael, Carl Morandi, Adarsh Rajashekhar, Dennis Shay, Smitha Shetty, Dan Tinberg, Margeaux Wallace, Aaron Welsh, Derek Wilke, Jung In Yang, Charley Yeager, and Hong Goo Yeo.

Finally, I would like to thank my family and close friends for keeping me going throughout this experience. My "family" at Penn State, Susie and Phil Sherlock and the gardening group, you are the ones who kept me going from day to day. Mom, Dad, Michelle,

Brian, Joe, and Steve, you have all kept me grounded in the real world. And last, thank you, Jordan, for supporting me from afar and helping me move forward in research and life.

Support for this work was provided by the National Science Foundation under grant DMR-1005771. The band excitation piezoresponse force microscopy was conducted at the Center for Nanophase Materials Sciences at Oak Ridge National Laboratory under user proposals CNMS 2011-022, CNMS2011-223, CNMS 2011-224, CNMS 2013-127, and CNMS 2013-249. The Center for Nanophase Materials Sciences is sponsored at Oak Ridge National Laboratory by the Scientific User Facilities Division, Office of Basic Energy Sciences, U.S. Department of Energy. Funding for the transmission electron microscopy work was provided by the Engineering and Physical Sciences Research Council EP/I038934/1. Phase field modeling was funded by the U.S. Department of Energy, Office of Basic Energy Sciences, Division of Materials Sciences and Engineering under Award FG02-07ER46417. Calculations at the Pennsylvania State University were performed on the Cyberstar Linux Cluster funded by the National Science Foundation through grant OCI-0821527.

Chapter 1: Introduction

1.1 Ferroelectric Materials

Ferroelectrics are a class of materials with a stable, reorientable polarization. The presence of a stable polarization necessitates a unique polar crystallographic axis. In addition, the polarization must be reorientable under a realizable electric field between equivalent crystallographically-defined directions.[3]

All ferroelectric materials have a unique polar axis. As such, they are also pyroelectric materials, meaning a change in temperature will result in a change in the magnitude of polarization. Out of the 32 crystallographic space groups, 10 are pyroelectric. These pyroelectric point groups permit odd-rank property tensors with non-zero terms, which includes the third rank piezoelectric property tensor. Therefore, all ferroelectric materials are allowed to exhibit a piezoelectric response.[4]

The direct piezoelectric effect entails a linear relationship between polarization P_i and an applied stress X_j, as $P_i = d_{ij}X_j$, where the piezoelectric coefficient is d_{ij} in matrix notation. Similarly, the converse effect relates strain x_i to electric field E_j, as $x_i = d_{ij}E_j$, with the same piezoelectric coefficient d_{ij}.[5] This is different from the electrostrictive coefficient Q_{ij} which relates strain to the square of the electric field, and is a fourth order tensor exhibited by all materials.[3]

Ferroelectric materials are a unique subset of pyroelectric materials for which the spontaneous polarization can be reoriented under a realizable electric field. This is represented by the ferroelectric polarization – electric field hysteresis loop, in which the polarization is

typically switched from –P to +P and back by an applied electric field. Hysteresis loops for ferroelectric materials are characterized by saturation of the polarization at high fields, at which point the material responds as a lower loss dielectric. Simply exhibiting hysteresis in polarization vs. electric field data without saturation is not sufficient to prove the material is ferroelectric, as conductive loss may also contribute to time-dependent charge accumulation.[6]

1.1.1 Domain Structure

Interaction of the spontaneous polarization with material surfaces and defects will result in an oppositely oriented electric field, or depolarization field, if the polarization is not compensated by charge accumulation (e.g. at an electrode). The depolarization field is generally strong enough to reorient the polarization locally and form regions with differently oriented polarization.[4] Regions with an (approximately) uniform polarization are called domains, while the boundary between two regions with different polarizations are called domain walls. Domain formation can also be driven by other sources of electric or elastic fields.[7]

In many ferroelectric materials, the polarization direction can be reoriented in more than two equivalent directions. The prototypical ferroelectric for such reorientation is the perovskite $BaTiO_3$. The perovskite structure is composed of a close-packed arrangement of oxygen and large cations (Ba^{2+}), with each large cation surrounded by 12 O^{2-} anions. Small, highly charged cations (Ti^{4+}) sit in the oxygen octahedral interstitial sites. At high temperatures, $BaTiO_3$ has a cubic structure, but upon cooling transitions to a tetragonal symmetry, followed by an orthorhombic symmetry, and finally by a rhombohedral symmetry.[3]

Each distortion from the cubic phase is accompanied by a spontaneous strain and a reorientation of the polar direction, associated with the relative displacement of the Ti^{4+} with

respect to the oxygen anions. In the tetragonal case, the cation displaces towards one oxygen anion, and is accompanied by a lengthening of the unit cell along the axis of displacement and a contraction perpendicular to the displacement[3] (see Figure 1.1). Because there are six equivalent directions for the cation to displace, if tetragonal $BaTiO_3$ cools in the absence of an electric field, Ti^{4+} will displace in different directions in different regions in order to minimize the depolarization and strain energy.[8] In general, a domain wall is described by the angle between the polarization directions it separates, such that domain walls can be 180° domain walls separating two regions with antiparallel polarizations, or non-180° domain walls separating two regions with polarization at some crystallographically defined angle <180°.[9]

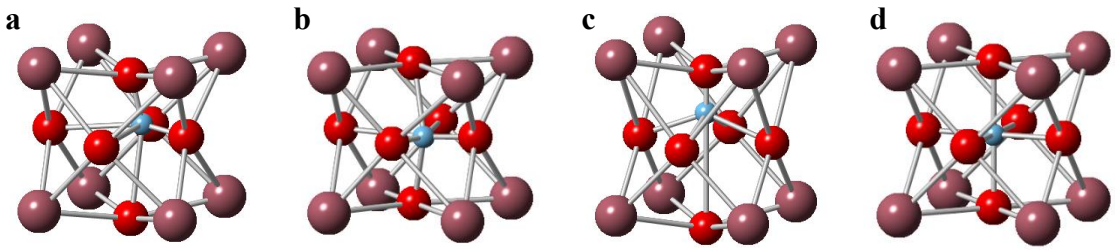

Figure 1.1: Ferroelectric distortions of $BaTiO_3$.

The ferroelectric distortions of $BaTiO_3$ from low temperature to high temperature. (a) Rhombohedral distortion, (b) orthorhombic distortion, (c) tetragonal distortion, and (d) cubic unit cell. The Ti^{4+} ion is in blue, the O^{2-} ion is in red, and the Ba^{2+} ion is in purple. All displacements from the cubic structure are multiplied by 5.[10]

When an electric field is applied, the domains with polarization nearly parallel to the electric field will grow at the expense of other regions. At low electric fields, only small domain wall displacements are typical, as the walls are often pinned on defects in the crystalline lattice. Domain wall motion contributes progressively to properties as the field amplitude is

increased.[11] As the electric field approaches the coercive field, sufficient energy is provided to nucleate and grow new domains, resulting in better alignment of the polarization with respect to the electric field. As the electric field is removed, some back-switching can occur. However, the predominance of domains stay aligned so that a net polarization is present at zero applied electric fields.[12]

Some ferroelectric materials, such as perovskites, also exhibit ferroelastic properties. Ferroelastic materials permit reorientation of a unique axis to another equivalent direction to accommodate an applied strain. Not all ferroelectric materials are ferroelastic; for example, ferroelectrics with the tetragonal tungsten bronze structure only permit 180° domain walls.[13] Similarly, not all ferroelastic materials are ferroelectric; martensites are ferroelastic but have no dipole moment.[14] The perovskite materials studied in this work exhibit both ferroelectric and ferroelastic properties.

1.1.2 Piezoelectric Constants and Permittivity

Ferroelectric materials exhibit enhanced permittivity and piezoelectric response relative to non-ferroelectric piezoelectrics. Typical values for the permittivity and piezoelectric constant d_{33} are reported in Table 1.1. Donor doping and the development of "soft" piezoelectric materials has been shown to enhance the domain wall contribution to ferroelectric response.[15]

Ferroelastic non-180° domain wall motion can significantly enhance the piezoelectric response of perovskite materials.[16] While the total piezoelectric d_{33} coefficient extrapolated to zero field is 461 pm/V for La-doped $Pb(Zr_{0.52}Ti_{0.48})$, reorientation of the polar axis by 90° accounts for 170 pm/V.[17] Similarly, movement of both 180° and non-180° domain walls can contribute significantly to the polarizability in the dielectric properties[18] and piezoelectric

response,[19] as discussed in more detail below. An improved understanding of mechanisms responsible for when domain walls contribute to the functional response will permit the design of superior materials.

Table 1.1: Property enhancement by domain wall motion.

Relative permittivity and axial piezoelectric coefficient for the non-piezoelectric SiO_2 glass, single crystal piezoelectric SiO_2 α-quartz (ε_{11}, d_{11}), and ceramic ferroelectrics $Pb(Zr_{0.52}Ti_{0.48})O_3$, hard $Pb(Zr,Ti)O_3$, and soft $Pb(Zr,Ti)O_3$ (ε_{33}, d_{33}).

Material	System	Permittivity (1 kHz)	Piezoelectric Coefficient (pC/N)
SiO_2 Glass	Linear Dielectric	3.8	n/a
SiO_2 Quartz[20]	Piezoelectric	4.5	–2.3
$Pb(Zr_{0.52}Ti_{0.48})O_3$[3]	Ferroelectric	730	220
Hard PZT-4[3]	Ferroelectric	1300	289
Soft PZT-5[3]	Ferroelectric	1700	374

1.2 Rayleigh Measurements

One method to analyze the contribution of domain wall motion to the functional properties of ferroelectric materials is the Rayleigh law. First applied to ferroelectric hysteresis by Boser[21] and to nonlinearity in permittivity and piezoelectric constant by Damjanovic and Demartin,[22] the Rayleigh law has become an essential method to describe the nonlinear dielectric and piezoelectric response of ferroelectric materials.[22] In the Rayleigh model, the dielectric and piezoelectric response are described by a reversible component, d_{init} and ε_{init}, and an irreversible component, α_d and α_e, which denotes the nonlinear response as a function of magnitude of an applied AC electric field as shown in Equations 1.1 and 1.2.

$$d = d_{init} + \alpha_d E_0 \qquad \text{Equation 2.1}$$

$$\varepsilon = \varepsilon_{init} + \alpha_e E_0 \qquad \text{Equation 2.2}$$

In this form, the initial permittivity and piezoelectric constant are attributed to the intrinsic response and the reversible movement of domain walls and phase boundaries, while the irreversible component is attributed to the motion of domain walls and phase boundaries across pinning centers in a potential energy landscape.[22]

The Rayleigh law directly relates variation in the permittivity and piezoelectric constant to hysteresis in the polarization and strain, respectively, as shown in Equations 1.3 and 1.4.

$$P = (\varepsilon_{init} + \alpha_e E_0)E \pm \frac{\alpha_e}{2}(E_0^2 - E^2) \qquad \text{Equation 1.3}$$

$$x = \left(d_{33,init} + \alpha_d E_0\right)E \pm \frac{\alpha_d}{2}(E_0^2 - E^2) \qquad \text{Equation 1.4}$$

For Equations 1.3 and 1.4, P is the polarization and x is the strain. In order to make sure that the Rayleigh law applies to a specific case, it is necessary to compare the actual polarization and strain loops to the fitted permittivity and piezoelectric constant collected at the same frequency and excitation field.[23]

The physical model for the Rayleigh law entails mobile interfaces (domain walls and phase boundaries) moving through a complex potential energy landscape under an applied field (see Figure 1.2 for a schematic representation). Local strains and electric fields due to defects in the crystal lattice apply forces on domain walls as represented by variations in the potential energy. Applied electric fields add a linear offset to the potential energy landscape. At low fields, domain walls *reversibly* oscillate around minima in the potential energy landscape. As the applied electric field increases, the domain wall may *irreversibly* move from one minimum to another.

The Rayleigh law holds in the case of a Gaussian distribution of restoring forces distributed randomly spatially throughout the material.[21] The absence of a Gaussian

distribution of pinning sources can result in non-Rayleigh behavior, as has been observed for acceptor doped ferroelectrics[24] and oxygen deficient $BaTiO_3$.[25] In the same way, a sublinear increase in permittivity with electric field has been shown for fine-grained $BaTiO_3$.[26] This was explained by a change in the potential energy landscape from closely spaced to widely spaced deep potential energy wells.[27]

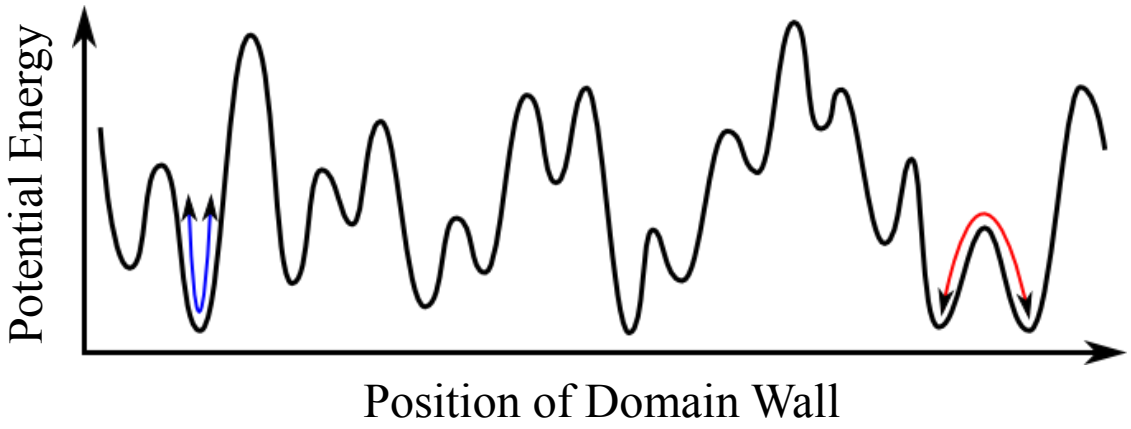

Figure 1.2: Complex potential energy landscape contributing to domain wall motion. Potential energy landscape for domain walls interacting with defects. The blue curve represents reversible domain wall motion, while the red curve represents irreversible domain wall motion.

Due to the progressive de-pinning and repining of the interface motion, domain walls have a time-dependent response. Specifically, as the frequency of the applied field increases, fewer domain walls are able to follow, and so their contribution to the properties is frozen-out. This is typically manifested as a logarithmic frequency dependence in the Rayleigh coefficients.[28] This frequency dependence of the Rayleigh parameters is not described in the original Rayleigh law, but appears to be characteristic of interface motion across randomly distributed defects.

The movement of non-180º domain walls generally dominates the piezoelectric extrinsic response due to the large spontaneous strains in ferroelectric materials. However, recent measurements indicate that the movement of 180º domain walls may also contribute to the piezoelectric response. Non-180º domain wall motion only appears in the odd powers of strain response to the electric field, while electrostriction contributes to the response that scales with the square of the electric field. Measurements of the second harmonic in the strain with electric field in some ferroelectric thin films have shown that the response is significantly higher than would be expected just for electrostriction. 180º domain wall motion can contribute to the second harmonic response and so account for the observed response.[19]

When measuring the Rayleigh response, it is essential that the domain structure is not significantly altered (e.g. by removal or introduction of domains) during the measurement. Thus, the Rayleigh law only applies within the regime where the permittivity and piezoelectric constant scales linearly with the ac electric field.[29] Typically, this range is up to ⅓ – ½ the coercive field.[30]

Rayleigh measurements have been used to quantify the effect of defects on domain wall motion in both bulk and thin film ferroelectric materials. The stability of any given domain structure is a strong function of the electrical and mechanical boundary conditions; these boundary conditions vary locally a function of the defect population. For thin-film ferroelectrics, defects affecting domain wall motion include substrate clamping,[31], [32] the dielectric-electrode interface,[33] point defects,[34]–[36] grain boundaries,[16], [37]–[39] domain wall-domain wall interactions,[40]–[42] aliovalent dopants,[43] dislocations,[33], [44] and stacking faults[45] (See Figure 1.3).

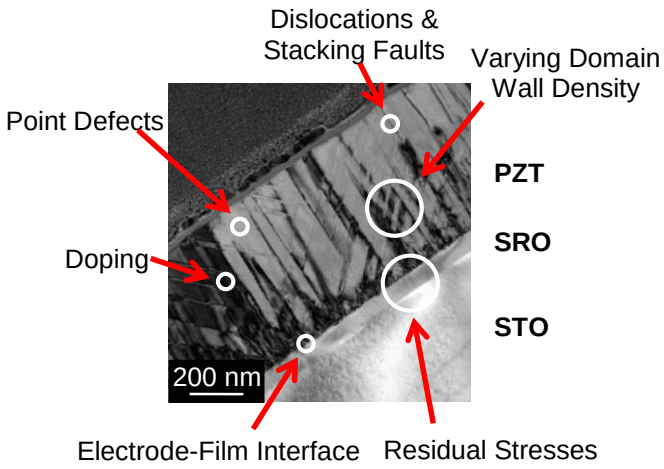

Figure 1.3: Defects influencing domain wall motion.

Bright Field TEM of epitaxial PZT 45/55 on SRO/STO showing various types of defects which may influence domain wall motion. Any variation from the ideal crystalline elastic or electric fields can influence domain wall motion. SRO – $SrRuO_3$, STO – $SrTiO_3$, and PZT 45/55 – $PbZr_{0.45}Ti_{0.55}O_3$

In magnetic materials, magnetization under a magnetic field occurs in a series of jumps, called Barkhausen noise. Physically, Barkhausen noise describes magnetization in multiple domains in avalanches, where neighboring regions are aligned due to a combination of the applied magnetic field and the local magnetic fields.[46] Many models of Barkhausen noise focus on the reorientation of domains as units rather than analyzing the motion of a domain wall as it moves across a single domain.[47] In fact, for ferroelastics there have been observations of barkhausen noise without observation of individual domain wall motion.[48]

1.3 Local Measurements of Domains and Domain Wall Motion

Although it is possible to determine the *average* influence of defects on domain wall motion by measurements of global properties, it is difficult to study the mechanisms involved in

pinning domain walls. It is essential to develop a mechanistic understanding of the emergent global response from the nanoscale polarization, domain structure, and domain wall pinning so that accurate models of the response of ferroelectric / ferroelastic materials under drive can be developed.[49], [50] Therefore, it is useful to employ characterization techniques that permit observation of the *local* response of domain walls near specific defects.

1.3.1 Piezoresponse Force Microscopy (PFM)

Piezoresponse force microscopy (PFM) is one method which permits local analysis of complex domain structures near specific defects. Traditional PFM has been used to study domain nucleation,[51] growth,[52]–[55] and pinning on specific defects[34], [56] with alternating write / read signals, although it can be difficult to remove topographic cross-talk.

Band excitation PFM (BE-PFM) techniques have recently been developed to minimize crosstalk and improve resolution at low excitation amplitudes.[57] The signal to noise ratio of scanning probe measurements is maximized at the resonance of the tip with the sample surface. However, the resonance frequency varies with topography, so attempts to collect amplitude and phase data with low excitation signal results in significant topographical crosstalk. BE-PFM involves exciting the material in a band of frequencies around resonance so that the piezoresponse can be measured at the resonance frequency at every point.[58]

1.3.2 Piezoelectric Nonlinearity: Reversible and Irreversible Motion of Domain Walls

Through the use of BE-PFM, it is possible to assess whether or not spatial correlation of domain wall motion occurs when measurements are made well *below* the sample coercive field (e.g. in the Rayleigh regime). Rayleigh measurements can be performed via BE-PFM when the

amplitude and phase of the surface deflection is measured as a function of the amplitude of the excitation voltage. The measured response amplitude, A_{max} is related to the excitation voltage V_{ac}, as $A_{max} = a_1 + a_2 V_{ac} + a_3 V_{ac}^2$, where the amplitude is proportional to the surface displacement h, such that $A_{max} = \beta h$. Here, β describes the transfer function of the cantilever. Differentiating with respect to V_{ac} and converting to electric field, E_{ac}, yields the Rayleigh law $\beta d_{33,f} = \beta d_{33,init} + \beta \alpha_d E_{ac}$ where $\beta d_{33,init} = a_2$ and $\beta \alpha_d = 2a_3 t$ and film thickness is t. The local nonlinearity is then $2a_3 t / a_2 = \alpha_d / d_{33,init}$. Notably, this parameter is independent of the cantilever properties,[59][1] and hence can be measured quantitatively.

Nonlinearity measurements following the Rayleigh law quantify the motion of domain walls at subcoercive fields, rather than domain nucleation. Measurements are made on poled and aged samples in order to achieve a strong response under small drive fields. Because the response under a well-defined electric field is essential for comparison to macroscopic measurements, a capacitor structure with the signal applied between top and bottom electrodes is employed, using the PFM tip as a sensor to measure vertical displacement.

1.3.3 Mechanical Nonlinearities in the Tip-Surface Junction

Although the intent of PFM studies is to characterize the nonlinear *material response* as a means of probing domain wall motion, the measured nonlinearity is a combination of both the material response and cantilever dynamics. Hysteresis in the resonance frequency of the cantilever tip in contact with the sample surface with increasing voltage and sweep direction is characteristic of nonlinearities arising from the cantilever dynamics. It was found in BE-PFM

[1] Note that the factor of two is missing in the equation in Bintachitt et al. (Ref [59]) though the data were calculated correctly.

measurements that dynamic nonlinearities suppress the maximum amplitude for increasing frequency with time, or chirp up, and amplify the maximum amplitude and decrease the resonant frequency for decreasing frequency with time, or chirp down, as indicated in Figure 1.4.[60]

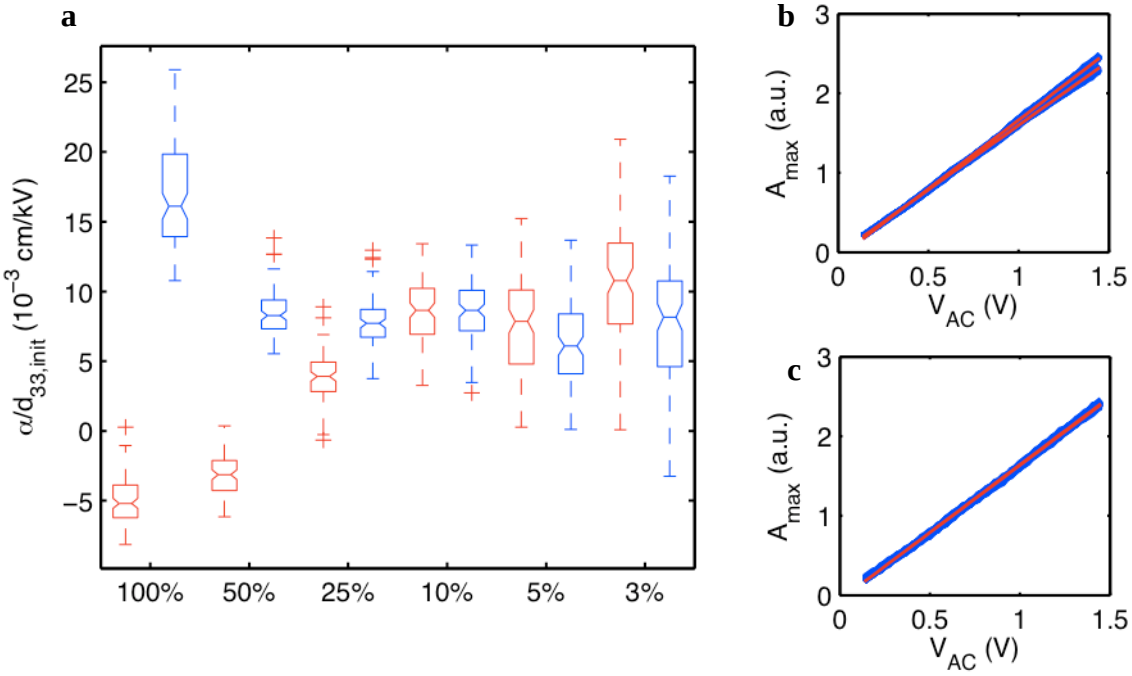

Figure 1.4: Tip surface nonlinearity.

Piezoelectric nonlinearity measurements on a PZT film with top and bottom electrodes. (a) Box plot of the distribution of nonlinearity as a function of percent chirp character of the excitation signal, with the increasing frequency sweep in red and the decreasing frequency sweep in blue. Signals with high chirp character show large tip surface nonlinearities, while signals with high sinc character show low signal to noise ratio. (b,c) Amplitude of the response as a function of excitation voltage for signals with 50% (b) and 10% (c) chirp character. The response of each of the 100 measurements is shown in blue with the average linear response for chirp up and chirp down in red. Differences in the red lines indicate tip surface nonlinearities.

In order to measure the material nonlinear response, the nonlinearity due to cantilever dynamics, and hysteresis in the resonance frequency with sweep direction, must be minimized. The nonlinearity due to the cantilever dynamics is a function of the energy of the excitation signal. Therefore, it is possible to minimize the nonlinearity by minimizing the energy of the excitation signal. This can be achieved by using a pure sinc function (i.e. well-localized in time) for the excitation. However, the signal to noise ratio decreases with increasing sinc character and increases with an increasing chirp character, so a balance must be found where sufficient signal to noise is achieved while minimizing the tip nonlinearities. In this manner, the nonlinearity associated with the ferroelectric material will exceed the nonlinearities associated with the tip – top electrode mechanics.

It has further been shown that when BE-PFM measurements are made on a capacitor structure, the optimal energy of the excitation signal is constant across a single electrode and does not depend on the position on the electrode. Because the necessary excitation signal will not vary between regions in the test area, it follows that the measured nonlinearity due to the piezoelectric response of the material is quantitative and local.

1.3.4 Domain Wall Motion in Ferroelectric Capacitors at Subcoercive Fields

The local nonlinear piezoelectric response was first observed via PFM by Bintachitt et al.[59] in $PbZr_{0.52}Ti_{0.48}O_3$ (PZT) ferroelectric films clamped on a Pt-coated Si substrate. In this study, micron-sized regions with high nonlinear response were observed in a matrix of lower nonlinear response (see Figure 1.5). This observation of local nonlinearity proves that small volumes of ferroelectric material exhibit Rayleigh behavior. The clusters of high nonlinear response were attributed to local regions of less strongly pinned domain walls than in the matrix.

It is intriguing that the cluster size significantly exceeded either the grain or domain size in those films (similar to the SSPFM studies), as will be discussed below.

Variation in the clusters of nonlinear response was observed with a change in thickness of the films, as shown in Figure 1.5(b). Films thicker than 2 μm showed uniform nonlinearity. This was attributed to the measured response averaging over a larger sample volume such that individual clusters could not be identified. It was estimated that the density of regions of high nonlinear response for these polycrystalline PZT films was on the order of 1 per μm^3 such that the response appears homogeneous when the resolution is above 1 μm^3, as was the case for the thicker films.[61] In thinner films, clusters of high nonlinear response were observed in a matrix of low nonlinear response, with the density of high response regions decreasing with film thickness. Finally, in the thinnest film the electromechnical nonlinearity was uniform and essentially zero. This evolution agreed with the observation of a decreasing global dielectric nonlinearity with decreasing thickness below 1-2 μm.[62]

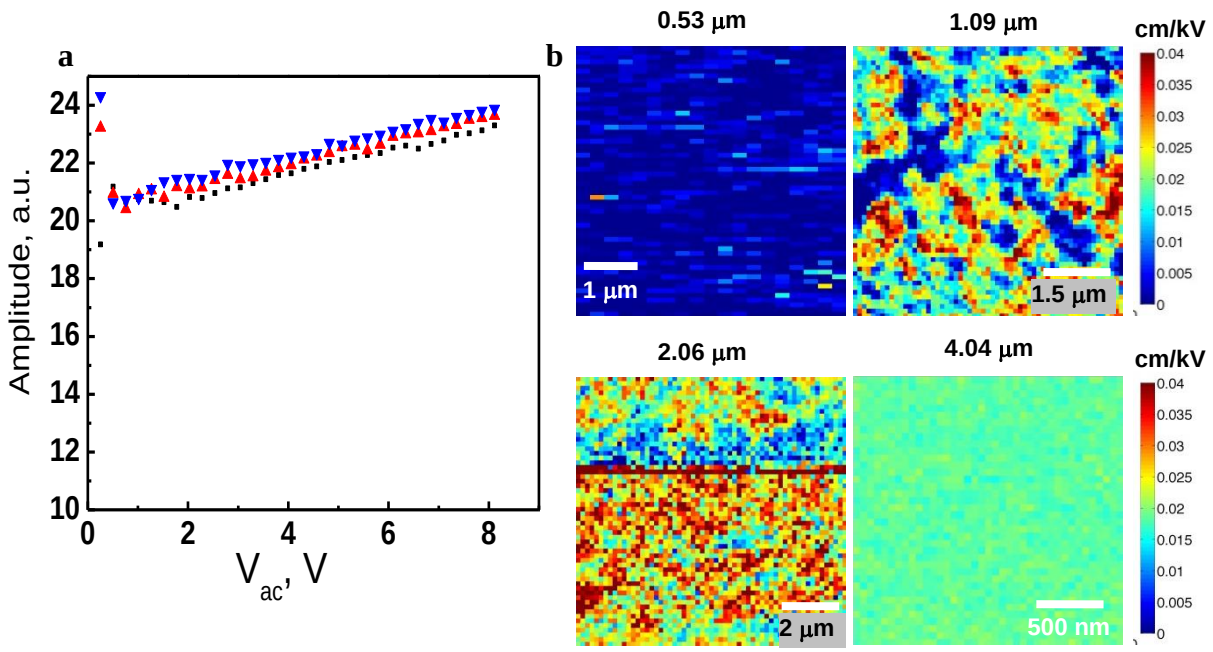

Figure 1.5: Piezoelectric nonlinearity in polycrystalline PZT films with top and bottom electrodes.

(a) Field dependence of $d_{33,f}$ in a 4 micron thick sample, (b) maps of the piezoelectric nonlinearity in PZT films of different thickness. Adapted and reprinted with permission from *Bintachitt* et al.[59] Copyright PNAS (2010).

The observed regions of high nonlinearity were interpreted as the cascading movement of domain walls[63] due to the motion of one wall imposing an effective pressure on walls within an interaction volume. Furthermore, the cluster size observed was much larger than the grain size of the material,[59] leading to the interpretation that there is a strong correlation of domain wall movement between grains. It is intriguing that the observed clustering of high nonlinear response in the 1.09 μm thick sample in Figure 1.3 (on the order of ~0.5-2 μm laterally) is comparable to the regions of correlated switching in higher field measurements on similar films.[64] These two findings suggest that there is a correlation between regions of high nonlinear response and

regions of correlated switching, indicating a similar mechanism is responsible for both, namely the simultaneous displacement of interacting domain walls across regions with reduced pinning.

One of the key points made in the initial paper on nonlinearity measurements by Bintachitt et al.[59] is a similarity between the global dielectric nonlinearity and the local piezoelectric nonlinearity measurements. However, in other experiments,[31], [65] the local piezoelectric nonlinearity was much reduced relative to the global dielectric nonlinearity for clamped films. It is noteworthy that the sample analyzed by Bintachitt et al.[59] was randomly oriented and finer-grained while the samples analyzed by Griggio et al.[31], [65] were textured. The difference in dielectric and piezoelectric nonlinearities was attributed to a difference in the population of domain walls which contributes to the irreversible component of the dielectric and piezoelectric properties. In addition, regions with negative nonlinearity observed in the textured samples, which were attributed to hard local behavior, also decrease the average piezoelectric nonlinearity.

1.3.5 Role of Mechanical Boundary Conditions

Because ferroelectric materials undergo a spontaneous strain upon polarization, they are typically ferroelastic as well. As such, it is not surprising that the observed domain state and domain wall mobilities in ferroelectric films depend on the mechanical boundary conditions experienced by the sample. Numerous observations have been reported on increases in response associated with more mobile domain structures on laterally relieving the clamping associated with the substrate.[32], [66]

Mechanical clamping can also be reduced by changing the sample geometry from a film to a nanotube. Bharadwaja et al.[67] and Bernal et al.[68] both reported fabrication of PZT-based

nanotubes using Si and soft templates respectively. The former group demonstrated that the ratio of the irreversible to the reversible dielectric Rayleigh constants was larger for the nanotube than for a thin film of the same thickness. Comparable results were obtained by Bernal et al. using PFM to probe the response along the length of the nanotube wall.

Recently, the influence of reduction in substrate clamping on the lateral extent of correlated domain wall motion was also reported using released diaphragm structures.[31] The sample studied was an oriented PZT morphotropic phase boundary film, released by an isotropic XeF_2 dry-etch step in a circular pattern under the electrode. Local BE-PFM measurements were taken on the clamped region, the released region, and the interfacial region on the same capacitor structure. As in other measurements on clamped regions, strong clustering of regions of high nonlinear response was observed in the clamped region on this sample. However, the nonlinear response was substantially more uniform in the released regions (particularly well away from the clamped boundary), as shown in Figure 1.6. Indeed, the spatial average of $\alpha_d/d_{33,init}$ increased

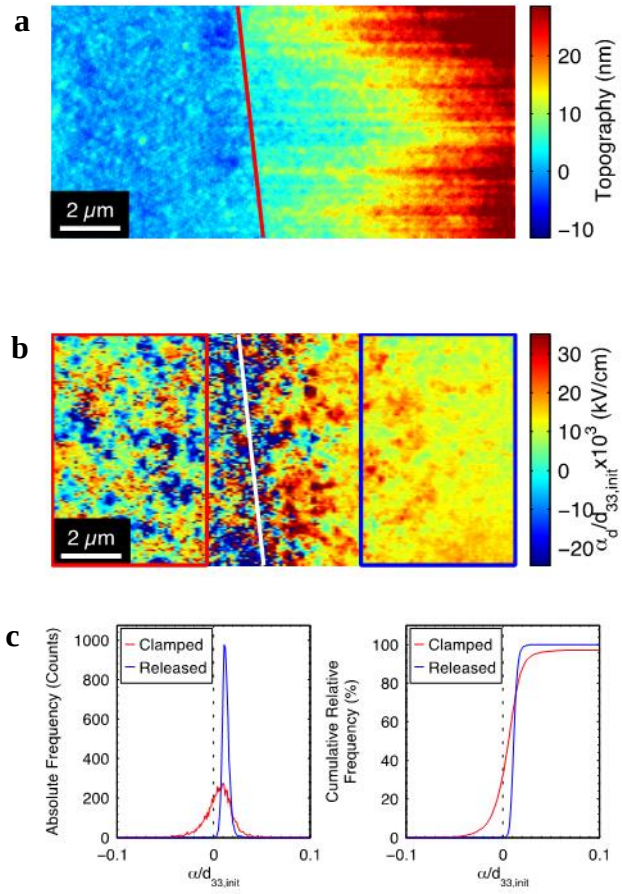

Figure 1.6: The role of clamping on nonlinear response.

Released diaphragm structure topography (a), the red line shows the edge of the released region. To the left of the line, the film is clamped to the underlying Si substrate; right of the line, the sample is released by undercutting the Si. (b) Nonlinear response, $\alpha_d/d_{33,init}$; the white line shows the edge of the released region, the bounding red and blue boxes are the regions used for histograms. (c) Absolute frequency and cumulative frequency histograms of clamped and released regions, showing narrower distribution and higher average nonlinear response in the released region relative to clamped region. These data are similar to those from Griggio et al.,[31] but arise from a separate measurement.

from 0.005 ± 0.015 cm/kV in the clamped region to 0.013 ± 0.003 cm/kV in the released region with a much tighter distribution of nonlinearity in the released region.

Dielectric measurements were also acquired for the released region for global dielectric measurements on fully clamped structures, released structures, and released and broken structures. The released structures had reduced local stresses at the film-substrate interface, while the released and broken regions also experienced a change in the average tensile stress in the film due to differences in the thermal expansion of the film and substrate. Significant increases in dielectric nonlinearity were observed for the broken diaphragm structures.

The increase in the local piezoelectric nonlinear response on undercutting the substrate was attributed to a greater mobility of domain walls, which was further corroborated by frequency dispersion measurements of the global dielectric nonlinearity.[31] For the clamped capacitors, α_e exhibited greater frequency dependence than the released capacitors, indicating that a greater portion of the irreversible domain wall motion freezes out at higher frequencies. Also, ε_{init} for the clamped capacitors exhibited a lesser frequency dependence than the released capacitors, indicating a greater contribution from reversible domain wall motion.

The narrower distribution of nonlinear response for the released region and the loss of clustering were attributed to an increase in the length scale for correlated motion of domain walls. Taking into account a greater number of domain walls moving irreversibly with a greater length scale for correlated movement, it is clear that clamping at the ferroelectric-substrate interface provides strong pinning sites. The pinning was attributed to a combination of a partial release of the average tensile stress due to the difference in thermal expansion of the film and substrate and also a release of local stresses due to the substrate rigidity. During domain formation, deformation strains can couple mechanically with the substrate rigidity, producing a

local stress at the ferroelectric-substrate interface, which can be expected to influence domain wall mobility. Therefore, reduction of these local stresses may remove strong pinning sources and lead to a much greater correlated movement of domain walls over an increased length scale. Further strengthening the above observations, it was found that the global dielectric irreversible coefficient of the released and broken capacitor was 27.2 ± 0.07 cm/kV, approaching values similar to undoped morphotropic phase boundary ceramics.[31]

1.4 Dissertation Organization and Statement of Goals

The influence of nanoscale defects becomes increasingly important with device miniaturization. Unexpectedly, in ferroelectric materials the degradation of functional properties is observed at the characteristic length of the order of microns, well above those expected from atomistic considerations and crucially important for downscaling of sensors, actuators, and memory devices. This dissertation provides a correlative study of nonlinear behavior in ferroelectrics using artificially engineered single defects.

The interaction of domain walls with a 24° tilt grain boundary in $Pb(Zr_{0.45}Ti_{0.55})O_3$ is presented in Chapter 2. Background knowledge and methodology are developed to assist in probing structure-property relationships at grain boundaries. This analysis is extended to 24° tilt grain boundaries in $Pb(Zr_{0.2}Ti_{0.8})O_3$ and $Pb(Zr_{0.52}Ti_{0.45})O_3$ in Chapter 3 and 10° tilt, 15° tilt, 10° twist, and 30° twist grain boundaries in $Pb(Zr_{0.45}Ti_{0.55})O_3$ and $Pb(Zr_{0.52}Ti_{0.45})O_3$ in Chapter 4. The chapters illustrate how grain boundaries influence domain structure and that domain wall – domain wall interactions dominate the nonlinear piezoelectric response. These studies further provide an example of emergent mesoscopic behavior and successful elucidation of its underpinning mechanisms.

Chapter 5 presents the development of a PbO – atmosphere rapid thermal annealing furnace and a study on the role PbO content plays on the local and global properties. A combination of global piezoelectric and dielectric measurements, and local piezoelectric nonlinearity measurements assist in determining what role $V_{Pb}'' - V_O^{\cdot\cdot}$ defect dipoles have on the functional properties of ferroelectric PZT.

Conclusions regarding domain wall motion near grain boundaries and with respect to PbO content are provided in Chapter 8. Proposed future works are also provided with preliminary results of an attempt to probe the relationship between domain structure and nonlinear response.

Chapter 2: Influence of a Single Grain Boundary on Domain Wall Motion in Ferroelectrics

Epitaxial tetragonal 425 and 611 nm thick $Pb(Zr_{0.45}Ti_{0.55})O_3$ (PZT) films were deposited by pulsed laser deposition on $SrRuO_3$-coated (100) $SrTiO_3$ 24º tilt angle bicrystal substrates to create a single PZT grain boundary with a well-defined orientation. On either side of the bicrystal boundary, the films showed square hysteresis loops and had dielectric permittivities of 456 and 576, with loss tangents of 0.010 and 0.015, respectively. Using Piezoresponse Force Microscopy (PFM), a decrease in the nonlinear piezoelectric response was observed in the vicinity (720-820 nm) of the grain boundary. This region represents the width over which the extrinsic contributions to the piezoelectric response (e.g. those associated with the domain density/configuration and the domain wall mobility) are influenced by the presence of the grain boundary. Transmission electron microscope (TEM) images collected near and far from the grain boundary indicated a strong preference for (101)/($\bar{1}$01) type domain walls at the grain boundary, whereas (011)/(0$\bar{1}$1) and (101)/($\bar{1}$01) were observed away from this region. It is proposed that the elastic strain field at the grain boundary interacts with the ferro-electric/elastic domain structure, stabilizing (101)/($\bar{1}$01) rather than (011)/(0$\bar{1}$1) type domain walls which inhibits domain wall motion under applied field and decreases non-linearity.

2.1 Introduction

One key open problem in the field of ferroelectrics is the way in which domain walls interact with local pinning centers, and the length scale over which defects influence the

response. Point, line, and area defects (and, in principle, any source of local electric or elastic fields) can act as pinning sites for domain wall motion and can lead to nonlinearity coupled with hysteresis in the dielectric and piezoelectric response at sub-switching applied electric fields.[18], [27], [33], [69]–[71] However, the quantitative influence of specific pinning sites on the measured dielectric and piezoelectric nonlinearities is currently unknown. The approach taken here is to utilize the piezoelectric response[59], [60] to study the way in which the nonlinear response develops across a single, well-defined grain boundary.

There are previous reports on the collective influence of grain boundaries on the observed domain structure and domain wall mobility of ferroelectrics. For example, coupling of domain structure across grain boundaries has been observed in TEM micrographs of lead zirconate titanate ceramics [72] and lead titanate thin films [73] as a result of long-range electric and elastic fields. Phase field simulations of domain structures in polycrystalline materials show coupling of domains across grain boundaries [37] with switching in one grain propagating to a neighboring grain.[49] It has also been shown by computational modeling that 90º domain walls prefer not to intersect certain types of grain boundaries, but tend to have nearly parallel polarization orientations on either side of the grain boundary.[74]

From the standpoint of functional properties, grain boundaries are known to influence the ensemble dielectric and piezoelectric response. Damjanovic and Demartin showed for $BaTiO_3$ ceramics that a decrease in the irreversible contribution to the direct piezoelectric response resulted from a decrease in the grain size,[16] indicating that grain boundaries act to pin domain walls.[75] In polycrystalline PNN-PZT films, a similar decrease was shown in the nonlinear contribution to permittivity with decreasing grain size.[76] Calculations made using first-principles density functional theory also indicate that pinning of domain walls at grain

boundaries is energetically favorable.[50] It was further shown experimentally that domain walls do not easily move over grain boundaries at low fields.[77], [78]

In addition, phase field models indicate that domains preferentially nucleate at grain boundaries upon back-switching.[37], [49], [74] In general, back-switching tends to occur by initial nucleation of 90º domains in one grain to decrease the local electrical energy density, followed by propagation into neighboring grains.[49] Local switching by PFM further indicates that domain nucleation may be preferred at grain boundaries.[79] If grain boundaries act only as strong pinning sites, there will be a low irreversible contribution to the piezoelectric and dielectric response near the boundaries due to reduced domain wall motion. However, if domains nucleate at grain boundaries upon back-switching, the concentration of domain walls interacting with weaker pinning sites would increase, leading to an increase in the irreversible contribution to the piezoelectric and dielectric response.

Recent developments of local measurements for piezoelectric response offer the opportunity to follow the evolution of the macroscopic response.[31], [80]–[82] Characterization of both polycrystalline and epitaxial films demonstrates complex domain structures by band excitation piezoresponse force microscopy revealing clusters of high nonlinear response with sizes larger than the average grain or domain size. Thus, there must be cooperative movement of domain walls across grain boundaries.[59]

One of the consequences of domain wall motion coupling across grain boundaries is that previous studies have sampled multiple pinning centers in their measurements. To better understand the influence of any single pinning site to the response, new data are required which isolate the influence of a single defect on the observed response. Specifically, in this contribution the role of an individual grain boundary is considered.

2.2 Materials & Methods

Bicrystal (100) $SrTiO_3$ substrates, 5 mm diameter and 0.5 mm thick, with a tilt angle of 24º (MTI Corp.) were used to engineer a single grain boundary at a known, well-defined angle in a ferroelectric film. Epitaxial $SrRuO_3$ bottom electrodes were deposited on the $SrTiO_3$ substrates by pulsed laser deposition (PLD) using a KrF excimer 248 nm laser (Lambda Physik Compex Pro), as described elsewhere.[83] This was followed by depositing PZT by PLD from a target batched at a Zr/Ti ratio of 45/55 with 20% excess PbO. PZT films were deposited on the bicrystal substrates with multiple thicknesses to determine whether the range of influence of a grain boundary on piezoelectric nonlinear response is thickness dependent. The results reported are for representative samples with thicknesses of 611 nm and 425 nm (Tencor 500 Contact Profilometer). Deposition conditions are provided in Table 2.1. A schematic of the sample is shown in Figure 2.1.

Table 2.1: Pulsed laser deposition conditions.

Conditions for pulsed laser deposition of $SrRuO_3$ and $Pb(Zr,Ti)O_3$.

Composition	Pressure [mTorr]	Temperature [ºC]	Substrate Distance [cm]	Laser Energy [J cm^{-2}]	Repetition Rate [Hz]	# Pulses
$SrRuO_3$	160	680	8	1.1	10	600
$Pb(Zr,Ti)O_3$	100	630	6	1.2	10	18000/7800

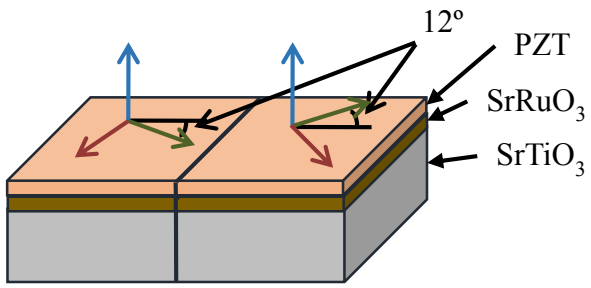

Figure 2.1: 24° Tilt $SrTiO_3$ with epitaxial $SrRuO_3$ and PZT films.

Schematic of samples used for studying the role of a 24° grain boundary on domain wall motion in PZT thin films.

Photolithography followed by sputter deposition of platinum (Kurt Lesker CMS-18) 10 nm (611 nm thick PZT film) or 50 nm (425 nm thick PZT film) thick was used to define capacitors across the grain boundary so that PFM measurements could be made with a well-defined electric field. Alternating exposure to buffered oxide etchant and HCl was used to etch through the PZT to expose the $SrRuO_3$ bottom electrode, followed by sputter deposition of Pt on the exposed $SrRuO_3$ to improve adhesion for wirebonding to the bottom electrode. Samples were packaged (Spectrum Semiconductor Materials, Inc., CCF04002) on a silicon spacer so that the top of the sample was flush with the top of the package. A Kulicke and Soffa Industries, Inc. wedge wirebonder with gold wire was used to make electrical connections between the sample electrodes and the package (see Figure 2.2).

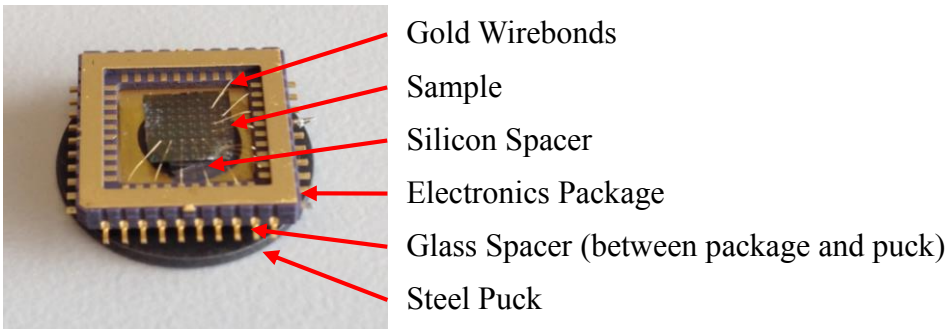

Figure 2.2: Picture of wirebonded sample prepared for BE-PFM measurements.

Packaged and wirebonded sample. Sample is mounted by silver paste on a silicon spacer on the bottom of the package. The package is super glued to a glass spacer on a steel puck.

Electrical measurements of capacitance and dielectric loss (HP 4284A Precision LCR Meter) were made at low field (30 mV, 10 kHz) and as a function of *ac* voltage up to 50% of the coercive voltage (½V_c) at 300 kHz, near the frequencies used in BE-PFM, to determine the dielectric nonlinearity. Polarization vs. voltage measurements were made using a Radiant RT-66 system to assess the ferroelectric hysteresis behavior.

BE-PFM measurements were conducted at the Center for Nanophase Materials Science at Oak Ridge National Laboratory using an Asylum Research Cypher with platinum-coated silicon tips (Nanosensors PPP-EFM-50) as described previously.[31], [59], [60], [65] In this work, the signal was applied to the bottom electrode, while the top electrode and the tip were grounded. Samples were poled at 8xV_C for 15 minutes and aged for 30 minutes prior to measurement. Maps were collected across the grain boundary at a pixel size of 50 or 30 nm and approximately 0.5 mm from the grain boundary at a pixel size of 50 nm.

In order to increase the amplitude of the piezoelectric strain, measurements by BE-PFM were made to 18 kV/cm (~0.5 V_C), beyond the electric field associated with the Rayleigh-like regime exhibited by electrical measurements (~5.2 kV/cm). Because measurements were made

beyond the Rayleigh regime, reported values for nonlinear response are simply the ratio of the quadratic to linear coefficients from the amplitude of response as a function of electric field, or $\frac{1}{2}\alpha_d/d_{33,init}$, in units of cm/kV, rather than the ratio of the irreversible (α_d) to reversible ($d_{33,init}$) components from the Rayleigh law. Clustered regions of high and low nonlinear response are evident in all maps, as has been observed previously.[31], [59], [60], [65] The clusters of high nonlinear response were defined as the regions having nonlinearity above the mean film nonlinearity by more than half a standard deviation, with cluster size off-boundary reported as equivalent circular diameters. A similar analysis was performed to determine regions of low nonlinear response.

Transmission electron microscopy was conducted by Huairuo Zhang and Ian Reaney of the University of Sheffield to observe the domain structure near the grain boundary. It has been reported in PZT that the surface domain configuration may be altered by mechanical grinding.[84], [85] Therefore, to avoid domain reorientation during specimen preparation, a dual beam FIB/SEM FEI Quanta 3D 200 machine was employed to prepare transmission electron microscope (TEM) specimens. The grain boundary of the bicrystal was initially located by scanning electron microscopy (SEM), then both cross-section and plan-view TEM specimens containing the grain boundary were prepared by focused ion beam (FIB). A field emission JEOL 2010F TEM/STEM and a JEOL 2010 TEM with Gatan 925 double tilt rotation analytical holder both operated at 200 kV were employed for TEM characterization.

2.3 Results

X-ray diffraction (Philips Pro MRD) showed phase pure PZT in a tetragonal perovskite structure. A phi scan on the PZT 101 peak confirmed epitaxy on both sides of the bicrystal grain

boundary. Rocking curves were measured for both samples, with a full width at half maximum of 0.76º in ω for the 611 nm thick film and 0.60º in ω for the 425 nm thick film.

Electrical measurements of the 611 nm thick sample made on electrodes off the grain boundary showed a well-saturated P-E hysteresis loop with remanent polarization of 41.6 $\mu C/cm^2$ and low-field permittivity of 576 with a loss tangent of 0.015. Analysis of the dielectric nonlinearity at 300 kHz after poling showed Rayleigh-like response up to 5.3 kV/cm with a reversible component of 480.2±0.2 and an irreversible component of 7.16±0.07 cm/kV, giving an irreversible/reversible ratio of 14.9±0.2 $x10^{-3}$ cm/kV. All dielectric Rayleigh parameters are reported in Table 2.2. The 425 nm thick sample showed similar results, with a well-saturated P-E loop with remanent polarization of 41.0 $\mu C/cm^2$ and low-field permittivity of 456 with a loss tangent of 0.010. Analysis of the dielectric nonlinearity at 300 kHz after poling showed Rayleigh-like response up to 5.2 kV/cm with a reversible component of 428.0±0.2 and an irreversible component of 6.79±0.05 cm/kV, giving a total irreversible/reversible ratio of 15.9±0.1 $x10^{-3}$ cm/kV. Comparison of global measurements made on electrodes containing the boundary to those far from the boundary revealed no variation in Rayleigh character, dielectric loss, or dispersion, leading to the necessity for local measurements.

Table 2.2: PZT 45/55 Rayleigh parameters.

Dielectric Rayleigh parameters for PZT 45/55 on electrodes crossing the grain boundary.

Sample Thickness	ε_{init}	α_e (cm/kV)	$\alpha_e/\varepsilon_{init}$ (10^{-3} cm/kV)
611 nm	480.2±0.2	7.16±0.07	14.9±0.2
425 nm	428.0±0.2	6.79±0.05	15.9±0.1

Local measurements of the piezoelectric nonlinearity using BE-PFM were made across and far to either side of the boundary. Figure 2.3 shows the topography, resonant frequency, and

phase collected at each point on the 5 µm x 5 µm region on the 425 nm thick sample. The resonant frequency for each region measured varies at most by 6 kHz at the grain boundary, which is < 2% of the resonant frequency. Such a low variation in resonant frequency at the grain boundary indicates that there was no significant topographical contribution to the nonlinearity measurement or variations in elastic properties. The low variation in phase shown in Figure 2.3(c) is characteristic of measurements taken after adequate poling.

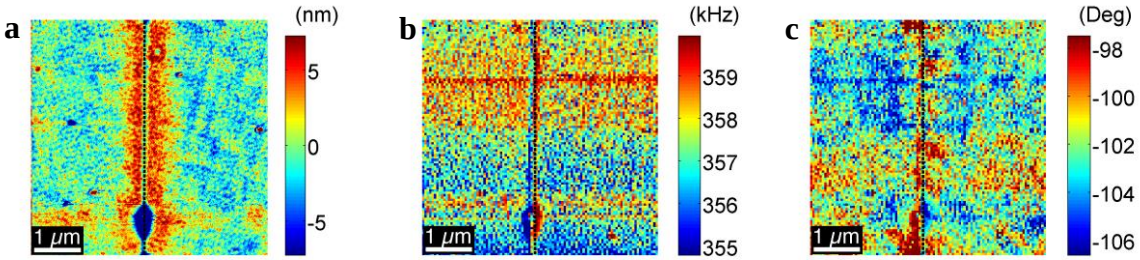

Figure 2.3: BE-PFM on PZT 45/55 across a 24° grain boundary.

Maps collected on 425µm thick sample across boundary on the 5µm x 5µm region: (a) topography, (b) resonant frequency, and (c) phase of signal at resonance. The dotted line denotes the grain boundary.

As a first approach, the data at each location were treated using the Rayleigh formalism. All maps collected across the grain boundary show a significant decrease in the nonlinear response at the boundary as seen in Figure 2.4(a-c), demonstrating that the boundary serves as an effective pinning site. The reduced response at the grain boundary had an average width for the 611 nm thick film of 834±67 nm, while the reduced response for the 425 nm thick film is 722±56 nm averaged across the 5 µm map and 755±48 nm averaged across the 3 µm map. The results shown here are representative of observations from many measurements made under

various poling conditions, indicating that this observed decrease is consistent for grain boundaries of this type.

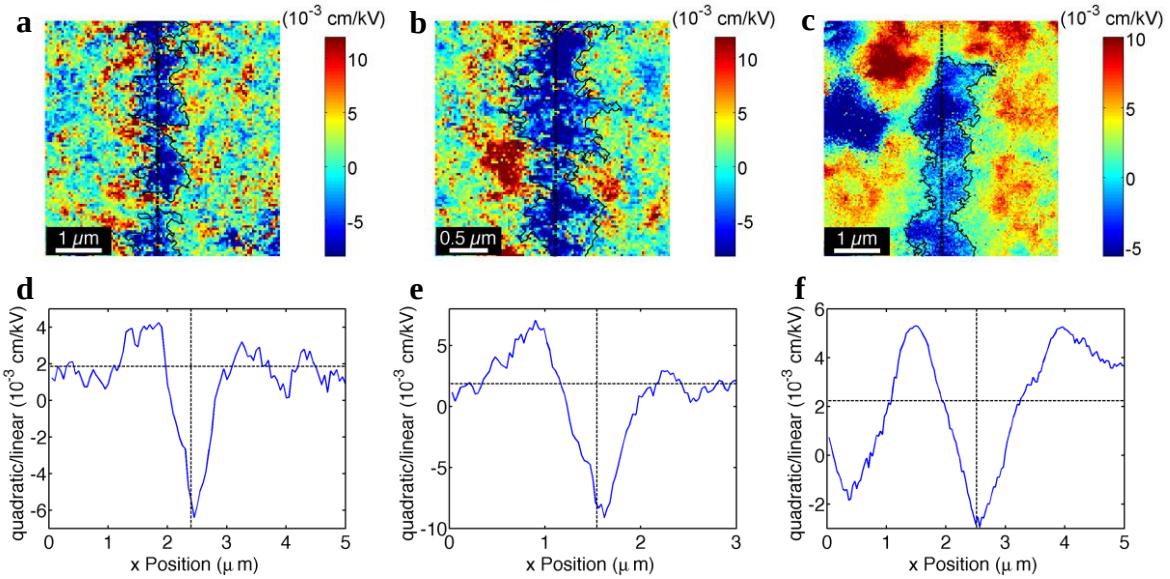

Figure 2.4: Local nonlinear response across a 24° grain boundary in PZT 45/55. Nonlinear response quadratic / linear maps measured across the grain boundary for the 425 nm thick sample (a) 5μm x 5μm and (b) 3μm x 3μm and for the 611 nm thick sample (c) 5μm x 5μm. Dotted lines denote the location of the grain boundary and solid lines border the selected regions of low response across the boundary for analysis. Plots (d-f) show the nonlinear response quadratic / linear for maps averaged across y positions where (d) corresponds to map (a), (e) corresponds to map (b), and (f) corresponds to map (c). The vertical line denotes the grain boundary and the horizontal line is the off-boundary average nonlinear response.

The width of reduced response observed for the 425 nm thick film and the 611 nm thick film indicates that the influence of a grain boundary is not determined by the film thickness. In addition, the width of the region influenced by the grain boundary is substantially larger in scale than the cluster size observed on either side of the boundary due to other pinning centers that

may influence domain wall motion. Thus, artifacts associated with the variation in top electrode thickness, which should vary similarly far from and at the grain boundary, do not influence the observed length scale of reduced nonlinear response.

Local measurements collected on the 425 nm thick film indicate that there is variation in response from location to location. The mean quadratic to linear ratio varied from the left of the boundary at 0.74±0.10 $x10^{-3}$ cm/kV to the right side of the boundary at 2.95±0.10 $x10^{-3}$ cm/kV. Mean ratios and standard deviations for all maps discussed are included in Table 2.3. This variation is likely due to a greater portion of the nonlinear response becoming negative in the map measured far to the left of the boundary, establishing a tendency toward a non-Rayleigh response. Regions with non-Rayleigh response are expected due to the local piezoelectric measurement being made up to fields beyond the Rayleigh regime. It is significant that regions with both positive and negative quadratic/linear ratios response are still observed. This suggests that the Rayleigh formalism is appropriate in some but not all regions. This may be due to a non-random spatial distribution of pinning sites, a non-Gaussian distribution of pinning energies, or the presence of interacting domain walls.[21] Using a mean nonlinear response and standard deviation from a combination of the two maps, the region to the left of the grain boundary showed clusters of high (0.23±0.03 μm) and low (0.35±0.11 μm) nonlinear response. The region to the right of the grain boundary showed similar cluster sizes which also exhibited high (0.26±0.05 μm) and low (0.22±0.03 μm) nonlinear response.

The average nonlinear response away from the grain boundary on the 611 nm thick film was measured to be 2.23±0.04 $x10^{-3}$ cm/kV. Clusters of high and low response were also observed in this sample with average size of 0.23±0.04 μm and 0.24±0.06 μm, respectively, similar to those measured on the 425 nm thick film. It is significant that the region of reduced

response observed at the grain boundary on both samples is ~3 times larger than the high and low response cluster size observed on both samples. This unambiguously demonstrates that the 24º tilt grain boundary influences a larger volume of material than other pinning sites present in these films.

Table 2.3 : PZT 45/55 local nonlinear response.

Mean and standard deviation of nonlinear response measured by BE-PFM.

Sample Thickness	Region	Mean Quadratic / Linear (10^{-3} cm/kV)	Standard Deviation (10^{-3} cm/kV)
611 nm	Off Boundary	2.23±0.04	1.96
611 nm	Across Boundary	2.01±0.06	4.70
425 nm	Left of Boundary	0.74±0.10	4.99
425 nm	Right of Boundary	2.95±0.10	4.89
425 nm	5µm Across Boundary	1.14±0.10	5.31
425 nm	3µm Across Boundary	0.87±0.12	6.02

Measurements across the grain boundary were taken on the 611 nm thick film with a 5 µm x 5 µm map at a pixel size of 33 nm. Figure 2.4(c) shows the distribution of nonlinearity for the measurement across the grain boundary. The average nonlinearity of the map across the grain boundary is 2.01±0.06 $x10^{-3}$ cm/kV, similar to that measured far from the grain boundary. However, the standard deviations are drastically different, at 1.96 $x10^{-3}$ cm/kV far from and 4.70 $x10^{-3}$ cm/kV across the grain boundary. This large difference was not observed for the 425 nm thick sample, where the standard deviation of the combined maps far from the grain boundary was 5.07 $x10^{-3}$ cm/kV and across the grain boundary, 5.31 $x10^{-3}$ cm/kV and 6.02 $x10^{-3}$ cm/kV for the 5 µm and 3 µm maps respectively. The average nonlinearity of the maps taken across the grain boundary were similar to the average nonlinearity far from the grain boundary with a map

average of 1.14±0.10 x10^{-3} cm/kV for the 5 μm map and 0.87±0.12 x10^{-3} cm/kV for the 3 μm map.

Averaging the nonlinear response vertically in the direction of the grain boundary and plotting as a function of position perpendicular to the boundary as in Figure 2.4(d-f) provides information of the average nonlinear response as a function of distance from the grain boundary. The average response is observed to be symmetric with the grain boundary, indicating that the grain boundary pins domain wall motion equally on both sides of the boundary. It is intriguing to note that a maximum in the nonlinear response is observed near the grain boundary immediately neighboring the region of low nonlinearity.

To reveal the fundamental mechanisms of a well-defined grain boundary on the movement of domain walls, comparison of the domain structure near and far from the grain boundary is essential. Figure 2.5 is a set of TEM diffraction contrast images obtained near the [100] zone axis, showing the typical domain structures near the grain boundary in an unpoled specimen. Needle shaped domains with (011)/(0$\bar{1}$1) domain walls inclined ~±45° to the PZT/SRO interface are apparent in the PZT film. For convenience, the coordinate system of the matrix is defined with the *a*-axis nearly parallel to the grain boundary, the *b*-axis nearly perpendicular to the grain boundary, and the *c*-axis perpendicular to the substrate. Therefore, domains are defined as *a*-domain when the polarization vector is along the *a*-axis, as *b*-domain when the polarization vector is along the *b*-axis, and as *c*-domain when the polarization vector is along the *c*-axis of the matrix. The (011)/(0$\bar{1}$1) domain walls observed in Figure 2.5 separate tetragonal *b*- and *c*-domains, presumably in the non-charged ‘head-to-tail’ configuration.

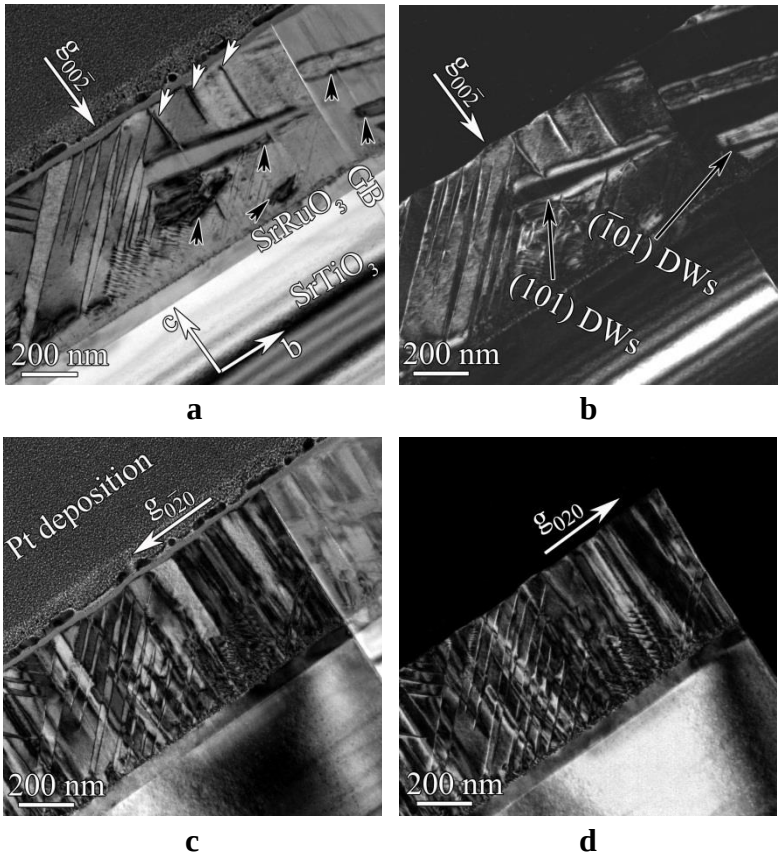

Figure 2.5: Virgin PZT 45/55 cross-section TEM.

Cross-sectional TEM images of virgin specimen obtained near the [100] zone axis (left grain) showing the domain structures near the grain boundary: (a) bright field and (b) dark field images with diffraction vector g = $00\bar{2}$, (c) bright field image with g = $0\bar{2}0$, (d) dark field image with g = 020.

However, a different domain structure indicated by black arrows in Figure 2.5(a) and 2.3(b), dominates ~500 nm either side of the grain boundary. Figure 2.5(c) and Figure 2.5(d) illustrates that the domain walls in the vicinity of the grain boundary are out of contrast when imaging with $\pm g_{020}$ conforming to $\boldsymbol{g.R} = 0$ and defining the habit plane as being within the (h0l)

trace. The allowed domain wall habit planes within this trace for tetragonal PZT are (101)/($\bar{1}$01), defining *a*-domains alternating with *c*-domains.

The traces of the (101)/($\bar{1}$01) domain walls deviate from the expected orientation parallel to the PZT/SRO interface. This may be explained by considering that cutting the sample in the FIB was carried out perpendicular to the grain boundary, which is rotated ±12° from the (010) plane about the *c*-axis, resulting in domain walls with what initially appeared to be unusual inclination angles within the TEM foil. Figure 2.6(a) illustrates how the FIB has been used to make a cut 12º clockwise around the *c*-axis from the (100) plane, corresponding to the left side of the grain boundary, with the inclined (101) domain walls retained in the TEM foil. Similarly, a TEM foil with (101) domain walls on the right of the grain boundary (cut counter-clockwise 12°) resulted in inclined domain walls but in opposite orientation, as illustrated in Figure 2.6(b). TEM foils for (101) and ($\bar{1}$01) domain walls on both sides of the grain boundary are also shown. The relative crystallographic planes and orientations of the domains on both sides of the grain boundary can be established according to their trace orientations. The domain walls of the black arrowed domains in Figure 2.5(a) and Figure 2.5(b) on each side of the grain boundary are thus determined as (101) and ($\bar{1}$01) for the left and right sides, respectively, with opposite polarization directions within the domains at an angle of 180° – 24° = 156°.

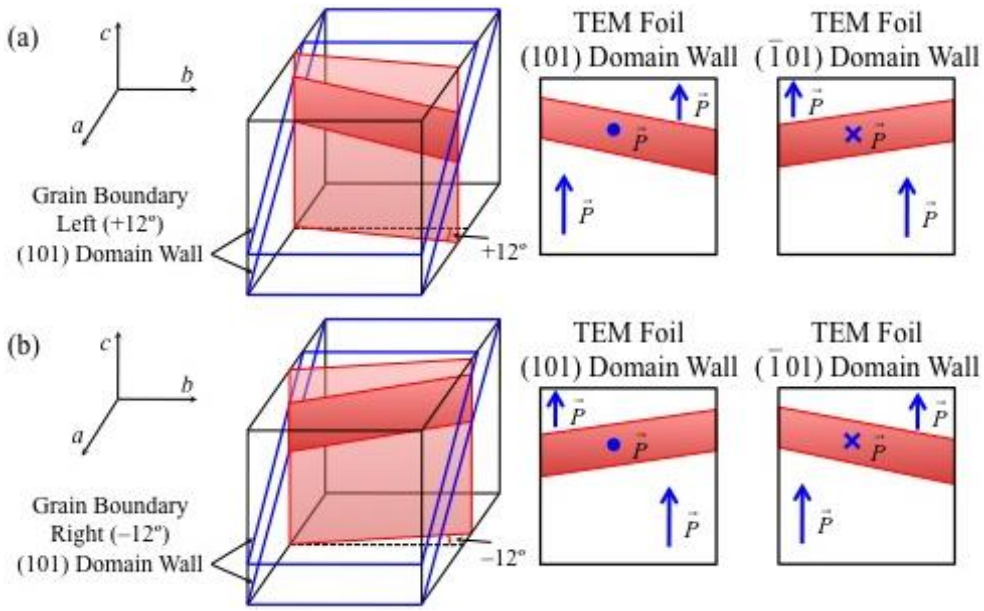

Figure 2.6: Domain walls at the grain boundary.

Schematics illustrating how FIB has been used to cut a TEM thin foil specimen (shown in red) from a matrix containing (101) domain walls. The schematic illustrates foil specimens with (101) and ($\bar{1}$01) domain walls with the cutting direction: (a) clockwise 12° and (b) counter-clockwise 12° about the *c*-axis off the (100) plane.

In addition to the cross-hatched domains, a further typical feature of the films is the vertical columnar structure, Figure 2.5(c) and Figure 2.5(d), which is due to threading dislocations, a typical growth defect arising from the lattice mismatch between the PZT and SRO. Most of the threading dislocations are out of contrast when imaging with g_{002}, which suggests that they are primarily edge character dislocations with the Burgers vectors parallel to the PZT/SRO interface. Dislocations with components normal to the PZT/SRO interface are also observed near the grain boundary, as shown by the white arrows in Figure 2.5(a). The strong contrast of the dislocation lines near the grain boundary suggests a pure-screw character with the Burgers vector $\vec{b}$ = [001].[86], [87]

Figure 2.7 shows plan-view images of an unpoled specimen near the grain boundary, obtained along the [001] zone axis. Figure 2.7(a) reveals a cross-hatched domain structure typical of a tetragonal ferroelectric phase, where the domain walls are inclined at 45º to the film surface normal. There is a preference near the grain boundary for domains with the major component of the polarization to be parallel to the boundary with *a*- and *c*-domains separated by (101)/($\bar{1}$01) domain walls. These domains are smaller than those observed farther away from the grain boundary and are consistent with the cross-section micrographs. The dark speckles are threading dislocations, which have a strain-field around a dislocation core and are visible under certain diffraction contrast conditions.

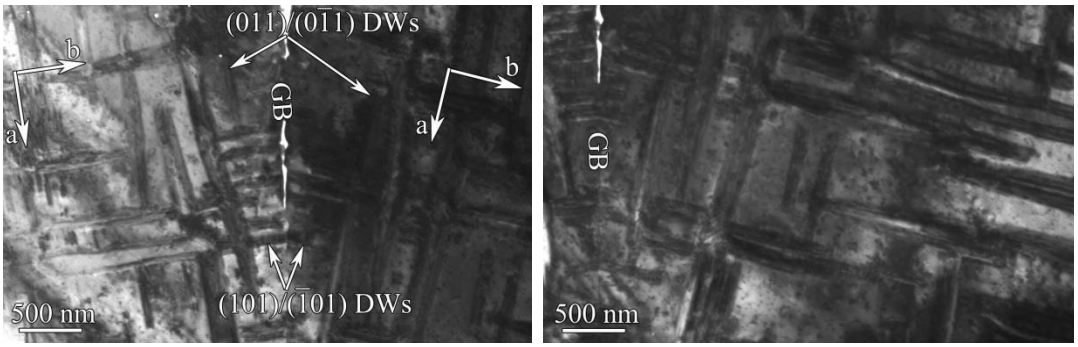

a **b**

Figure 2.7: Virgin PZT 45/55 plan-view TEM.

(a) and (b) Plan-view bright field images of virgin specimen obtained along the [001] zone axis showing the domain structures near the grain boundary.

Figure 2.8 shows the cross-sectional TEM images of the poled specimen near the grain boundary, obtained near the [100] zone axis. Cross-hatched domain walls are present, with a dense arrangement of *a*-, *b*-, and *c*-domains separated by (011)/(0$\bar{1}$1) and (101)/($\bar{1}$01) domain walls. In Figure 2.8(a) and Figure 2.8(b), (101) type domain walls (shown by short white arrows)

appear in the film far away from the grain boundary, but only ($\bar{1}$01) type domain walls appear adjacent to both sides of the grain boundary, as illustrated in the dark field inset in the bottom right of Figure 2.8(a). In contrast to the intersection angle of 156° for the polarization directions of a^{Left}/–a^{Right} domains on each side of the grain boundary in the virgin specimen, the intersection angle of a^{Left}/a^{Right} domains at the grain boundary in the poled specimen is 24°.

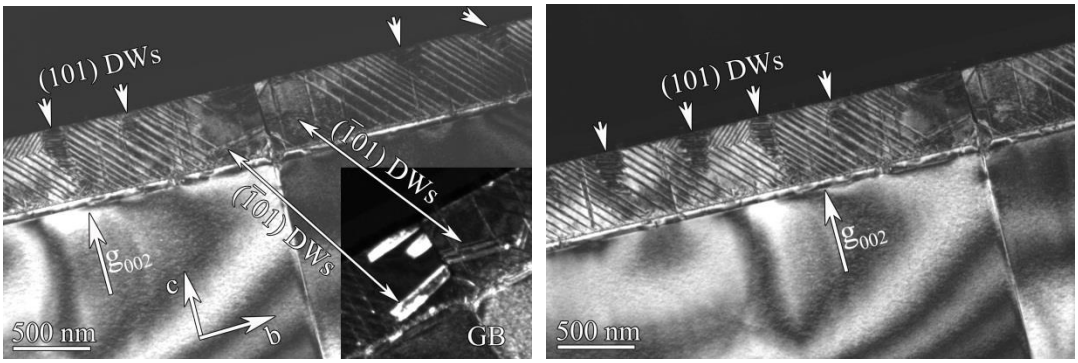

a **b**

Figure 2.8: Poled PZT 45/55 cross-section TEM.

Cross-sectional TEM images of poled specimen obtained near the [100] zone axis (left grain) showing the domain structures near the grain boundary: (a) and (b) dark field images with diffraction vector g = 002, the inset in the right bottom of (a) obtained in a slightly different condition revealing the same ($\bar{1}$01) type domains in both sides of the grain boundary.

Figure 2.9 shows the plan-view images of the poled specimen near the grain boundary, obtained along the [001] zone axis. Highly ordered, cross-hatched *a*-, *b*-, and *c*-domains separated by (011)/(0$\bar{1}$1) and (101)/($\bar{1}$01) domain walls are present. Generally, only *a*- and *c*-domains are preferred near the grain boundary, separated by (101)/($\bar{1}$01) type domain walls.

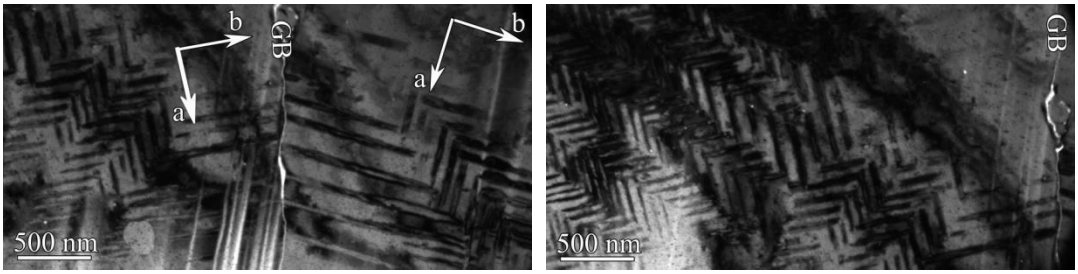

a **b**

Figure 2.9: Poled PZT 45/55 plan-view TEM.

(a) and (b) Plan-view bright field images of poled specimen obtained along the [001] zone axis showing the domain structures near the grain boundary.

2.4 Discussion

There are a number of critical observations associated with these results. First, the domain structure observed shows a lower likelihood of (011)/(0$\bar{1}$1) domain walls adjacent to the grain boundary. In order to minimize the strain at the grain boundary, the strain due to the ferroelectric distortion must be the same on both sides of the boundary according to the Fousek-Janovec criteria,[88] which dictates that the deformation of adjacent domains match at their interface. Extending the Fousek-Janovec criteria to consider the permitted domain orientations on either side of a 24º symmetric grain boundary, only *a*- or *b*-domains with an angle of 24º or 156º and *c*-domains with an angle of 0º or 180º between polarization vectors allow the ferroelectric strain on either side of the grain boundary to match.

It is also necessary to examine the intersection of domain walls at the grain boundary. Figure 2.10 shows equivalent domain walls from both crystals intersecting the grain boundary. In Figure 2.10(a), the intersection of (101) domain walls from both crystals lies on the grain boundary, allowing angles between adjacent polarization directions of 24º for *a*-domains and 0º

for *c*-domains. Alternatively, Figure 2.10(b) shows the intersection of (011) domain walls from both crystals penetrating the grain boundary, requiring adjacent polarizations at the grain boundary with non-allowed angles. This results in additional stress and reduces the likelihood of observing those domain walls.

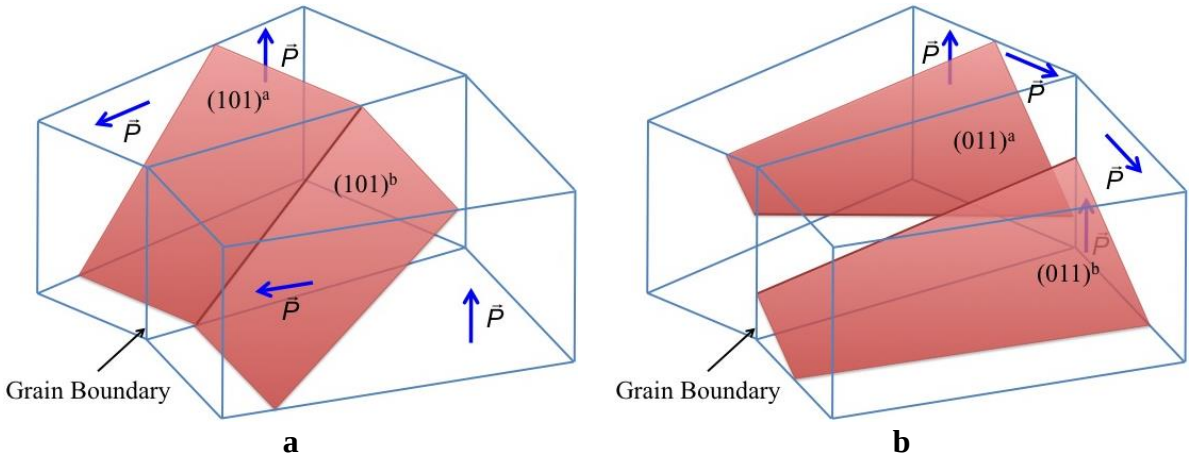

Figure 2.10: Permitted domain walls at the grain boundary.

Domain walls from both sides of the grain boundary shown intersecting the 24° tilt grain boundary. (a) The intersection between (101) domain walls lies on the grain boundary while (b) the intersection between (011) domain walls does not lie on the grain boundary.

The manner in which grain boundaries pin domains appears to be related to a change in the domain state influenced by the grain boundary. This is evident from the width of reduced nonlinearity being related to the region with primarily *a*- and *c*- domains in the TEM images. As shown in Figure 2.8 for the poled domain structure, *b*- domains, with (011)/(0$\bar{1}$1) type domain walls, are not present within 300-500 nm from the grain boundary. This range is consistent with the range of nonlinear response that lies below the film average response, indicating that (101) as opposed to (011) domain wall orientation stabilized at the grain boundary is responsible for the decreased response.

Furthermore, the significant decrease in nonlinear response at the grain boundary in both films indicates that grain boundaries serve as strong pinning centers. The width of the region influenced by the 24º tilt boundaries is large (~720-820 nm), providing one explanation for observations on both bulk polycrystalline and thin film ferroelectrics on the grain size dependence of the functional properties below ~1 micron grain sizes.[16], [75]

It has previously been shown that the nonlinear response in bulk ceramics [16], [69] and thin films [65] varies with Zr/Ti content in PZT; a higher nonlinear response is obtained for rhombohedral with respect to tetragonal compositions. Although this has previously been attributed to increased clamping of domain walls due to a larger spontaneous strain in tetragonal compositions, there is also a trend for higher nonlinear response in compositions with a higher density of domain walls. It appears that for the samples examined here, the increased concentration of domain walls is likely responsible for the local maxima in the nonlinearity on either side of the grain boundary. Near the grain boundary, there is a preference for *a*- and *c*-domains, as opposed to a mixture of *a*-, *b*-, and *c*-domains farther from the grain boundary. This indicates that near the grain boundary there is a tendency for the polarization to be as close to parallel to the grain boundary as possible. Fewer domain wall variants at the grain boundary may result in a lower nonlinear response due to preferential pinning at the grain boundary. The increase in possible domain wall variants further from the boundary may result in a higher nonlinear response despite increased domain wall – domain wall interactions under applied field.

2.5 Conclusions and Summary

A decrease in the piezoelectric nonlinear response was observed at the 24º tilt grain boundary with a total influence of 720-820 nm. A variation in domain structure at the grain

boundary was observed with a tendency toward *a*- and *c*-domains with polarization aligned nearly parallel to the grain boundary, whereas *a*-, *b*-, and *c*-domains with (011)/(0$\bar{1}$1) and (101)/($\bar{1}$01) type domain walls are observed farther from the boundary. Through correlation of the TEM and BE-PFM data, the decreased nonlinear response is attributed to this change in the domain wall configurations at the grain boundary, resulting in the grain boundary acting as a strong pinning source for domain wall motion. Regions of high nonlinear response were observed neighboring the minimum at the grain boundary, where *b*-domains with (011)/(0$\bar{1}$1) type domain walls are introduced. Although a symmetric bicrystal was utilized in these measurements, the variation in domain structure observed and its influence on nonlinear response can be applied to multigrain films and ceramics, where the lattice in neighboring grains may not be symmetric across the grain boundary. Large angle tilt grain boundaries result in a change in preferred domain wall orientation near the grain boundary and a decreased nonlinear response, providing an explanation for the properties observed in specimens with sub-micron grain size.

Chapter 3: Domain Pinning Near a Single Grain Boundary in Tetragonal and Rhombohedral Lead Zirconate Titanate Films

The interaction of grain boundaries with ferroelectric domain walls strongly influences the extrinsic contribution to piezoelectric activity in $Pb(Zr,Ti)O_3$ (PZT), ubiquitous in modern transducers and actuators. However, the fundamental understanding of these phenomena has been limited by complex mechanisms originating from the interplay of atomic-level domain wall pinning, collective domain wall dynamics, and emergent mesoscopic behavior. This chapter utilizes engineered grain boundaries created by depositing epitaxial PZT films with various Zr:Ti ratio onto 24º $SrTiO_3$ tilt bicrystals. The nonlinear piezoelectric response and surface domain structure across the boundary are investigated using piezoresponse force microscopy whilst cross section domain structure is studied using transmission electron microscopy. The grain boundary reduces domain wall motion over a width of 800±70 nm for PZT 45:55 and 450±30 nm for PZT 52:48. Phase field modeling provides an understanding of the elastic and electric fields associated with the grain boundary and local domain configurations. This study demonstrates that complex mesoscopic behaviors can be explored to complement atomic-level pictures of the material system.

3.1 Introduction

In bulk and thin film ferroelectrics, grain boundaries limit the dielectric and piezoelectric properties, reducing the responses of sensors, actuators, and memory devices.[61], [72], [89],

[90] Single crystals or epitaxial films cannot always be utilized. Understanding the effect of grain boundaries on domain wall motion is, therefore, essential for controlling device properties. Furthermore, the interaction of domain walls with grain boundaries is vital in describing the fundamental physics of ferroelectric materials.

For over 20 years the interaction between domain walls and grain boundaries has been studied with macroscopic measurements. In 1985 Arlt et al. reported decreasing permittivity with grain size below 0.7 μm in $BaTiO_3$ ceramics.[38] Later, measurements of the piezoelectric properties,[26], [75] Rayleigh response,[16] and field-induced switching indicated decreased extrinsic contribution to the functional properties as grain size decreased.[39], [76], [91]

Recently, domain wall pinning was studied using phase field models and density functional theory. It was found that stress concentrations and large internal electric fields at grain boundaries and triple points influence both domain nucleation and domain wall pinning.[37], [49], [74], [92] Additionally, a preference for specific polarizations on either side of high angle grain boundaries may produce pinning.[50] Significant charge concentrations can exist at 90º domain walls, which then exert a local pressure on 180º domain walls even at sub-switching electric fields due to variations in the local electric field.[40], [93]

Experimentally, PFM measurements demonstrated that 1- and 2-dimensional defects produce significant pinning of 180º domain walls in ferroelectric films.[34], [52], [78], [94]–[96] The local electric field created by defects and domain wall – domain wall pinning are the major contributions to domain wall pinning.[40], [97] It is widely reported that in tetragonal ferroelectrics, the domain structures of adjacent grains are correlated due to local strain and electric fields.[72], [98] Ivry et al. indicate that the local fields influence the domain structure up

to 300-400 nm from the grain boundary,[98] a result matching the distance observed for the influence of a grain boundary on domain wall motion.[2]

The contribution of domain wall motion to the dielectric and piezoelectric properties is dependent on composition and crystallographic structure.[61], [65], [69], [99], [100] The highest irreversible domain wall motion is observed at the morphotropic phase boundary and decreases as internal stress increases with increasing ferroelastic strain.[3], [69], [99] However, the role of ferroelectric distortion (e.g. rhombohedral, tetragonal, etc.) on domain wall interaction with planar defects is unknown. Recently (as described in the previous chapter), 24º tilt grain boundaries were shown to pin domain walls in tetragonal $PbZr_{0.45}Ti_{0.55}O_3$ (PZT 45/55) films and reduce domain wall motion ~350 nm to either side of the grain boundary, with strong dependence on the local domain structure.[2] It is anticipated that the relative pinning strength of any particular grain boundary will depend on the accommodation of the local strain by the ferroelectric domain structure.

This work explores the effect of ferroelastic strain on the domain structure and local piezoelectric nonlinearity at and near the grain boundary. Comparisons are made between tetragonal and rhombohedral epitaxial PZT thin films with 24º tilt grain boundaries. Particular emphasis is placed on the spatial width of reduced or enhanced nonlinear response resulting from the grain boundary.

3.2 Materials & Methods

3.2.1 Material Synthesis

Bicrystal (100) $SrTiO_3$ substrates with a 24º tilt angle (MTI Corp.) were used to engineer a well-defined grain boundary. A $SrRuO_3$ buffer layer was deposited as a bottom electrode

followed by deposition of the $Pb(Zr_xTi_{1-x})O_3$ films, with compositions x = 0.20, 0.45, and 0.52. All samples were prepared as described previously.[2]

Electrical measurements of capacitance and dielectric loss (HP 4284A Precision LCR Meter) were made as a function of *AC* voltage to 50% of the coercive voltage at the same frequency range as used for BE-PFM (300 kHz) to determine the dielectric nonlinearity $\alpha_e/\varepsilon_{init}$ with Rayleigh analysis.

3.2.2 Band Excitation Piezoresponse Force Microscopy

BE-PFM characterization of the *local* piezoelectric nonlinear response (Asylum Research, Inc. Cypher) was made on a 5 μm x 5 μm region with a 100 x 100 pixel grid in a 100 kHz band across the resonant frequency of the cantilever (NanoSensors PPP-EFM-50). Samples were poled at 230 kV/cm for 40 minutes for PZT 20/80, 310 kV/cm for 15 minutes for PZT 45/55, and 98 kV/cm for 35 minutes for PZT 52/48 and aged for 30 min prior to measurement. Poling parameters were determined using the global piezoelectric response (aixACCT DBLI). The capacitors were driven from the bottom, with tip and top electrode grounded. The drive voltage extended beyond the dielectric Rayleigh regime, as this was necessary in order to minimize noise. Thus, the reported values for nonlinear response are the ratio of the quadratic to linear response normalized to the film thickness, or $\frac{1}{2}\cdot\alpha_d/d_{33,init}$.[2]

Clusters of high and low nonlinear response were observed, as has been reported previously,[59] where the clustered regions were defined as being above or below the mean nonlinear response ± ½ standard deviation measured far from the grain boundary. Most low response pixels were observed at the grain boundary. Three methods were used to determine the width of influence for a grain boundary on the nonlinear response of a PZT thin film. The

reported width of influence and confidence reflects all analysis methods. Values for all three methods are reported for PZT 45/55 and PZT 52/48 in Table 3.1. A description of each method follows.

Table 3.1: Methods for analyzing nonlinear response.

Width of influence in μm determined by each of 3 different methods.

Composition	Method 1	Method 2	Method 3
PZT 45/55	0.722±0.056	0.870±0.044	0.837±0.041
PZT 52/48	0.429±0.088	0.421±0.056	0.476±0.016

Method 1: Clustering of low response regions was determined as having a value more than half the standard deviation below the mean nonlinear response. The mean and standard deviation in the nonlinear response for each sample were determined from maps collected far (~5 mm) from the grain boundary. The total area enclosed in low response regions crossing the grain boundary was then divided by the total distance data was collected parallel to the grain boundary (5 μm) for an average width of influence. The error bars were determined as the 95% confidence in the width of low response at each row.

Method 2: Using all low response clusters on the map of the grain boundary as determined in Method 1, the number of low response pixels observed with distance from the grain boundary was represented in a histogram (see Figure 3.1). If a random distribution of the nonlinear response were observed with no clustering, approximately 30% of the pixels at each distance from the grain boundary should be low response. Due to clustering in the response, the cutoff value was set to 40% of the pixels observed at each distance from the grain boundary being low response. The error bars were determined as ±5% in the ratio of low response pixels.

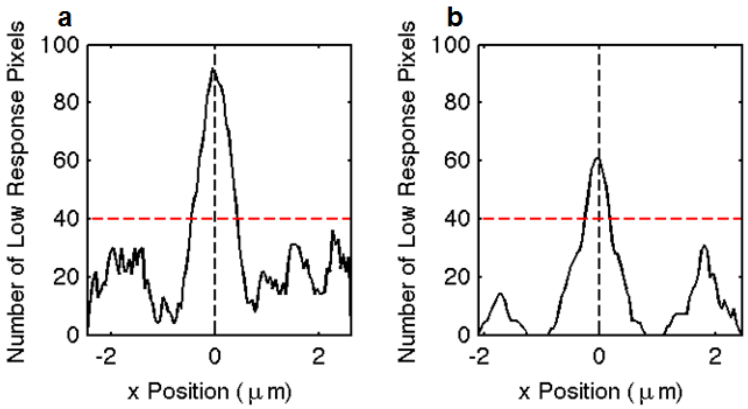

Figure 3.1: PZT 45/55 and PZT 52/48 width of reduced response method 2.

Number of low response pixels varying with distance from the grain boundary for (a) PZT 45/55 and (b) PZT 52/48. The red horizontal line marks the cutoff determined by 40 low response pixels out of 100 total pixels, while the black vertical line denotes the grain boundary.

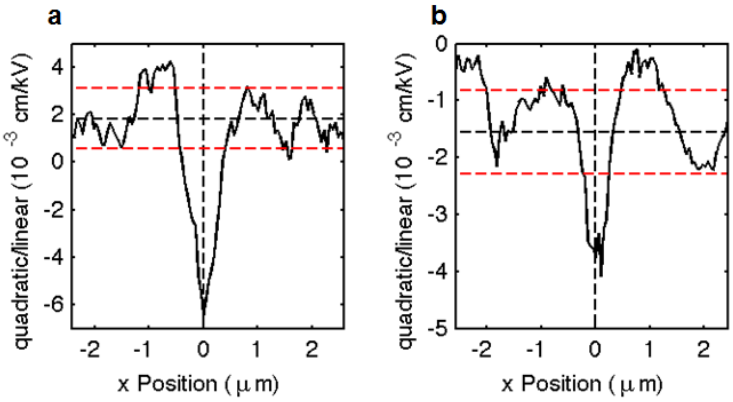

Figure 3.2: PZT 45/55 and PZT 52/48 width of reduced response method 3.

Nonlinear response averaged parallel to the grain boundary for (a) PZT 45/55 and (b) PZT 52/48. The black vertical line denotes the location of the grain boundary, while the black horizontal line shows the mean nonlinear response and the red horizontal lines indicate ±25% of the standard deviation.

Method 3: The average of the nonlinear response parallel to the grain boundary shows a minimum at the grain boundary. A cutoff value of 25% of the standard deviation below the mean nonlinear response was used to determine the width of influence, as shown in Figure 3.2. Error bars were determined as ±5% in the average nonlinear response.

3.2.3 Transmission Electron Microscopy

TEM provided information on the domain structure at and away from the grain boundary. Specimens were prepared with a dual beam focused ion beam/scanning electron microscope (SEM) (FEI Quanta 3D 200). SEM was used to locate the grain boundary then cross-section and plan-view TEM specimens containing the grain boundary were prepared. Micrographs were collected with a field emission JEOL 2010F JEOL 2010 Scanning Transmission Electron Microscope operated at 200 kV. The specimens were rotated (Gatan 925 double tilt rotation analytical holder) to orient the grain boundary vertical in the CCD camera image. The 24º bicrystal specimens were tilted to the symmetric condition with each grain 12º off the [100] zone axis for comparing the domain structures across the grain boundary.

3.2.4 Phase Field Modeling

Phase field modeling (conducted by Jason Britson) was used to investigate the relative stability of domain configurations around 24° tilt grain boundaries. As described previously,[37], [101]–[103] this approach evolves a domain structure defined by a continuous distribution of the polarization components, P_i, toward a minimum in the total energy. Free energy was modeled as the sum of contributions from the bulk free energy, domain wall energy, and electrostatic and mechanical interactions. The bulk free energy of the PZT thin film was modeled using the sixth

order Landau polynomial with the phenomenological constants measured by Haun, et al. for $Pb(Zr_{0.2},Ti_{0.8})O_3$.[104] Isotropic domain wall energy was also modeled using gradients in the polarization distribution in the model as $f_{DW} = \frac{1}{2} G P_{i,j}^2$ where G is the gradient energy coefficient,[102] which was assumed to have a value of 4.1×10^{-11} $C^{-2}m^4N$. This choice has been shown to lead to 90° domain wall width of 1-2 nm.

Electrostatic interactions between domains arising from the electric field, E_i, were included through the electrostatic energy with an isotropic background dielectric constant[105] assumed to be 10. Electric fields in the system were found by solving the Poisson equation assuming the electrodes to be ideally compensating and grounded.[106] When considering thin films with only *b/c* type domain structures and, consequently, highly charged grain boundaries, the electric energy was neglected since full compensation by free charge carriers around the grain boundaries was also assumed. The mechanical state of the thin film was solved from the mechanical equilibrium equation. The solution to this equation with appropriate boundary conditions and the associated energy contribution are described in detail in Refs [102], [107]. To model the bicrystal system the elastic constants were varied in each grain to accommodate the 12° rotation.

Films with the a/c domain structure were simulated on a discrete grid of 256 Δx × 128 Δx × 54 Δx while the film with the b/c domain structure was simulated on a grid of 120 Δx × 320 Δx × 54 Δx with Δx=0.5 nm. Periodic boundary conditions in the first two dimensions and appropriate thin films boundary conditions in the third dimension were used. Different film sizes were used to accommodate the different periodicities of the two domain structures. The thin film in both cases was 15 nm thick with a non-polarizable 7 nm thick layer of deformable substrate allowed to relax beneath the film.[102]

3.3 Results

Films were grown to a thickness of 481 nm for PZT 20/80, 425 nm for PZT 45/55, and 791 nm for PZT 52/48. X-ray diffraction showed phase pure tetragonal (PZT 20/80 and PZT 45/55) and rhombohedral (PZT 52/48) films with <001>/<100> out of plane. Synchrotron x-ray diffraction was conducted to determine the phase of the PZT 52/48 films. Measurements were collected on 004, 404, and 444 peaks and are shown in Figure 3.3. Splitting was observed in the 444 and 404 peaks, with no splitting observed in 004, corresponding to a rhombohedral structure.[108] Phi scans of the PZT 101 peak proved epitaxy on both sides of the grain boundary. The full width at half maximum for the PZT 002 peak rocking curve along with the permittivity, loss tangent, and remanent polarization for all compositions are provided in Table 3.2. The measurements indicate high film quality.

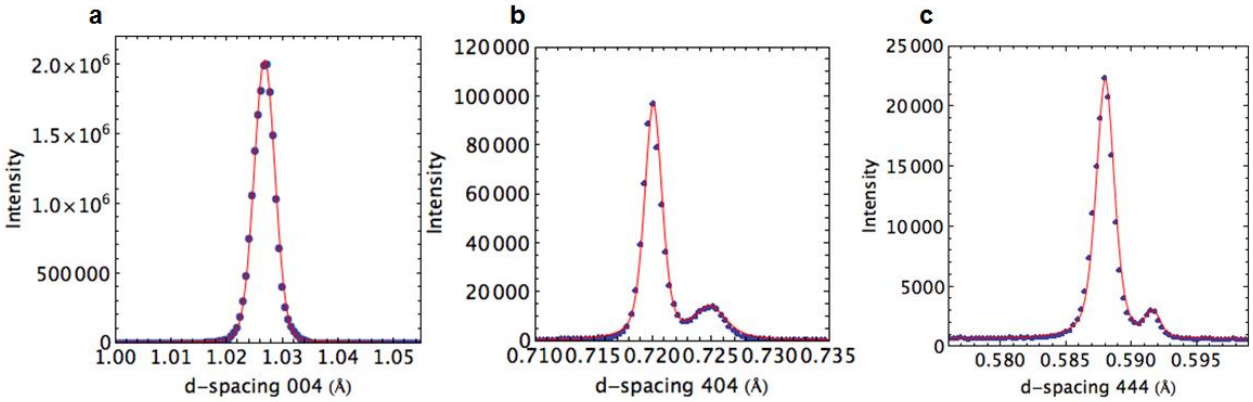

Figure 3.3: PZT 52/48 phase development.

Rod scans on the (a) 004, (b) 404, and (c) 444 peaks of PZT 52/48. Data were acquired at the Advanced Photon Source at beamline 33BM.

Table 3.2: PZT structural and electrical measurements.

Structural and electrical data for PZT films of different composition.

Composition	PZT 002 FWHM ($^o\omega$)	ε_r (10kHz, 30mV)	tanδ (%)	P_r ($\mu C/cm^2$)
PZT 20/80	1.19	224	0.8	44.5
PZT 45/55[2]	0.60	456	1.0	41.0
PZT 52/48	0.11	413	1.0	37.1

Global dielectric Rayleigh measurements and averaged local piezoelectric nonlinearities are presented in Table 3.3. As expected, the highest initial permittivity was observed for the composition near the morphotropic phase boundary (PZT 52/48). However, the highest $\alpha_e/\varepsilon_{init}$ was observed for PZT 45/55, followed by PZT 20/80 and PZT 52/48, similar to the trend observed in the averaged local nonlinear piezoelectric response. These results are probably at least partially a function of the fact the intrinsic polarizbility is largest near the MPB. It is also possible that a larger percentage of the domain walls in PZT 52/48 are reversibly excited, resulting in a higher reversible component and a lower irreversible component than PZT 45/55.

Table 3.3: Rayleigh analysis for various PZT compositions.

Composition dependence of dielectric and piezoelectric nonlinear response measured at 300 kHz.

Composition	Dielectric Rayleigh Parameters			BE-PFM Quadratic/Linear	
	ε_{init}	α_e (cm/kV)	$\alpha_e/\varepsilon_{init}$ x10^3 (cm/kV)	Mean x 10^3 (cm/kV)	Std. Dev. x 10^3 (cm/kV)
PZT 20/80	161.3±0.1	0.78±0.01	4.8±0.1	-0.66±0.03	1.73
PZT 45/55[2]	428.0±0.2	6.79±0.05	15.9±0.1	1.84±0.07	5.06
PZT 52/48	793.7±0.8	2.81±0.14	3.5±0.2	-1.56±0.02	1.46

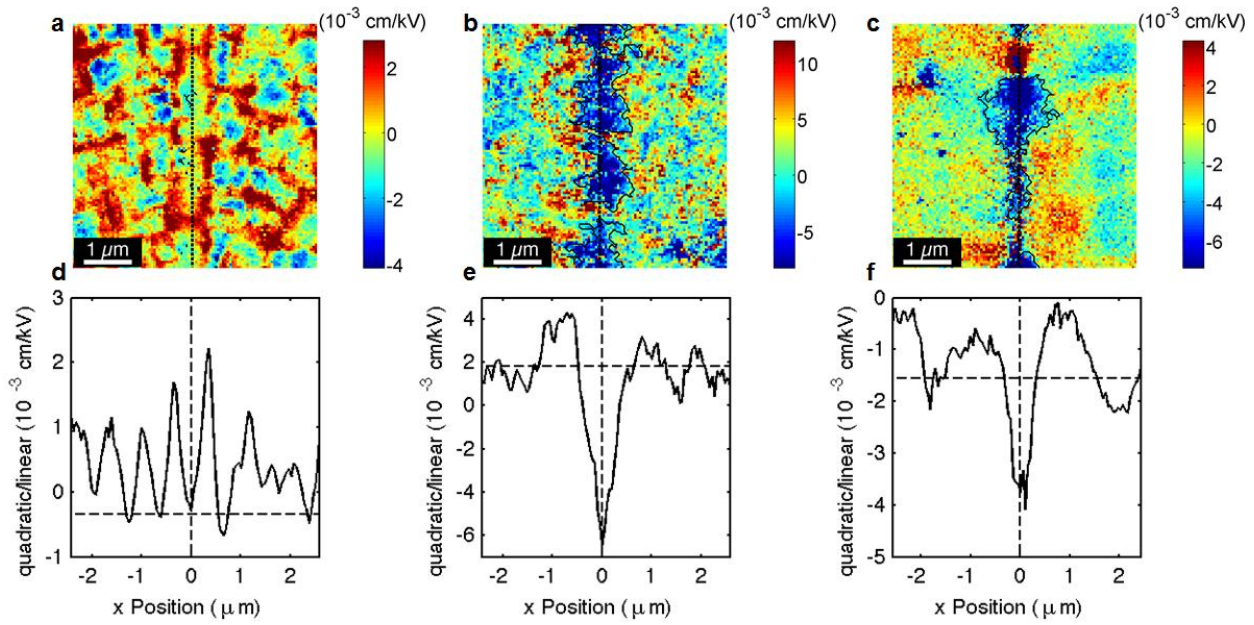

Figure 3.4: Local nonlinear response for various PZT compositions.

Nonlinear response quadratic / linear maps measured across the 24º grain boundary for (a) PZT 20/80 (b) PZT 45/55 (c) PZT 52/48. Dotted lines denote the location of the grain boundary and solid lines border the regions of low response across the boundary. Plots (d-f) show the nonlinear response quadratic / linear for maps averaged across y positions where (d) corresponds to map (a), (e) corresponds to map (b), and (f) corresponds to map (c). The vertical line denotes the grain boundary and the horizontal line is the off-boundary average nonlinear response.

Band excitation piezoresponse force microscopy (BE-PFM), Figure 3.4 (a-c), was used to collect maps of nonlinear response across the grain boundaries. For all three compositions there is a *local* minimum in the average nonlinear response at the grain boundary (Figure 3.4 (d-f)), indicating that a 24º grain boundary reduces the nonlinear response for all compositions. The average width of the reduced nonlinear response for PZT 45/55 is 800±70 nm and for PZT 52/48 is 450±30 nm, ~2-3x larger than the observed cluster size far from the grain boundary (240±30 nm for PZT 45/55[2] and 200±90 nm for PZT 52/48). The decreased width of reduced response

for PZT 52/48 relative to PZT 45/55 is attributed to improved relaxation of the strain and electric field associated with the grain boundary, possibly because of the higher domain wall density. Previous measurements on 24º tilt grain boundaries in PZT 45/55 films of various thicknesses showed no significant variation in the width of reduced response,[2] indicating that the different width of reduced nonlinear response for PZT 52/48 relative to PZT 45/55 is unlikely to be an artifact of the different thicknesses.

For PZT 20/80, the nonlinear response at the grain boundary varies spatially. Although no *global* minimum in response is observed at the grain boundary for PZT 20/80, on average there is reduced coupling of high nonlinear response from one side of the grain boundary to the other. As seen in Figure 3.4(a), ~28% of the grain boundary has nonlinear response more than half a standard deviation above the mean, indicating some coupling of domain wall motion across the boundary. However, the remainder of the grain boundary shows a significantly lower nonlinear response than that observed immediately adjacent to the grain boundary, indicating that the grain boundary primarily acts to reduce concerted domain wall motion.

To probe the underlying reasons behind the local nonlinear response, transmission electron microscopy (TEM) was used to determine the domain structure as a function of distance from the grain boundary. For the analysis of tetragonal films, *a*-domains are those with polarization in the plane of the film and nearly parallel to the grain boundary, *b*-domains have polarization nearly perpendicular to the grain boundary, and *c*-domains have polarization perpendicular to the film surface. Cross-sectional TEM provides information on how domain patterns extend through the film thickness. Figure 3.5 (a-f) provides micrographs of all films (a-c) before and (d-f) after poling. For both tetragonal compositions, all domain variants are observed >500 nm from the grain boundary. Near the grain boundary, PZT 20/80 had a

combination of *b*- and *c*-domains, while PZT 45/55 exhibited primarily *a*- and *c*-domains. PZT 52/48 showed a fine domain tweed structure attributed to reduced domain wall energy near the morphotropic phase boundary.[109]

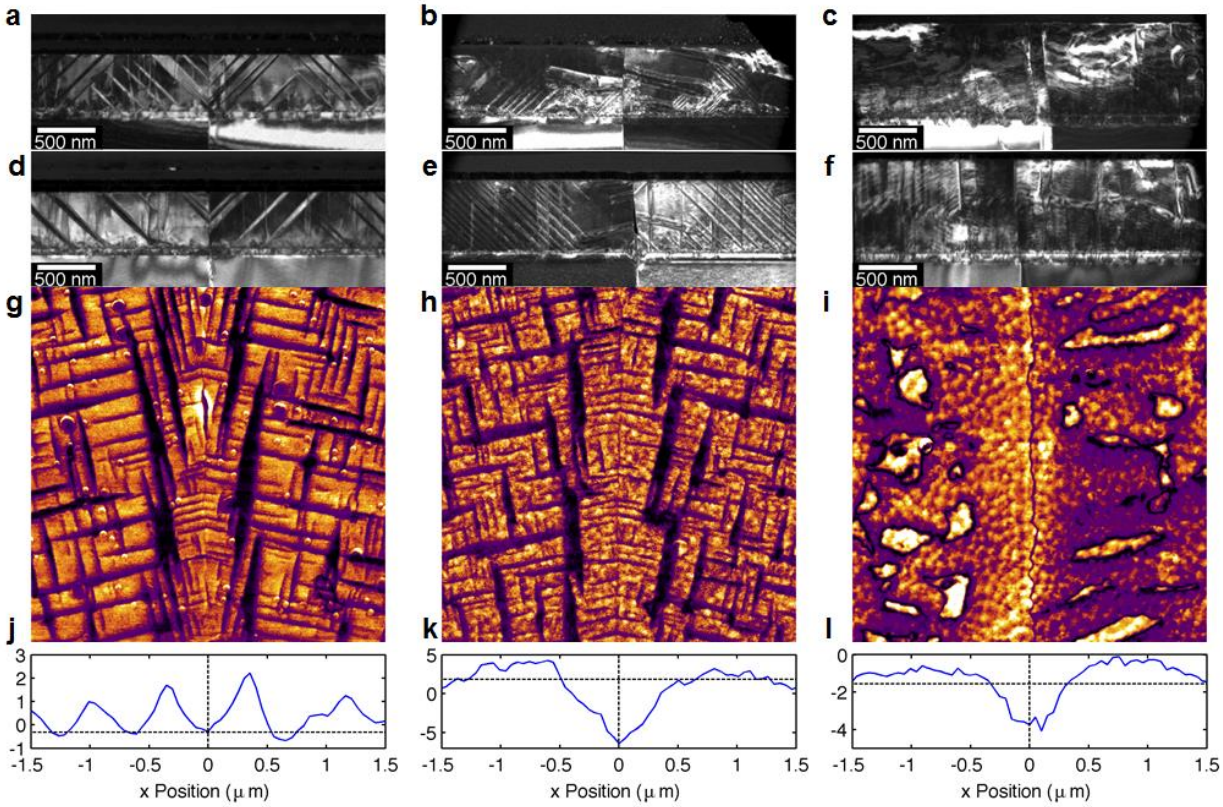

Figure 3.5: Domain structure correlates with the average nonlinear response for various PZT compositions.

Bright field cross-section TEM (a-c) unpoled and (d-f) poled PZT, (g-i) vertical PFM amplitude showing out of plane (bright) vs. in plane (dark) domains, and (j-l) mean nonlinear response in 10-3 cm/kV. Figures (a,d,g,j) PZT 20/80, (b,e,h,k) PZT 45/55, and (c,f,i,l) PZT 52/48. All figures have the same lateral scale with a total width of 3μm. The 24º grain boundary is located at x=0.

Vertical PFM amplitude measurements of the domain structure off the capacitor and prior to poling are shown in Figure 3.5 (g-i) with *c*-domains evident as bright (high-response) regions

while *a*- and *b*-domains are both evident as dark (low-response) regions. Figure 3.5 (g) and 3.8(a) show that the domain variants observed by PFM are similar to those in plan-view TEM. The PFM images show that the surface domain structures change along the grain boundary. A combination of all three ferroelastic domain variants for PZT 20/80 and 45/55 are evident. Note that for PZT 52/48 the out-of-plane response amplitude should be uniform in an ideally-poled sample. The dark regions represent domain boundaries between regions with opposite out-of-plane phase response.

Phase field modeling was employed to understand the forces controlling domain structure development at the grain boundary. To model the case where *a*- and *c*-domains cross the grain boundary, the system was initialized with four 90º domain walls oriented perpendicular to two grain boundaries. When allowed to relax, the domain walls rotated 12º, producing a stable configuration along the <101> plane in each grain as shown in Figure 3.6 (a), similar to the PZT 45/55 domain structure described previously.[2] In addition, the domain walls also bend towards the grain boundary, with most bending near the top and bottom surfaces of the film. This produced a wider domain near one boundary, but a narrower domain at the other grain boundary. A minimum in the local electric energy was associated with both boundaries where the domains met across the grain boundary. The reduction in the electric energy is particularly strong at the grain boundary where the domains form a domain wall with a slight tail-to-tail arrangement. Both boundaries, however, are associated with moderate increases in the local elastic energy and stresses within the *a*-domains, as can be seen in Figure 3.6 (b,c). Increases in the elastic stresses and energy are larger for the tail-to-tail domain arrangement, indicating that the head-to-head arrangement, associated with an increased domain thickness, is more stable. (Figure 3.6 (c,d)) Analysis of the poled domain structure in Figure 3.5 (d), for which the polarization directions are

known, shows *b*-domains increasing in thickness near the grain boundary by ~10nm for the head-to-head configuration in PZT 20/80, agreeing with the phase field analysis.

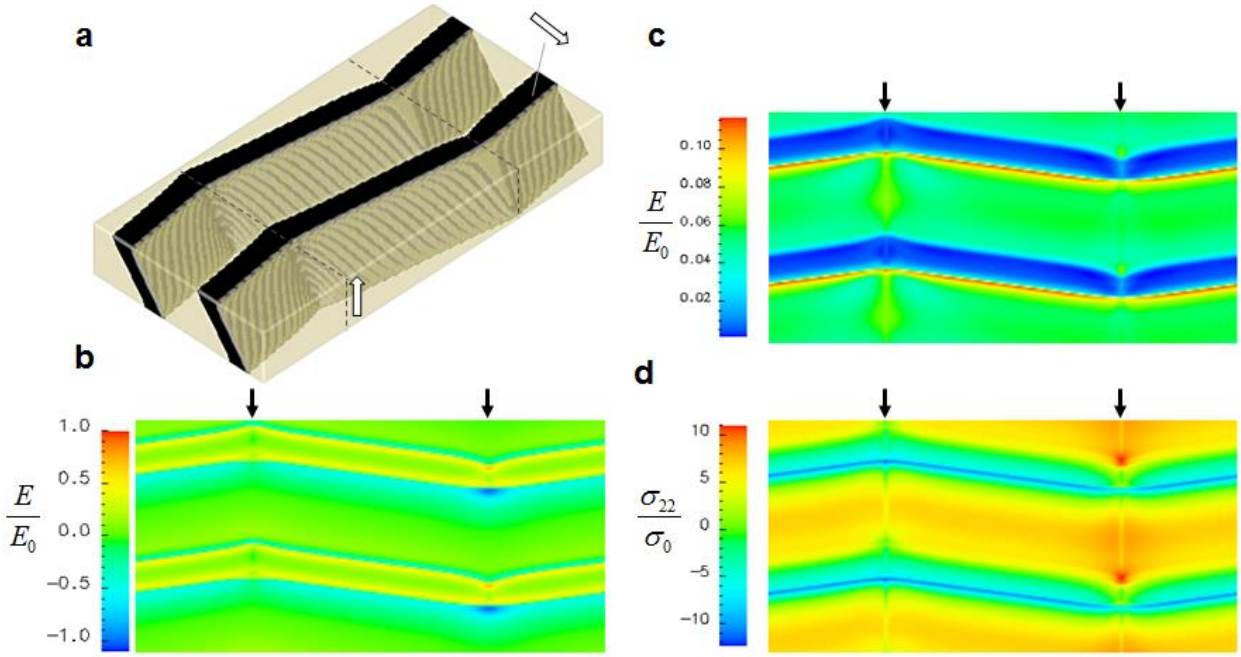

Figure 3.6: Phase field model of *a*/*c* domain structure.

(a) Phase field simulation of stable domain configuration for the *a*/*c* domain structure. (b) Electric energy at the top surface of the film structure. (c) Elastic energy at the top surface of the film structure. (d) In-plane σ_{22} stress around the grain boundaries. σ_0 = 93.1 MPa. The grain boundaries are marked by (a) dashed lines and (c-d) black arrows.

A similar model consisting of the *b*/*c* domain structure observed in PZT 20/80 thin films was considered (Figure 3.7). Charged domain interfaces at the grain boundary were assumed in this model to be completely compensated by free charges by ignoring contributions from the electrical energy to the free energy of the system. A *b*/*c* domain structures was seeded, so as to minimize elastic energy and produce a coherent interface. However, after evolution, the phase field model did not reproduce a stable *b*/*c* configuration at the grain boundary. Rather, the *b*/*c*

domain structures observed in TEM (Figure 3.5 (a)) rapidly transformed to a single *c*-domain adjacent to the grain boundary due to compressive σ_{11} stress and elastic energy concentration at the grain boundary. This suggests that the observed *b*/*c* domain structure is likely stabilized by either built-in charge or an additional stress compensation mechanism. Such defects, if present, could reduce the piezoelectric response near the grain boundary as observed experimentally.[38]

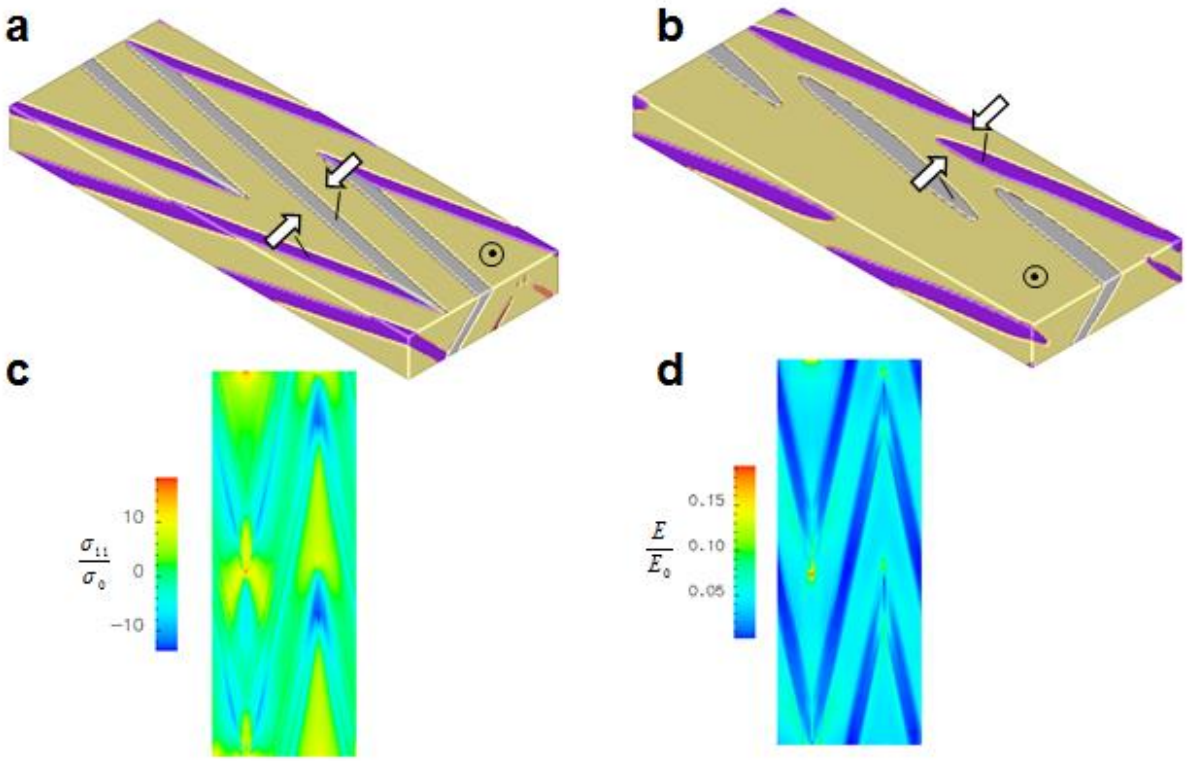

Figure 3.7: Phase field model of *b*/*c* domain structure.

(a) Domain structure of film with head-to-head and tail-to-tail b/c domain structure after 100 time steps. (b) *b*/*c* domain structure after partial relaxation (14,000 time steps) showing b-domains retreating from the grain boundaries to produce a uniform c-domain around the grain boundaries. (c) In plane σ_{11} stress around the domains. σ_0 = 93.1 MPa. (d) Elastic energy at top surface of thin film showing elevated elastic energy within the b-domain around the grain boundaries.

3.4 Discussion

It is clear from Figure 3.4 that for the rhombohedral PZT 52/48, the 24º tilt grain boundary influences the mobility of domain walls over a much shorter spatial scale than is the case for the analogous grain boundary in PZT 45/55. Given the significant differences in domain wall density (See Figure 3.5), the difference in the width of influence for the grain boundary is attributed to improved strain relaxation for the rhombohedral sample, based on the fine domain structure observed by TEM.

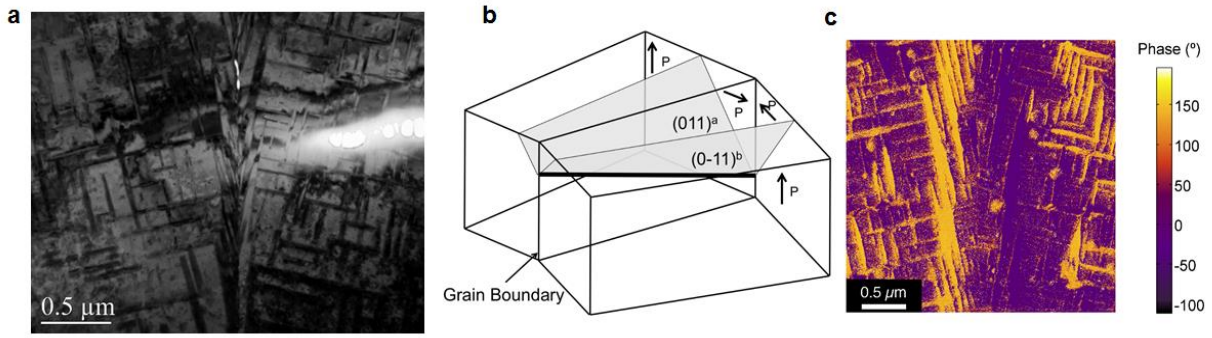

Figure 3.8: Analysis of PZT 20/80 domain structure near the grain boundary.
(a) Plan-view TEM of PZT 20/80 unpoled region showing similar domain structure to vertical PFM in Figure 2(g). (b) Schematic of domain wall strain matching at the grain boundary showing how (011) type 90º domain walls from each grain intersect to minimize strain at the grain boundary with head-to-head polarization. (c) Lateral PFM of PZT 20/80 showing in-plane polarization reversal at the grain boundary.

For the tetragonal films, while PZT 45/55 exhibits a well-defined minimum in the nonlinearity at the grain boundary, an alternating nonlinear response was observed for PZT 20/80. These differences are attributed to the disparate poled domain structures. For PZT 20/80,

ferroelastic strain matching at the grain boundary permits registry of domain walls between *b*- and *c*-domains (see Figure 3.5(a,d)) as described previously.[2] From Figure 3.8(b), to maintain a head-to-tail domain configuration within each grain there must be a polarization discontinuity at the grain boundary for either the *b*- or *c*-domains. The PFM lateral phase measurements collected on a virgin region in Figure 3.8(c) show a polarization discontinuity in the in-plane polarization at the grain boundary, indicating that the *b*-domains at the grain boundary have nearly antiparallel polarizations.

Figure 3.5(d) shows *b*-domains from one side of the boundary bordered either by *b*- or *c*-domains on the other side, depending on location. A similar observation can be made for *a*-domains at the grain boundary in Figure 3.5(e). The case where *b*-domains border *b*-domains at the grain boundary minimizes the local strain energy. However, charge accumulation is required to compensate the head-to-head domain configuration for *b*-domains. The intersection of *b*- and *c*-domains at the grain boundary minimizes charge accumulation, but results in uncompensated local strain.

Note that *b*-domains are preferred at the grain boundary for the PZT 20/80 case (Figure 3.5(a,d)), while *a*-domains are preferred for the PZT 45/55 case (Figure 3.5(b,e)). It is anticipated that the formation of the ferroelastic domain structures near the grain boundary are driven by strain accommodation for PZT 45/55. For PZT 20/80, the energy required to form charged defects is lower than for Zr-rich samples due to the decreased bandgap,[110] leading to the formation of *b*-domains to compensate the presence of local charge. Conversely, the larger bandgap for PZT 45/55 makes it more difficult to compensate highly charged domain walls, with the result that *a*-domains will be preferred over *b*-domains at the grain boundary. Evidence of charge carriers in PZT 20/80 is provided by high field hysteresis measurements showing an

increased loss compared to PZT 45/55 (see Figure 3.9). The influence of electric field on domain structure was previously determined to decay within 100 nm of a charged grain boundary,[111] indicating that any charge accumulation at the grain boundary is quickly compensated by the local domain structure.

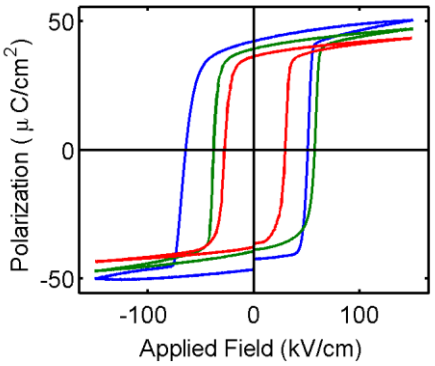

Figure 3.9: High field polarization – electric field hysteresis for various PZT compositions. Hysteresis measurements for PZT 52/48 (red), PZT 45/55 (green), and PZT 20/80 (blue).

Comparison between the domain structures of PZT 20/80 before and after poling in Figure 3.5(a,d) indicates that a decreased concentration of *b*-domains is present within 500 nm of the grain boundary after poling. To better understand the poling process, consider a *b*-domain near the grain boundary on poling. Due to the elastic constraints imposed by the substrate, the *b*-domain is unable to completely switch to *c*-domain. However, by moving the domain to intersect the grain boundary, the total volume of *c*-oriented polarization will increase by decreasing the *b*-domain concentration *adjacent* to the grain boundary, as shown in Figure 3.5(d). In some regions, the *b*-domains may be completely removed. A schematic illustrating this is shown in Figure 3.10. In contrast, *a*-domains move nearly parallel to the grain boundary, such that no volume can be converted to *c*-orientation in the same manner.

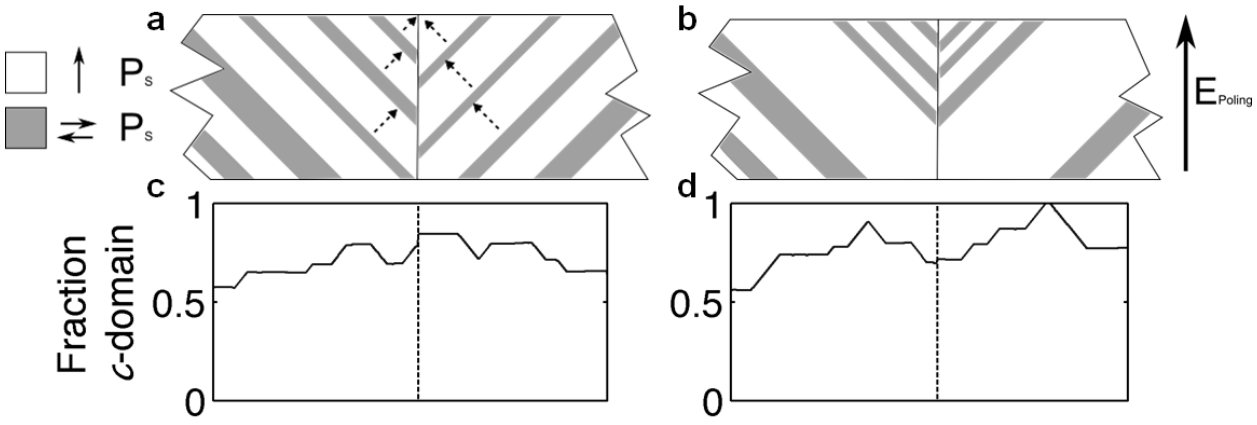

Figure 3.10: Proposed domain wall motion in PZT 20/80.

Schematic of how the c-domain volume near the grain boundary increases when poled with an electric field in the c-direction. (a) The unpoled domain structure with dotted arrows showing the direction of domain movement on (b) poling. Shaded regions indicate b-domains while white regions indicate c-domains. (c,d) c-domain fraction with distance from the grain boundary (c) before and (d) after poling.

No global minimum in the nonlinear response is observed at the grain boundary for PZT 20/80. Rather, a striped pattern in the nonlinear response is evident; the striping is not observed far from the grain boundary (Figure 3.11), although clustering of high and low response regions is evident. It is likely that the striped nonlinear response is due to changes in the domain structure associated with accommodation of the strain and electric fields at the grain boundary. Although the domain structure is unknown for the region in which the nonlinear response was collected, comparison can be made between the *average* nonlinear response and *average* domain structure at specific distances from the grain boundary.

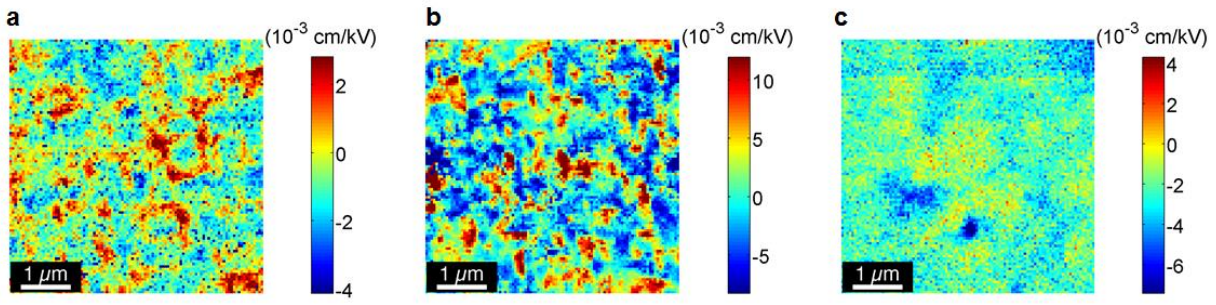

Figure 3.11: Nonlinear local response for various PZT compositions.

Nonlinear response quadratic / linear maps measured far from the grain boundary for various compositions (a) PZT 20/80, (b) PZT 45/55, and (c) PZT 52/48.

For PZT 20/80, a maximum in nonlinear response occurs in Figure 3.5(j) at ~360 nm to either side of the grain boundary, similar to that observed for PZT 45/55.[2] The domain structure for the poled region in Figure 3.5(d) shows that the maximum in nonlinear response corresponds to the edge of a region primarily consisting of *c*-polarization, where *a*- and *b*-domains intersect the substrate. One possibility is that the maximum in nonlinear response results because the 90º domain walls can move irreversibly into the *c*-polarized region due to reduced interaction with other 90º domain walls. Contributions from 180º domain wall motion, if present within the large *c*-polarized region, may further increase the nonlinear response as described elsewhere.[19], [112] Furthermore, a minimum occurs in the nonlinear response in Figure 3.5(j) at ~650 nm to either side of the grain boundary. At this distance, Figure 3.5(d) shows an increased volume fraction of in-plane polarization relative to regions closer to the grain boundary. A decreased nonlinear response when a larger number of 90º domain walls are present suggests 90º domain wall – domain wall pinning.

A similar maximum is observed near the grain boundary for PZT 52/48 in Figure 3.5(l). No variation in domain structure or configuration can be identified in Figure 3.5(f) due to the

small domain size. However, the maximum in nonlinear response corresponds to the introduction of 180º domain walls in Figure 3.5(i). Although the PFM data were collected on an unpoled region, it is anticipated that some variation in the average domain structure through the thickness of the film is still present at this position after poling.

3.5 Conclusions

A 24º tilt grain boundary was found to have maximum influence on pinning domain wall movement for {001} oriented epitaxial PZT 45/55, followed by PZT 52/48 and PZT 20/80. The reduced influence of the grain boundary on pinning PZT 52/48 was attributed to the higher domain wall density accommodating the local strain and electric fields. The effect of the grain boundary on domain wall motion for PZT 20/80 was more complex, with alternating low and high nonlinear response as a function of distance from the grain boundary associated with the local domain structure.

Domain wall pinning was attributed to the local elastic and electric fields at the grain boundary, as shown in the phase field model, and the local domain structure, observed by TEM and PFM. There is a strong indication that domain wall – domain wall pinning plays an important role in the evolution of global properties in ferroelectric materials. Such a combination of characterization techniques can be used to study other pinning sources, such as defect dipoles and isolated dislocations.

This work provides insight for the development of macroscopic properties from the nanoscale properties in multiple material systems, including ferromagnets and ferroelastics. The results displayed here can be used as a starting point to model the behavior of domain wall interactions and the evolution of functional properties in polycrystalline materials.

Chapter 4: Domain Wall Motion across Various Grain Boundaries in Ferroelectric Thin Films

Domain wall movement at and near engineered 10º, 15º, and 24º tilt and 10º and 30º twist grain boundaries was measured by band excitation piezoresponse force microscopy for $Pb(Zr,Ti)O_3$ films with Zr/Ti ratios of 45/55 and 52/48. A minimum in nonlinear response was observed at the grain boundary for the highest angle twist and tilt grain boundaries, while a maximum in nonlinear response was observed at the 10º tilt grain boundaries. The observed nonlinear response was correlated to the domain configurations imaged in cross section by transmission electron microscopy.

4.1 Introduction

In order to adequately model the properties of polycrystalline piezoelectric materials, knowledge of the way that individual grain boundaries influence the domain configuration and its mobility is required. Previous work has indicated that for 24º tilt grain boundaries in {001} lead zirconate titanate (PZT) films, the pinning of domain wall motion is strongly dependent on the composition and, thus, the ferroelastic strain.[113] However, the effect of grain boundaries on domain wall motion has not yet been systematically studied for a broader range of grain boundary orientations.

Various defects have been shown to pin domain wall motion and provide a reduced energy for domain nucleation. For example, transmission electron microscopy (TEM) and piezoresponse force microscopy (PFM) studies have indicated that dislocations,[33], [114] 90º

domain walls,[40], [41] defect dipoles[35], [36] and point defects[34] will pin domain walls in PZT. Domain nucleation has been observed to occur at the film/electrode interface[33] or 90º domain walls,[115] and phase field models indicate that domains may nucleate at grain boundaries and triple points.[49], [74]

It is well known that grain boundaries act to pin domain walls.[2], [16], [26], [37]–[39], [72], [75], [76], [91], [116] X-ray diffraction has shown ferroelastic domain wall pinning by intergranular elastic clamping.[39] Global dielectric and piezoelectric measurements exhibit decreased domain wall motion with decreasing grain size, indicating either pinning by grain boundaries[16], [26], [75], [76], [91] or increased domain wall – domain wall pinning due to the domain size decreasing with the square root of grain size.[38], [72] Recent results by PFM have shown reduced domain wall motion in the vicinity of grain boundaries.[2] Switching spectroscopy PFM studies on 200 nm epitaxial {001} $BiFeO_3$ coupled with phase field modeling indicates that a 24º grain boundary acts to pin domain walls, while at the same time reducing the nucleation energy for new domain formation. Both effects were attributed to the electric field developed at the grain boundary rather than the strains due to crystallographic mismatch.[37], [116]

The strain and electric fields at grain boundaries have been shown to result in correlation of domain structure between adjacent grains in $BaTiO_3$ and poled PZT ceramics,[8], [72], [98] suggesting the possibility of cooperative domain wall motion. PFM measurements of correlated switching across multiple grains further support this (See previous 2 chapters).[64] Studies of martensitic transformations indicate that a strong preference for strain-matched domain structures is a general rule for many materials systems.[14], [117], [118]

First principle modeling has been harnessed to understand the role of grain boundaries on the functional properties of materials. This includes studies of the strain,[119] electronic structure and defect formation energy,[120] and domain structure[50] at grain boundaries. However, further experimental information on the role played by grain boundaries in domain switching is essential to develop a stronger model on the interplay of defects with domain motion.[121]

Variation in the dielectric and piezoelectric properties between films in different orientations is expected due to material anisotropy.[108], [122], [123] Additionally, the Rayleigh parameters may also be anisotropic. For a random domain state, the film will have $\infty\infty m$ Curie symmetry. Poling prior to piezoelectric measurements changes the Curie symmetry to ∞m, providing a unique polar direction. However, the poling direction relative to the crystallographic axes is known to be important in some single crystals due to polarization rotation from the zero field domain configuration.[124], [125] Both this, and the equilibrium domain structure, should have an effect on domain wall motion.[126]–[128]

Since a myriad of grain boundaries are found in polycrystalline ceramics, it is essential to measure the dielectric and piezoelectric properties of multiple types of grain boundaries. To provide models for some orientations, films were grown on $SrTiO_3$ bicrystal substrates prepared with 10º and 15º tilt grain boundaries (Toplent Photonics Ltd., Sydney, Australia) and 10º and 30º twist grain boundaries (Crystal GmbH, Berlin, Germany). For a crystal with [010] perpendicular to the grain boundary, a tilt grain boundary involves rotation about [001] or [100], whereas a twist grain boundary involves rotation about [010]. A schematic distinguishing these two families of grain boundaries is shown in Figure 4.1. Tilt and twist grain boundaries are

expected to influence material properties in different ways, so samples prepared on tilt and twist bicrystal substrates were measured for rhombohedral (near MPB) and tetragonal PZT films.

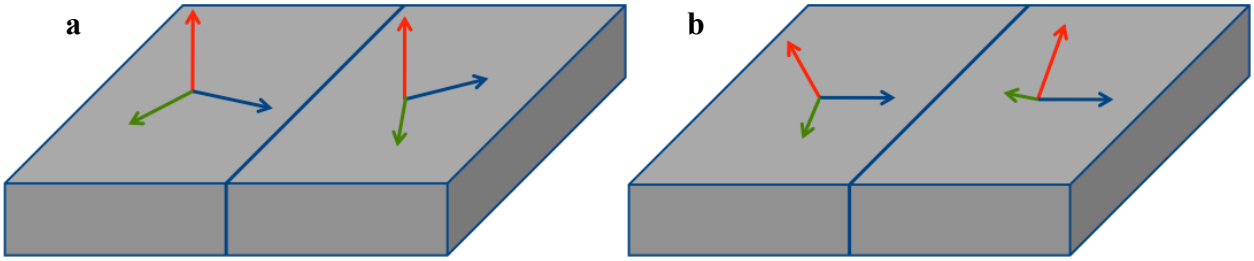

Figure 4.1: Types of grain boundaries.

Schematics of (a) tilt and (b) twist grain boundaries. The red arrow indicates the [00l] direction. The other two arrows are [100] and [001].

4.2 Materials & Methods

The influence of grain boundaries on the nonlinear response is expected to be different for tetragonal and rhombohedral ferroelectric phases due to varying domain structures developing at the grain boundary to compensate spontaneous strain and polarization. Therefore, both tetragonal 45/55 PZT and rhombohedral 52/48 PZT films were grown on $SrTiO_3$ bicrystals. Sample preparation is described elsewhere.[2] PZT films were grown by pulsed laser deposition on $SrTiO_3$ bicrystals with a 60 nm thick $SrRuO_3$ bottom electrode. It is noted that no significant variation in the width of reduced response with thickness was observed for PZT 45/55 thin films on 24º tilt bicrystals.[2] The PZT was etched alternatively with BOE 10:1 and 36% w/w HCl solutions to expose the $SrRuO_3$. Photolithography (Clariant Corporation AZ5214E resist, Karl Suss MA/BA6 contact aligner) followed by sputter deposition (Kurt Lesker CMS-18) of 50nm Pt was used to define top electrodes crossing the grain boundary (via liftoff). Pt was also deposited on the substrate backside after polishing to a mirror finish to aid in finding the bicrystal boundary

for BE-PFM. Samples were packaged (Spectrum Semiconductor Materials, Inc. CCF04002) on pieces of Si such that the top surface of the specimen was flush with the top of the package and both top and bottom electrodes were wirebonded (Kulicke & Soffa Industries, Inc. iBond 5000-Wedge) so that the electrodes could be driven during the BE-PFM measurements. During the BE-PFM measurements the drive signal was applied to the bottom electrode while the top electrode and tip were both grounded.

X-ray diffraction (Philips Pro MRD) prior to photolithography was used to insure phase purity. Phi scans on the PZT 101 peak confirmed epitaxy on both sides of the grain boundary. For the specimens with a twist grain boundary, phi scans were conducted while repositioning omega and chi every 5-10º in phi so that the film 101 was never more than 0.65º out of alignment. Capacitance was measured (HP 4284A Precision LCR) with increasing *ac* field at 300 kHz to determine the dielectric nonlinear response under conditions similar to BE-PFM. Polarization – electric field measurements (Radiant Multiferroic Tester) were made to assess the coercive field and remanent polarization. A double beam laser interferometer (aixACCT aixDBLI) was used to monitor the net piezoelectric coefficient in order to determine poling conditions prior to BE-PFM measurements.

BE-PFM (Asylum Research Cypher, Nanosensors PPP-EFM) was conducted at the Center for Nanophase Materials Science at Oak Ridge National Laboratory.[1], [31], [59], [60], [65] Samples were poled at 310 kV/cm for 30 min (PZT 45/55) and 160 kV/cm for 30 min (PZT 52/48) in the direction of imprint and aged for 30 min prior to BE-PFM measurements. The piezoelectric Rayleigh response was made under increasing *AC* electric field to 18.6 kV/cm (PZT 45/55) and 22 kV/cm (PZT 52/48) at the resonance frequency of the tip (~300 kHz). For all samples, the excitation waveform was chosen to minimize nonlinearities associated with the tip

contact, while maximizing signal to noise ratio. Maps were collected with 100 x 100 pixels on a 5 x 5 μm region crossing the grain boundary and ~5 mm to either side of the grain boundary.

For all samples, the BE-PFM measurements were made to fields beyond the Rayleigh regime in order to increase the amplitude of the piezoelectric strain. Therefore, reported values of nonlinear response are the ratio of quadratic to linear coefficients of the response with electric field normalized by the thickness of the film in units of cm/kV, or $\frac{1}{2}\cdot\alpha_d/d_{33,init}$.[1] Low nonlinear response was defined as being more than half a standard deviation below the mean film response, with cluster size far from the grain boundary reported as equivalent circular diameters. The width of decreased nonlinear response at the grain boundary was calculated using three different methods, similar to previous measurements on 24º tilt 20/80, 45/55, and 52/48 PZT films.[113] A description of the methods used to calculate the width of decreased nonlinear response is described next. The data reported herein is the mean of all calculated widths of influence for each sample.

The width of influence of the grain boundary was determined by three methods, discussed in Chapter 3. Values for all three methods are reported for all films in Table 4.1. The width of influence reported in the text is the mean of all values excluding zeros from method 2. For the case where a strong increase in the nonlinear response is observed at the grain boundary, negative values were reported by method 3, which is the only method able to identify a maximum in nonlinear response. The confidence in reported influence was chosen to cover the range of width of influence from all methods. The analysis for PZT 45/55 tilt bicrystals are shown in Figure 4.2, Figure 4.3 contains the analysis for PZT 52/48 tilt bicrystals, and the analysis for all twist bicrystals is reported in Figure 4.4.

Table 4.1: Methods for analyzing nonlinear response for various grain boundary angles. Width of reduced nonlinear response at the grain boundary using each of 3 analysis methods. Positive values indicate a decrease in the nonlinear response while negative values indicate an increase in the nonlinear response.

Composition & Angle	Method 1: Clustering	Method 2: 40 Pixels	Method 3: 25% Std	Reported Influence
45/55 24º Tilt	0.722±0.056	0.870±0.044	0.837±0.041	0.81±0.09
45/55 15º Tilt	0.101±0.032	0	0	0
45/55 10º Tilt	0.053±0.033	0	–1.016±0.038	–1.02±0.04
45/55 30º Twist	0.296±0.039	0.253±0.050	0.355±0.038	0.30±0.06
45/55 10º Twist	0.252±0.045	0.309±0.071	0.343±0.037	0.30±0.05
52/48 24º Tilt	0.429±0.088	0.421±0.056	0.476±0.016	0.44±0.04
52/48 15º Tilt	0.104±0.036	0	0.358±0.058	0.23±0.13
52/48 10º Tilt	0	0	–0.787±0.014	–0.79±0.01
52/48 30º Twist	0.341±0.024	0.378±0.018	0.383±0.008	0.37±0.03
52/48 10º Twist	0.130±0.033	0	–0.303±0.052	0

In order to further elucidate the impact of grain boundaries on domain wall motion, TEM was conducted by Huairuo Zhang and Ian Reaney on poled and unpoled specimens of 30º twist grain boundaries for both compositions. Specimens were prepared with a FEI Helios NanoLab 660 DualBeam Focused Ion Beam (FIB) / Scanning Electron Microscope (SEM) platform to avoid alteration of the surface domain structure by conventional mechanical grinding.[84], [85] The grain boundary was located by SEM followed by FIB milling of cross-sectional TEM specimens containing the grain boundary. A field emission JEOL 2010 TEM/STEM and a JEOL 2010 TEM operated at 200 kV were used to collect micrographs. The specimens were rotated using a Gatan 925 double tilt rotation analytical holder to orient the grain boundary vertically in the CCD camera image. The 30º twist bicrystal specimens were tilted to the symmetric condition with each grain 15º off the [100] zone axis for comparing the domain structures across the grain boundary.

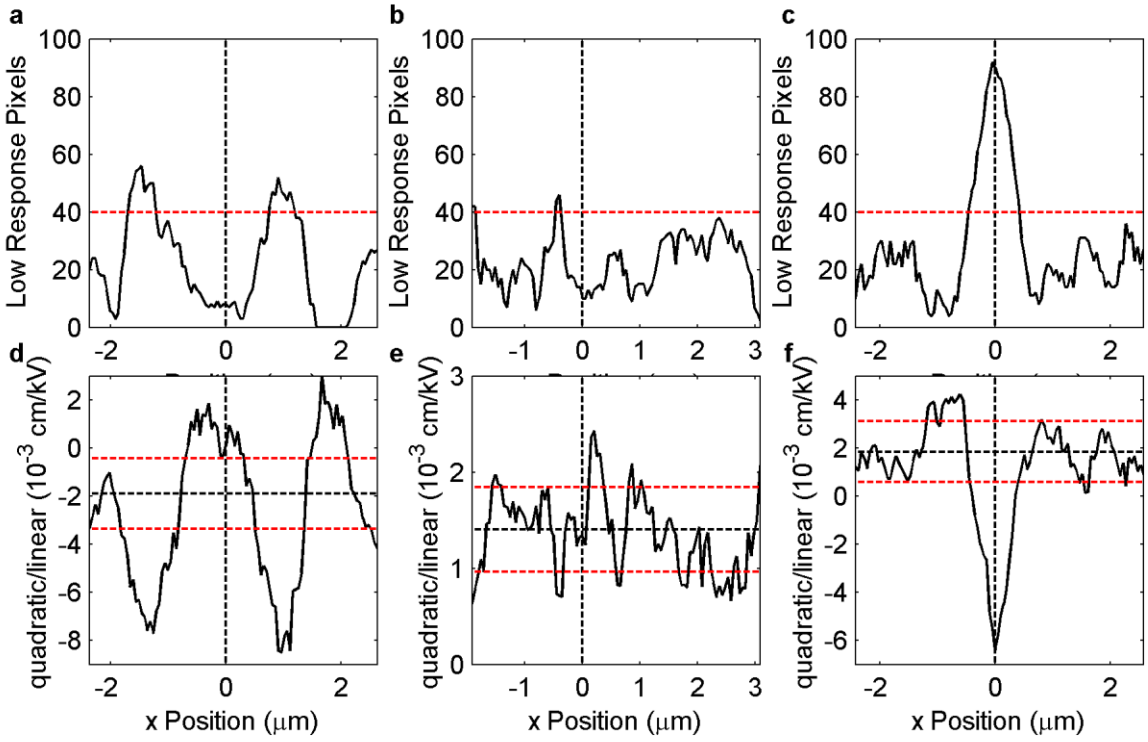

Figure 4.2: Low nonlinear response determined by methods 2 and 3 for tilt PZT 45/55.

(a-c) Total number of low response pixels as a function of distance from the grain boundary and (d-f) average nonlinear response as a function of distance from the grain boundary for PZT 45/55 (a,d) 10º, (b,e) 15º, and (c,f) 24º tilt grain boundaries. The grain boundary is marked with a vertical black line while the horizontal red lines indicate cutoff values of 40 pixels low response for a-c and ±25% standard deviation from the film average for d-f.

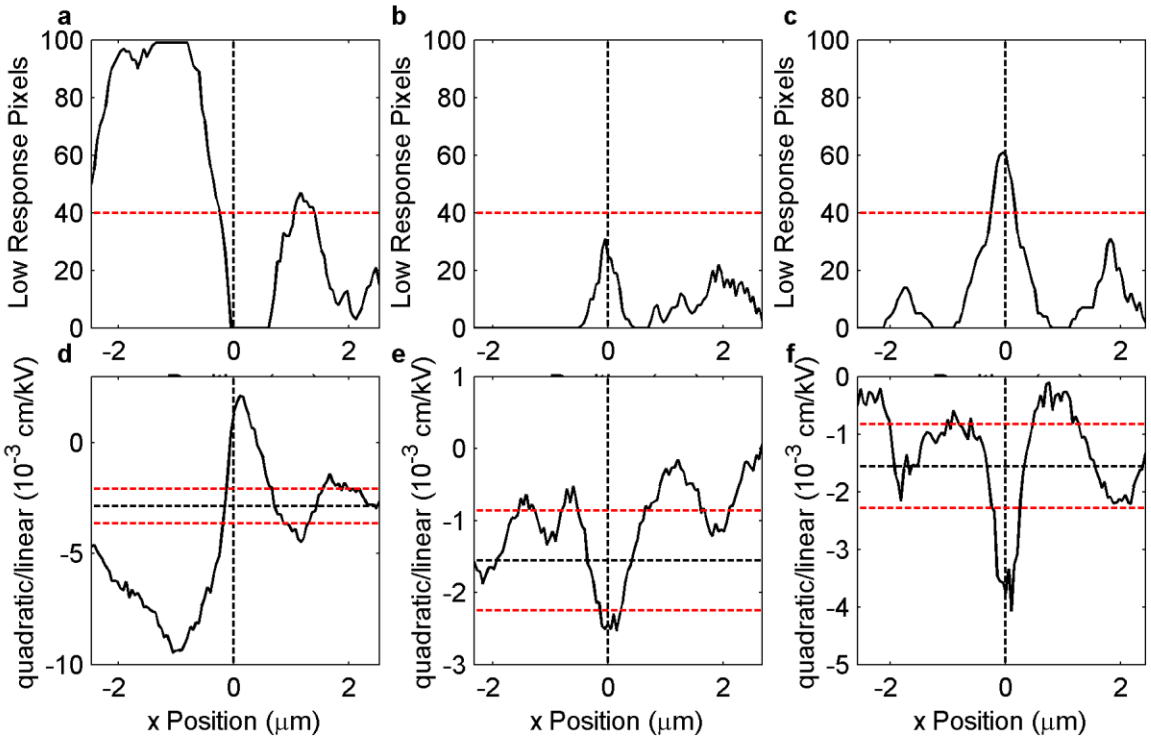

Figure 4.3: Low nonlinear response determined by methods 2 and 3 for tilt PZT 52/48.

(a-c) Total number of low response pixels as a function of distance from the grain boundary and (d-f) average nonlinear response as a function of distance from the grain boundary for PZT 52/48 (a,d) 10º, (b,e) 15º, and (c,f) 24º tilt grain boundaries. The grain boundary is marked with a vertical black line while the horizontal red lines indicate cutoff values of 40 pixels low response for a-c and ±25% standard deviation from the film average for d-f.

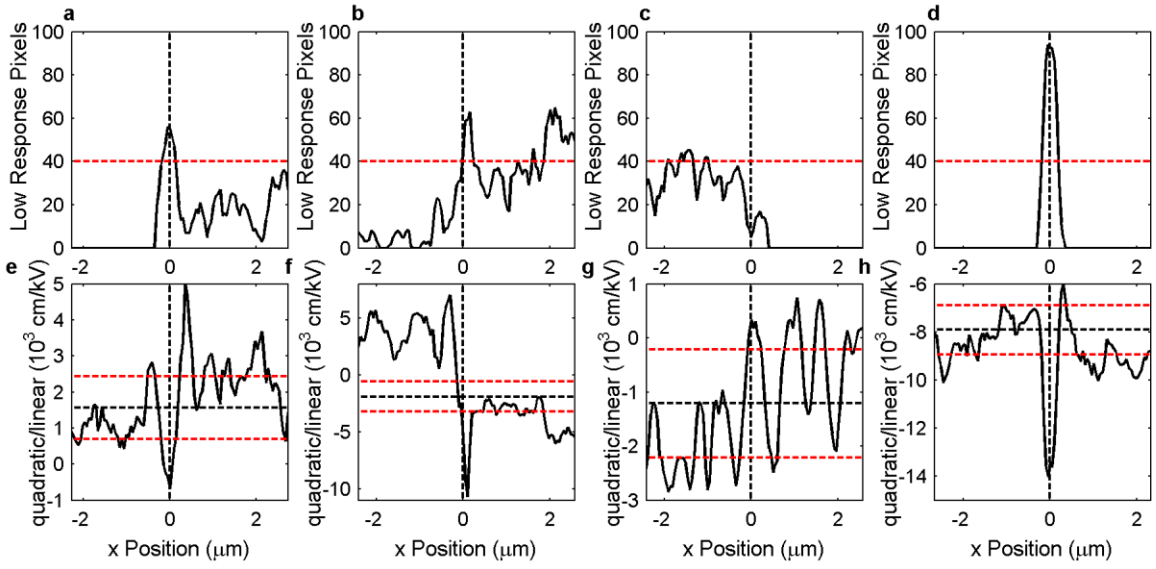

Figure 4.4: Low nonlinear response determined by methods 2 and 3 for twist grain boundaries.

(a-d) Total number of low response pixels as a function of distance from the grain boundary and (e-h) average nonlinear response as a function of distance from the grain boundary for (a,b,e,f) PZT 45/55 and (c,d,g,h) PZT 52/48 twist grain boundaries. (a,c,e,g) 10º, (b,d,f,h) 30º. The grain boundary is marked with a vertical black line while the horizontal red lines indicate cutoff values of 40 pixels low response for a-d and ±25% standard deviation from the film average for e-g.

4.3 Results

All films showed single perovskite phase development and epitaxial growth on both halves of the bicrystal within the detection limits of XRD. Additionally, dielectric and ferroelectric properties showed high quality films, with a modest level of imprint developing for most samples. Due to the misorientation of the crystallographic <001> direction relative to the surface normal for films deposited on symmetric twist bicrystals, variation in the permittivity, remanent polarization, and coercive field were observed. The full width at half maximum of the

002 peak, the film thickness, the low field permittivity and loss, and the degree of imprint are listed in Table 4.2.

Figure 4.5 shows maps of nonlinear response collected for PZT 45/55 films on different angle tilt grain boundaries. It is evident that the 24º grain boundary shows the largest width of reduced nonlinear response, while a maximum in nonlinear response is found at the 10º grain boundary. The 15º grain boundary appears to have a comparable influence to other pinning sources. Similar results are shown in Figure 4.6 for PZT 52/48 films, where a definite minimum in nonlinear response exists for the 24º grain boundary, the 15º grain boundary shows a small width of reduced nonlinear response, and a maximum in nonlinear response is observed at the 10º grain boundary.

Table 4.2: X-ray diffraction and electrical data for all films.

Film thickness, full width at half maximum of the PZT 002 XRD peak, low field permittivity and loss for all films studied.

Composition & Angle	Thickness (nm)	PZT 002 FWHM (ºω)	ε_r (10 kHz, 30 mV)	Tan δ (%)	$V_c^+ - V_c^-$ (V)
45/55 24º Tilt	425	0.69	488	1.3	0.83
45/55 15º Tilt	420	0.59	509	3.1	–0.71
45/55 10º Tilt	882	0.63	461	2.5	0.04
45/55 30º Twist	458	0.82	631	3.1	–0.45
45/55 10º Twist	520	0.74	585	2.8	–0.86
52/48 24º Tilt	791	0.12	467	2.4	–0.49
52/48 15º Tilt	838	0.12	597	3.0	0.79
52/48 10º Tilt	583	0.15	597	5.1	–0.41
52/48 30º Twist	432	0.57	567	4.2	–0.11
52/48 10º Twist	390	0.24	629	5.2	–0.91

Maps crossing the PZT 45/55 and PZT 52/48 twist grain boundaries are presented in Figure 4.7. A strong minimum in nonlinear response is present at the grain boundary for the 30º

twist grain boundaries in both PZT 45/55 and PZT 52/48. The 10º twist grain boundaries have higher nonlinear response at and near the grain boundary than the 30º twist grain boundaries, as quantitatively shown in Figure 4.7(e-h). In fact, the 10º twist grain boundary for PZT 52/48 shown in Figure 4.7(c,g) appears to have no significant influence on the nonlinear response relative to other pinning sites present in the film. Calculated widths of reduced nonlinear response are presented in Table 4.3. A positive number indicates reduced nonlinear response while a negative number indicates increased nonlinear response at the grain boundary.

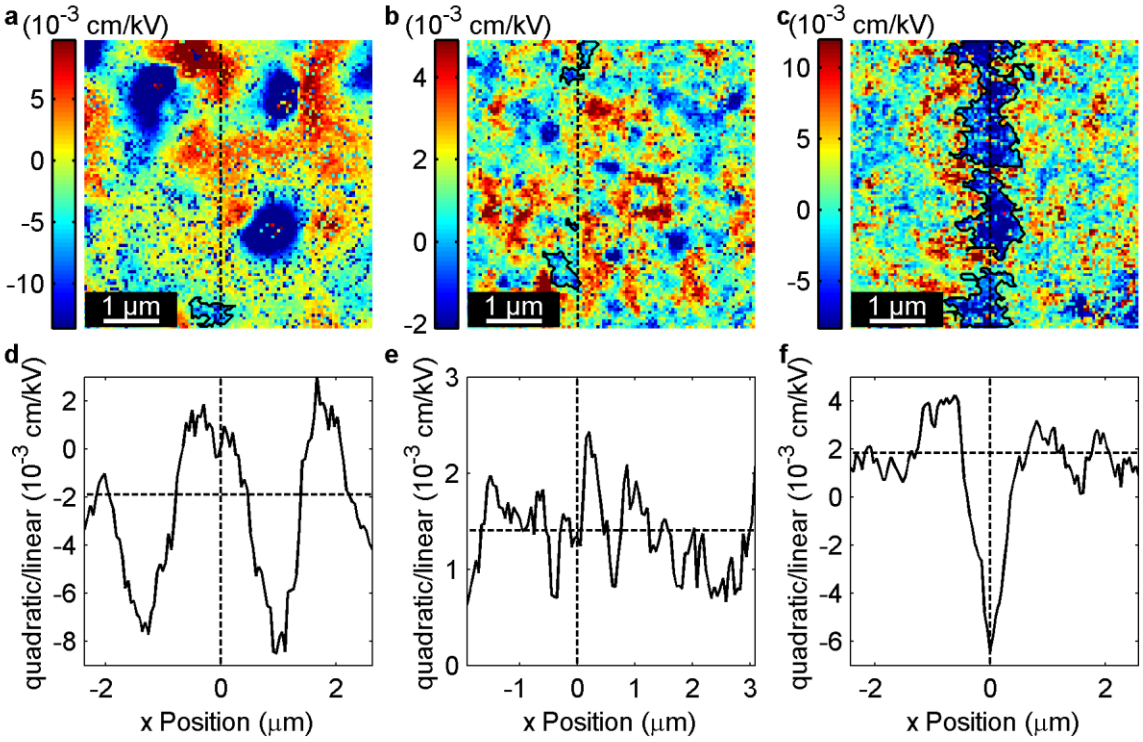

Figure 4.5: Nonlinear response for PZT 45/55 for tilt angle grain boundaries.

Maps of the (a-c) nonlinear response and (d-f) mean nonlinear response parallel to the grain boundary for PZT 45/55 tilt bicrystals. The grain boundary is denoted by the vertical dashed line. (a,d) 10º, (b,e) 15º, (c,f) 24º. Horizontal lines (d-f) indicate the film mean response.

In order to better understand the difference in domain configuration between twist and tilt grain boundaries, TEM diffraction contrast methods were used to image the domain structure at and near grain boundaries. Micrographs were collected for 30º twist grain boundaries of the PZT 45/55 and PZT 52/48 films; previous studies[113] already report the domain structure near tilt grain boundaries. As described elsewhere for tetragonal films,[2] *a*-domains are those that have their polarization nearly parallel to the grain boundary and rotated 15º from the plane of the film, *b*-domains have the polarization nearly perpendicular to the grain boundary, and *c*-domains have polarization rotated 15º from the normal to the film surface.

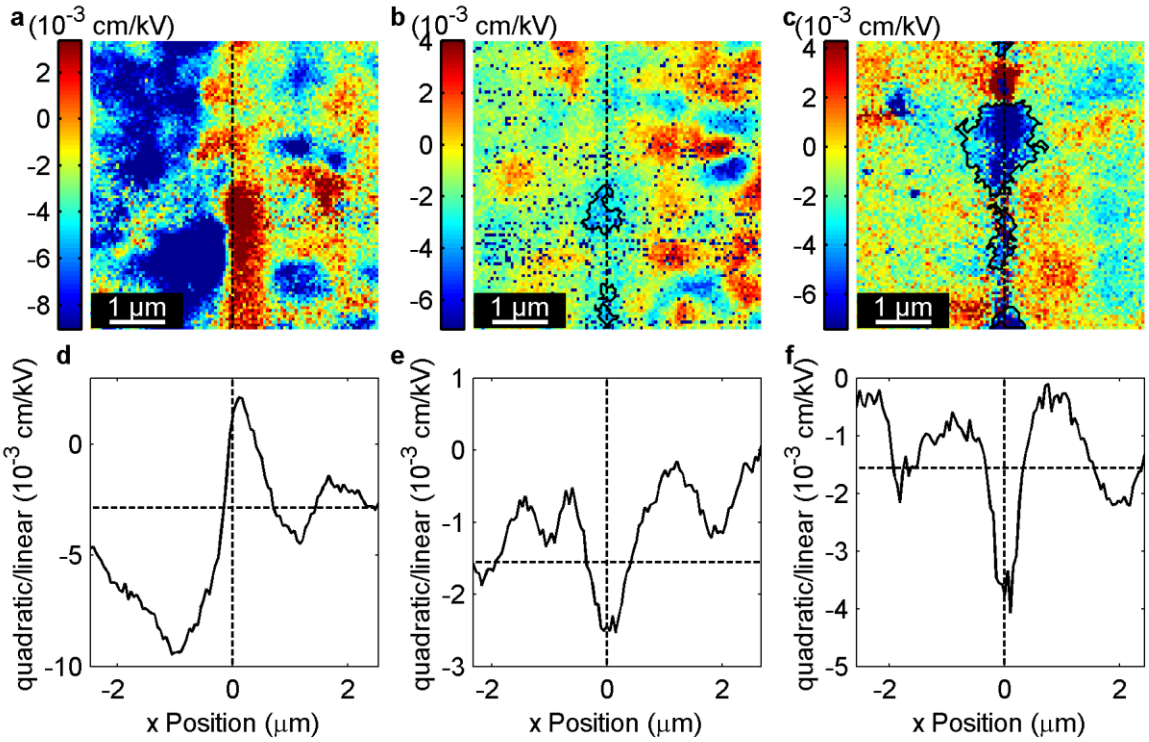

Figure 4.6: Nonlinear response for PZT 52/48 for tilt angle grain boundaries.

Maps of the (a-c) nonlinear response and (d-f) mean nonlinear response parallel to the grain boundary for PZT 52/48 tilt bicrystals. The grain boundary is denoted by the vertical dashed line. (a,d) 10º, (b,e) 15º, (c,f) 24º. Horizontal lines (d-f) indicate the film mean response.

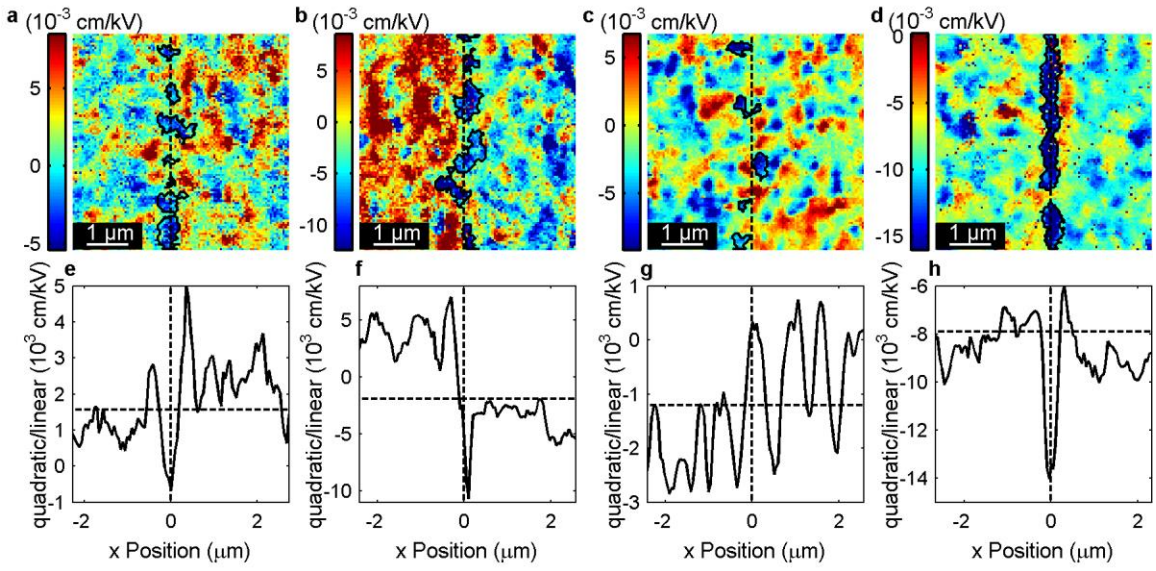

Figure 4.7: Nonlinear response for twist angle grain boundaries.

Maps of the (a-d) nonlinear response and (e-h) mean nonlinear response parallel to the grain boundary for PZT 45/55 (a,b,e,f) and PZT 52/48 (c,d,g,h) twist bicrystals. The grain boundary is denoted by the vertical dashed line. (a,c,e,g) 10º, (b,d,f,h) 30º. Horizontal lines (d-f) indicate the film mean response.

The cross-section micrographs for the twist grain boundary films are provided in Figure 4.8(a,b) before and (c,d) after poling. For PZT 45/55 films, one side of the grain boundary exhibits small domains while the other has larger domains prior to poling (Figure 4.8(a)), while large domains are observed after poling (Figure 4.8(c)). No significant variation in the domain wall density is observed for either case near the grain boundary compared to farther away. No large *a*-domains are observed at the grain boundary as were observed for the 24º tilt grain boundary.[2] Instead, *b*- and *c*-domains comparable in size to those far from the grain boundary are present. In the case of PZT 52/48, a tweed domain structure is observed before and after poling (Figure 4.8(b,d)). The small domain size (~6 nm) is attributed to low domain wall energy

for compositions near the morphotropic phase boundary. The origin of the bending of the grain boundaries away from the substrate normal is not known.

Table 4.3: Rayleigh parameters for all films.

Dielectric nonlinearity, mean piezoelectric nonlinear response, mean size of low response clusters far from the grain boundaries, and mean width of reduced response at the grain boundary for all films studied.

Composition & Angle	$\alpha_e/\varepsilon_{init}$ (10^{-3} cm/kV)	BE-PFM Nonlinearity		Low Response Clusters (μm)	GB Reduced Response (μm)
		Mean (10^{-3} cm/kV)	Std. Dev. (10^{-3} cm/kV)		
45/55 24º Tilt	15.9±0.1	1.84	5.06	0.27±0.05	0.81±0.09
45/55 15º Tilt	13.5±0.1	1.41	1.76	0.25±0.04	0
45/55 10º Tilt	15.9±0.8	-1.89	5.86	0.25±0.06	–1.02±0.04
45/55 30º Twist	12.9±0.1	-1.90	5.26	0.18±0.02	0.30±0.06
45/55 10º Twist	12.8±0.1	1.56	3.49	0.23±0.05	0.30±0.05
52/48 24º Tilt	3.8±0.1	-1.56	2.92	0.23±0.06	0.44±0.04
52/48 15º Tilt	24.1±0.6	-1.56	2.78	0.22±0.03	0.23±0.13
52/48 10º Tilt	25.6±0.6	-2.84	3.10	0.37±0.12	–0.79±0.01
52/48 30º Twist	40.1±0.9	-7.91	4.07	0.29±0.04	0.37±0.03
52/48 10º Twist	31.4±1.2	-1.21	3.98	0.22±0.03	0

4.4 Discussion

It was found that only some of the grain boundary angles measured are significant pinning sources relative to other pinning sites in the film. Angles 15º and less in tilt angle grain boundaries have similar energy to other pinning sites in the films, as evident by the concentration of low response pixels being comparable to the film far from the grain boundary. However, the 24º tilt angle grain boundary for both PZT 45/55 and PZT 52/48 acts as a significant pinning site, with a notable increase in the concentration of low response pixels. For twist grain boundaries, 30º samples showed significant pinning while 10º for PZT 52/48 was comparable to other pinning sites.

In contrast to observations made on 24º tilt grain boundaries, Figure 4.5(d) and Figure 4.6(d) show an *increase* in the mean nonlinear response at the 10º tilt grain boundaries of both compositions. It is anticipated that there is a change in the local elastic and electric fields with grain boundary angle.[129] At all angles, the perturbation in the lattice energies will lead to a preference for domain walls at the grain boundary to accommodate the local strain and charge, represented schematically in Figure 4.9 and discussed further below.

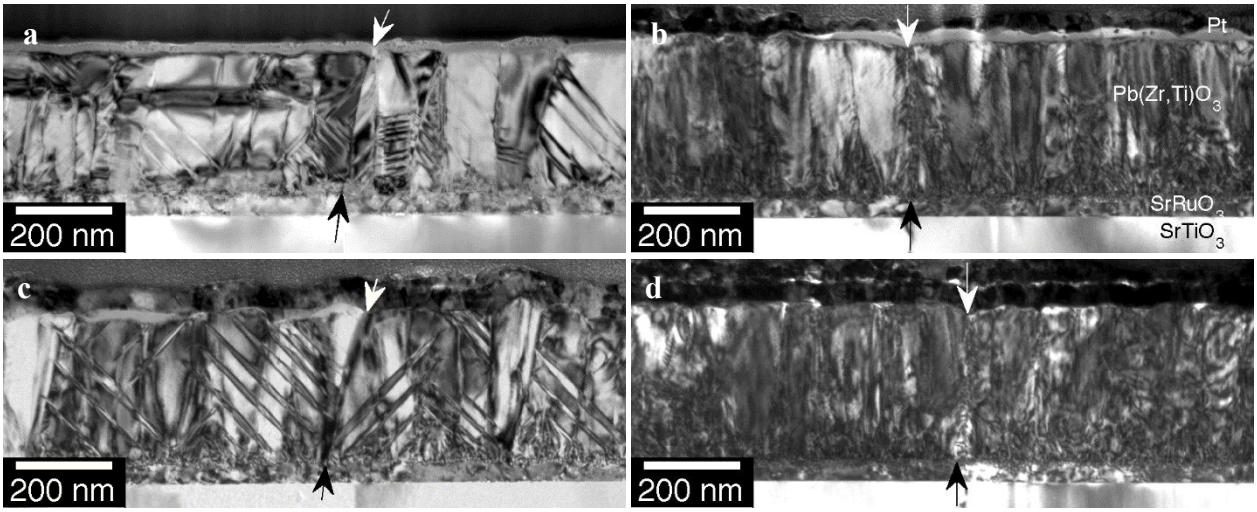

Figure 4.8: Cross-section TEM on twist grain boundaries.

Cross-section TEM of 30º twist grain boundaries in (a,c) PZT 45/55 and (b,d) PZT 52/48. (a,b) were collected prior to poling while (c,d) were poled and excited, with a similar domain structure to that measured by BE-PFM. Arrows at top and bottom of the film mark the grain boundary.

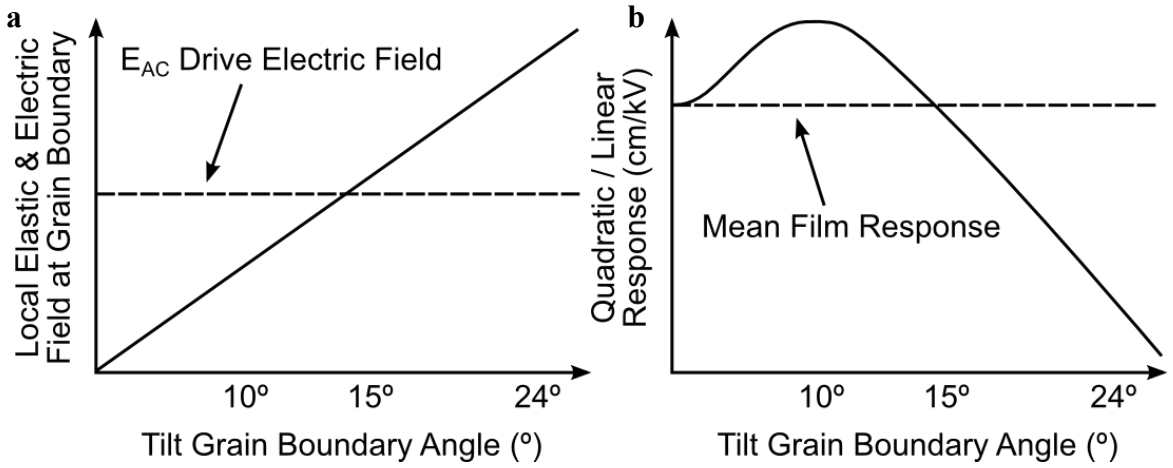

Figure 4.9: Schematic of grain boundary pinning energy

Schematic representation of the (a) local elastic and electric fields at the grain boundary relative to electrical excitation as a function of tilt grain boundary angle. The dashed line represents the electrical excitation. (b) The nonlinear response at the grain boundary as a function of tilt grain boundary angle. The dashed line represents the film average response far from the grain boundary.

At small angles, the energy pinning these domain walls is small relative to the drive voltage. This will result in significant, possibly cascaded, motion of domain walls, resulting in an increased nonlinear response relative to the film average. It is also possible that the domains at the grain boundary are removed at low fields but re-nucleate (due to the local elastic and electric fields at the grain boundary) upon removal of the drive electric field. This would also result in an increase in the nonlinear response at the grain boundary. Therefore, for the case of 10º tilt grain boundaries, an increase in the local nonlinear response is observed due to moderate electric fields irreversibly moving domain walls across the low pinning energy defect.

At intermediate angles, the energy pinning domain walls at the grain boundary is comparable to or slightly higher than the drive electric field. Domain walls will move under

electric excitation but will not be rewritten with every *ac* excitation. Therefore, a comparable response will be observed at the grain boundary relative to that observed far from the grain boundary. This case holds for the 10º twist and the 15º tilt grain boundaries studied here, where small variation in the nonlinear response and the cluster size was observed at the grain boundary relative to the film average.

At large grain boundary angles, the energy that pins domain walls at the grain boundary is large relative to the drive electric field. Domain walls are strongly pinned to the grain boundary, leading to a significant decrease in the nonlinear response. In addition, domain walls pinned at the grain boundary may pin adjacent domain walls (i.e. by preventing cascaded wall motion), leading to a larger width of reduced response for the case of 30º twist and 24º tilt grain boundaries.

The correct functional form for the variation in pinning energy of the grain boundary with angle in Figure 4.9 is unknown. Previous studies of grain boundary energy in metals indicate that a component of the grain boundary energy is the local strain energy, which varies according to Equation 4.3.[129]

$$E^{GB}(\theta) \propto \sin\theta\,[E_s \ln(\sin\theta)]/b \qquad \text{Equation 4.3}$$

In Equation 4.3, E^{GB} is the grain boundary energy, E_s is a fitting parameter for the strain energy, θ is the symmetric grain boundary angle, and b is the magnitude of the Burgers vector associated with dislocations at the grain boundary. Although grain boundaries can only be represented as arrays of dislocations for small angles, Equation 4.3 has been shown to hold well for large angle grain boundaries in metals.[129] Thus, it is anticipated that the strain component of the pinning energy of grain boundaries will vary with angle in a manner similar to that shown in Equation 4.3.

It is proposed that strain matching at the grain boundary creates a long-range (100 nm) impact on the domain structure and domain wall motion. Observations on 24º tilt grain boundaries indicate that the domain structure produced by the grain boundary influences the domain wall motion at intermediate distances (0.36 – 0.65 μm) from the grain boundary.[113] In contrast, no significant variation in domain wall density was observed near the 30º twist grain boundary compared to far away. For the twist grain boundaries, the homogeneity in domain wall density indicates that there is no long-range influence on the domain structure and, thus, on domain wall motion. The 30º twist grain boundaries act as pinning sites due to large local electric and elastic fields, but compared to 24º tilt grain boundaries have a decreased width influence on domain wall motion due to a homogeneous domain structure. One explanation for the long-range domain structure near the 24º tilt grain boundary in PZT 45/55 is the ability for domain walls on one side to intersect the grain boundary at the same position as domain walls on the other side to relieve local strain. For a 30º twist grain boundary there is a 30º misorientation between the {110}-type planes which prevents domain walls on each side of the grain boundary from intersecting the grain boundary in the same location and reduces the long-range influence of the grain boundary on the domain structure.

It is intriguing that the width of decreased nonlinear response is different for large angle tilt and twist grain boundaries. For example, comparisons of Figure 4.5(f) to Figure 4.7(f) and Figure 4.6(f) to Figure 4.7(h) shows that the 24º tilt grain boundaries have a larger width of reduced response than 30º twist grain boundaries. However, the twist boundaries produce a stronger reduction in the nonlinear response. This indicates that the perturbation in the potential energy landscape caused by a grain boundary is dependent on the details of the misorientation. Figure 4.10 illustrates the potential energy landscape near the grain boundary for three different

cases. Figure 4.10(a) represents the unperturbed potential energy, where domain walls are pinned by various pinning sites throughout the epitaxial film. Figure 4.10(b) represents a large angle tilt grain boundary with a wide and moderately deep potential energy well (along with the superimposed random variations from other pinning sources). Figure 4.10(c) represents a large angle twist grain boundary with a narrow and deep potential energy well. For all figures, the black line indicates the potential energy landscape while the red line represents the perturbation caused by the grain boundary. The depth of the potential energy well should decrease with decreasing grain boundary angle, resulting in the observed trend in magnitude and width of reduced nonlinear response with angle.

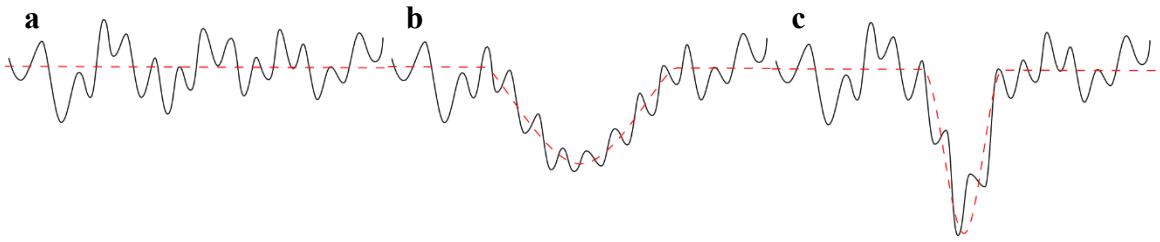

Figure 4.10: Grain boundary potential energy landscape.

Proposed potential energy landscapes for the (a) unperturbed state, (b) tilt grain boundary, and (c) twist grain boundary. The dashed red lines represent the average potential energy, while the black lines represent the potential energy landscape with other pinning sites present. (b,c) The grain boundary is located at the minimum in the red line.

4.5 Conclusions

The highest angle tilt grain boundaries were found to have a larger width of reduced nonlinear response when compared to the twist angle grain boundaries, while the smallest angle

tilt grain boundaries were found to have a maximum in the nonlinear response at the grain boundary. The reduction in domain wall motion for the highest angle tilt and twist grain boundaries was attributed to an increase in domain wall density to accommodate local elastic and electric fields. The different widths of reduced response for tilt and twist grain boundaries is believed to be associated with differences in the widths required for the local strain energy to decay. The small perturbation in pinning energy from the smallest angle tilt grain boundaries resulted in an increase in the local nonlinear response, which is believed to be due to a small pinning energy such that moderate electric fields will irreversibly move domain walls across the grain boundary.

Chapter 5: A-site Stoichiometry and Clustered Domain Wall Motion in Thin Film $Pb(Zr_{1-x}Ti_x)O_3$

Lead zirconate titanate (PZT) films with Zr/Ti ratios of 52/48 and 30/70 annealed at varying partial pressures of PbO within the perovskite phase field exhibited permittivities of 1150 and 600, respectively with loss tangents of 0.02. Many of the functional properties, including the permittivity, the Rayleigh coefficients, and the aging rates were found to be weakly dependent of the lead content in the single phase field. Minor polarization – electric field hysteresis loops and piezoelectric coefficient $e_{31,f}$ values after hot poling suggest that the $V''_{Pb} - V^{\cdot\cdot}_{O}$ defect helps stabilize the poled domain state. Measurements of the local nonlinear response show an increased low response cluster size with decreasing PbO content, indicating that PbO deficiency acts to reduce domain wall motion where it is already low.

5.1 Introduction

In thin film and bulk PZT, control of PbO content is essential for achieving the desired electrical and piezoelectric properties. Too much PbO may result in a PbO second phase in grain boundaries, causing high leakage and low electrode yield.[130]–[132] Too little PbO typically results in a Pb-poor cubic pyrochlore or fluorite second phase, which, while electrically insulating, has a lower permittivity and is not ferroelectric.[133] Volatilization of PbO is problematic during annealing (600-800ºC), and is only partially controlled for thin films through the use of rapid thermal annealing processes.[134], [135]

In thin films, PbO control has been achieved either by increasing the PbO content in the deposited film[134] (typically by 5-20% excess PbO in solutions for solution processing and in targets for physical vapor deposition) or by adding a PbO overcoat after the film has been prepared and heating to diffuse the PbO into the PZT film.[133], [136] Excess surface PbO can be removed using an acetic acid wash.[136] In both cases, the PbO content is essentially controlled by kinetics. Neither method is amenable to precise control of PbO defect concentrations.

The perovskite phase can accommodate nonstoichiometry in Pb content, with differing reports on the extent of solid solution.[137], [138] Point defects are known to contribute to ionic conductivity and can, in principle, increase electronic conductivity if they are compensated electronically. In bulk PZT, Prisedsky et al. determined that lead vacancies are compensated by oxygen vacancies and holes.[139], [140] A more general understanding of ionic defects and charge carriers in PZT films should lead to an improved understanding of breakdown and aging characteristics.[140], [141]

Point defects produce local electric and elastic fields. Indeed, in ultrathin films, PbO overpressure can be used to drive chemical switching of PZT films.[142] These local fields may influence domain wall motion.[25] Domain walls may be pinned by point defects or defect complexes. This would lead to a decreasing nonlinear response with increasing defect concentration.[21], [25] For example, defect dipoles have been reported to control imprint and pinching of hysteresis loops in acceptor-doped ferroelectric materials,[143] where the dipole associated with paired ionic defects influences the surrounding material, resulting in a local preferred polarization direction.[144] In contrast, the electric and elastic fields associated with individual point defects may also contribute to domain nucleation, creating local “soft” spots that act to preferentially nucleate domains near the defect.[145]–[147] This could result in an

increasing nonlinear response with increasing defect concentration due to a higher concentration of mobile domain walls present at low fields.[147]

The required lead partial pressure to obtain phase pure perovskite PZT was first measured by Härdtl and Rau.[148] It was found that solid PbO deposition controlled the upper limit of PbO partial pressure while PbO removal from $PbZrO_3$ controlled the lower PbO partial pressure limit as shown in Equations 5.1 and 5.2.

$$PbO_{(solid)} \leftrightarrow PbO_{(gas)} \qquad \text{Equation 5.1}$$

$$PbZrO_3 \leftrightarrow PbO_{(gas)} + ZrO_2 \qquad \text{Equation 5.2}$$

For the reactions in Equations 5.1 and 5.2, the equilibrium vapor pressures measured using the Knudsen cell method are reported in Equations 3 and 4.

$$\log p = -\frac{15030}{T} + 9.51 \qquad \text{Equation 5.3}$$

$$\log p = -\frac{13660}{T} + 7.15 \qquad \text{Equation 5.4}$$

In Equations 5.3 and 5.4, p is the PbO partial pressure in atm and T is temperature in K. The lower PbO partial pressure limit varies with the Zr/Ti ratio, with $PbTiO_3$ stable to a lower vapor pressure. For PZT films, it is known that a PbO deficient pyrochlore phase forms instead of pure ZrO_2.[134] Therefore, for the experiments in the present work, the pyrochlore – perovskite equilibrium was found for the higher Zr content film (PZT 52/48) and the same partial pressure was used for both PZT 30/70 and PZT 52/48.

Most PZT thin films are crystallized between 600 and 750 °C to provide sufficient energy for ionic diffusion within short time spans (1-5 minutes). In this work, an equilibration time of 1 hour at 670°C was estimated based on reports of reproducibly converting films from the pyrochlore to the perovskite phase after a 45 minute anneal at 650°C.[149] At 670ºC, the range of lead partial pressures that should promote single phase PZT is between 3.53×10^{-5} torr and 2.85×10^{-4} torr.

5.2 Materials & Methods

5.2.1 Furnace Design

In order to enable thermodynamic control of the lead content during high temperature processing, a rapid thermal annealing furnace with controlled lead overpressure was designed and built. The design of the furnace was guided by an arsine annealing furnace described elsewhere.[150] The system is composed of three parts: gas and precursor control, the processing chamber, and a burnout furnace for breakdown and capture of the metallorganic. Tetraethyl lead (TEL) (Gelest, Inc) was chosen as the precursor due to its common use as a lead precursor in MOCVD processes.[73], [151]–[154]

A schematic of the furnace is shown in Figure 5.1. Nitrogen is used as the carrier gas for the TEL. Nitrogen is introduced to a bubbler containing TEL in a temperature controlled bath (Lauda E200), then mixed with more nitrogen and oxygen in the desired proportions to control the lead overpressure and enable cracking of the precursor. Gas lines between the bubbler and the furnace are heated to 80°C to prevent condensation of TEL.

The process chamber is composed of a 6” outer diameter fused silica tube in an infrared heated furnace (Research Inc., ChamberIR). All parts except the carrier wafer and thermocouple are made out of fused silica to reduce absorption of infrared light and subsequent heating. The substrate holder was designed to hold a silicon carrier wafer in contact to the holder only at 3 points to reduce heat loss to the sample holder. Temperature is measured from underneath the Si carrier wafer via thermocouple. Glass frit is used on the exhaust side of the chamber to capture unused PbO prior to exiting the process chamber.

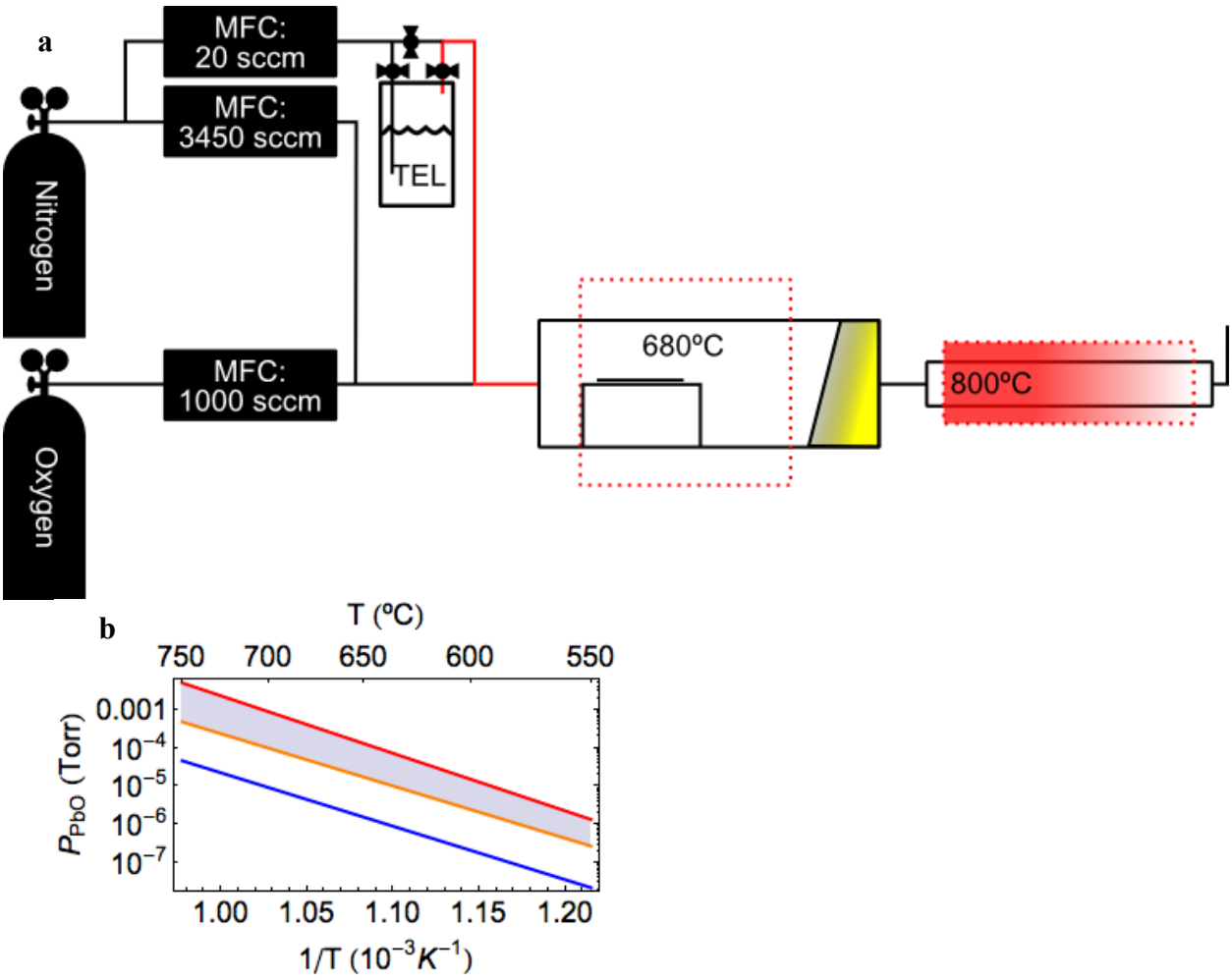

Figure 5.1: PbO atmosphere rapid thermal annealing furnace design.

(a) Schematic of PbO partial pressure controlled rapid thermal annealer (RTA). Lines connecting units represent ¼" gas lines, where the red gas lines are heated to 70ºC. Red dotted boxes indicate furnace hot zones. (b) The required partial pressure of PbO for equilibrium of $PbO_{(g)} \leftrightarrow PbO_{(s)}$ (red line), $PbZrO_3 \leftrightarrow PbO_{(g)} + ZrO_2$ (orange line), and $PbTiO_3 \leftrightarrow PbO_{(g)} + TiO_2$ (blue line) at various temperatures. The desired range for PZT perovskite equilibrium is the shaded region. Equations are from Härdtl et al.[148]

A 1” diameter tube furnace (Lindberg/Blue M Mini-Mite) held at 800ºC decomposed remaining metallorganic precursors. The tube filled with fiber refractory was used to capture any PbO particles generated; at over 3x the length of the furnace, the process gas cools to near room temperature prior to exhaust to the building exhaust system. The system is contained in a vented enclosure. Gas flow through the bubbler is interlocked to the enclosure doors to reduce likelihood of user exposure to TEL.

Flow rates necessary to achieve the desired partial pressure depend on the flow rate of all gases, the pressure in the bubbler, the pressure in the processing chamber, and the vapor pressure of TEL at the bubbler temperature. The pressure of the bubbler was assumed to be the same as that in the reaction chamber. Because each molecule of TEL contains one lead atom, the partial pressure of lead was assumed to be equivalent to that of TEL. The vapor pressure of TEL was previously measured by Buckler and Norrish[155] between 0-80 °C:

$$\log p = 9.428 - \frac{2938}{T} \qquad \text{Equation 5.5}$$

For Equation 5.5, p is TEL partial pressure in torr and T is temperature in K. Using a N_2 and O_2 flow of up to 5000 sccm and 1000 sccm, respectively, to dilute the TEL, required flow rates for N_2 through TEL for the desired partial pressure of PbO were determined as a function of bubbler temperature.

The amount of PbO required to change the vacancy concentration and achieve equilibrium throughout the sample was calculated for 4” diameter wafers with a 1 μm thick PZT with a density of 7.6 g/cm^3. About 10^{-4} mols of PbO are present in the sample. Thus, in order to change the defect concentration by +1%, approximately 10^{-6} mol PbO must be supplied. At the flow rates required for the perovskite phase to be in equilibrium, 10^{-6} mol PbO is supplied to the furnace within 1 minute.

5.2.2 Material Preparation & Characterization

PZT films with Zr:Ti ratios of 52:48 (PZT 52/48, 0.93 μm) and 30:70 (PZT 30/70, 1.19 μm) were deposited by the sol-gel method[156] on 4" Pt/Si wafers (Nova Electronic Materials). Following crystallization, wafers were broken into 1" x 1" pieces and annealed at varying PbO partial pressures in the PbO RTA for 1 hour. Three different flow rates were used: near that for pyrochlore development, near the $PbO_{(g)}$ equilibrium, and halfway between. Photolithography (LOR 5A, Shipley SPR 3012, MABA6) followed by Pt deposition (Kurt Lesker CMS-18) was used to provide top electrode contacts.

X-ray diffraction (XRD) and field emission scanning electron microscopy (FE-SEM) were employed to ensure perovskite phase after anneals. Leakage measurements were collected on all samples up to 20 V in 0.5 V increments (HP 4140A). Capacitance was measured as a function of frequency and *dc* bias with a small field *ac* signal of 10 kHz and 30 mV (HP 4284A Precision LCR). Polarization – electric field hysteresis loops were acquired as a function of maximum drive field (Radiant Multiferroic Tester). Aging data for the permittivity and piezoelectric constant $e_{31,f}$ were collected after poling. The room temperature poling conditions were at 3.5 x E_C (180 kV/cm for PZT 52/48 and 310 kV/cm for PZT 30/70) for 30 min. Hot poling was conducted at 150ºC with a field of 3.5 x E_C for 15 min; the field was maintained while cooling. Poling conditions were determined by monitoring the $d_{33,f}$ piezoelectric coefficient (aixACCT DBLI). Aging in the permittivity was measured under an *ac* excitation of 10 kHz and 30 mV for 2.5 hours. Aging in the piezoelectric coefficient $e_{31,f}$ was measured using the wafer flexure technique[157] over a period of 12 hours.

The local nonlinear response was measured for the PZT 52/48 samples annealed at various PbO pressures in order to characterize the local influence of PbO defects on domain wall motion. Band excitation piezoresponse force microscopy (BE-PFM) measurements[57] were collected (Asylum Cypher, nanoSENSORS PPP-EFM-W) on capacitor structures with the signal applied from the bottom electrode, and with top electrode and tip grounded. The applied signal was chosen to minimize contribution from the tip-surface nonlinearities.[60] The vertical displacement as a function of electric field frequency and amplitude was then fit to a simple harmonic oscillator model.[59] The displacement at tip-surface resonance was used to calculate the *local* nonlinear response, $\alpha_d/d_{33,init}$, for a 125 x 125 grid on an 8 x 8 μm map. Clusters of high and low nonlinear response were determined as regions of more than 4 pixels with response more than ¾ of a standard deviation above (below) the mean nonlinear response.

5.3 Results and Discussion

No evidence for PbO or pyrochlore second phases was found by either XRD (Figure 5.2) or FE-SEM (Figure 5.3) for samples annealed in the perovskite phase field. The XRD peak intensities and peak positions are the same for all PbO contents, indicating that no significant changes in crystallinity or the lattice parameter occurred. Similarly, no changes could be seen in the grain size as a result of the annealing, indicating no coarsening of the grain structure occurred while annealing in a Pb-rich atmosphere.

The dielectric properties of the PZT 52/48 and PZT 30/70 films are shown in Figure 5.4 and Figure 5.5 respectively. Typical remanent polarizations were 31 μC/cm^2 for PZT 52/48 and 39 μC/cm^2 for PZT 30/70. Low field leakage currents of ~ 10^{-10} A/cm^2 were observed for all samples as reported in **Error! Reference source not found.**. This is comparable to other PZT

thin films,[158] indicating similar preparation quality. The low leakage current for the high PbO content films suggests that little PbO is present on the grain boundaries.

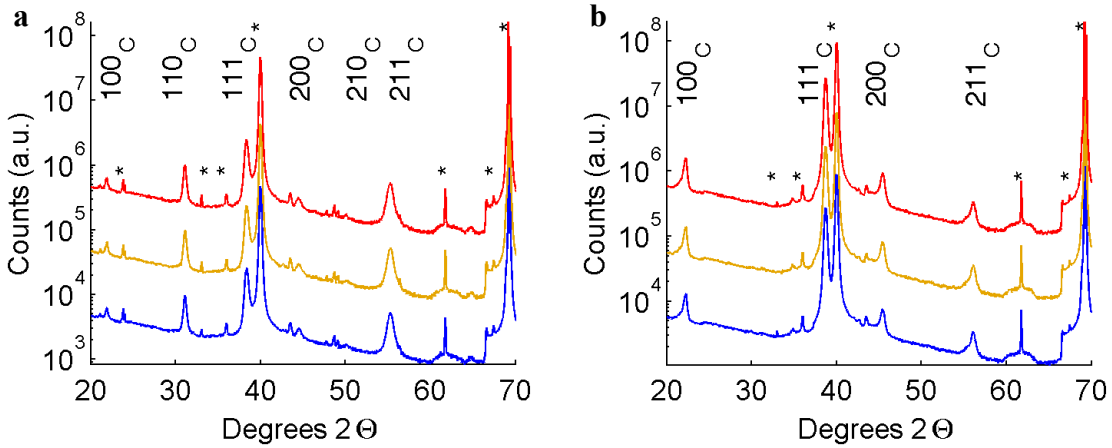

Figure 5.2: XRD on PZT 52/48 and PZT 30/70 with various PbO concentrations.

X-ray diffraction on (a) PZT 52/48 and (b) PZT 30/70 showing phase pure perovskite for (blue) low PbO partial pressure, (yellow) intermediate PbO partial pressure, and (red) high PbO partial pressure. Asterisks denote substrate peaks (including those from wavelengths other than Cu Kα). The subscript C refers to indexing based on the pseudocubic perovskite cell.

Rayleigh measurements were made on all of the samples annealed under different conditions. It was found, as was expected, that the tetragonal films showed significantly lower initial permittivities and lower $\alpha_e/\varepsilon_{init}$ values than MPB films (see Table 5.2). As shown in Figure 5.4, there was no systematic change in the Rayleigh behavior for films annealed at different lead overpressures for PZT 52/48. This suggests that there is no significant variation in the global domain wall pinning with changing PbO content. However, as shown in Figure 5.5, PZT 30/70 shows a decreased dispersion in the reversible Rayleigh component, ε_{init}, for the high PbO content film, suggesting that V_{Pb}'' and/or $V_O^{\cdot\cdot}$ defects may act to slow domain wall motion or slow depinning.

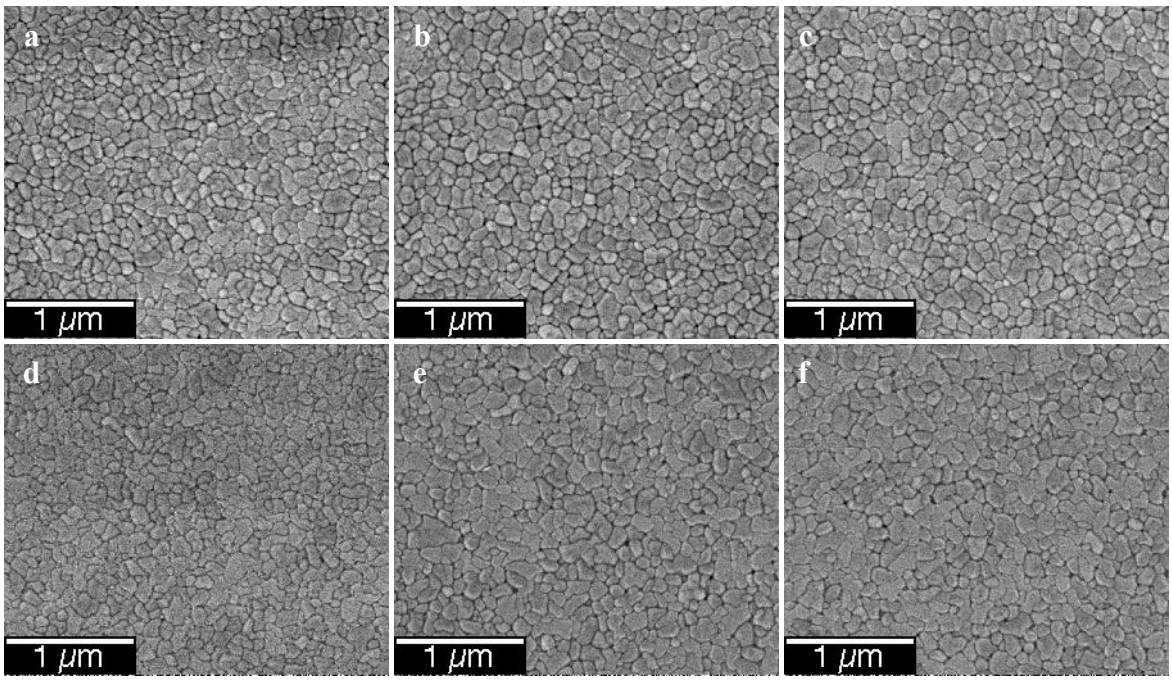

Figure 5.3: FE-SEM for PZT 52/48 and PZT 30/70 with various PbO contents.

Plan-view FE-SEM of (a-c) PZT 52/48 and (d-f) PZT 30/70 annealed at various partial pressures of PbO: (a,d) low, (b,e) intermediate, and (c,f) high. No second phase is visible.

Table 5.1: Leakage for PZT 52/48 and PZT 30/70 with various PbO contents.

Low temperature leakage extrapolated to zero applied field. 52 stands for PZT 52/48, 30 stands for PZT 30/70, and Low, Medium, and High are the flow rates of TEL. Reported values have units of $\log(A/cm^2)$.

	52 Low	52 Medium	52 High	30 Low	30 Medium	30 High
–Log(J)	9.8±0.2	10.0±0.2	9.8±0.1	9.9±0.3	9.9±0.1	10.2±0.2

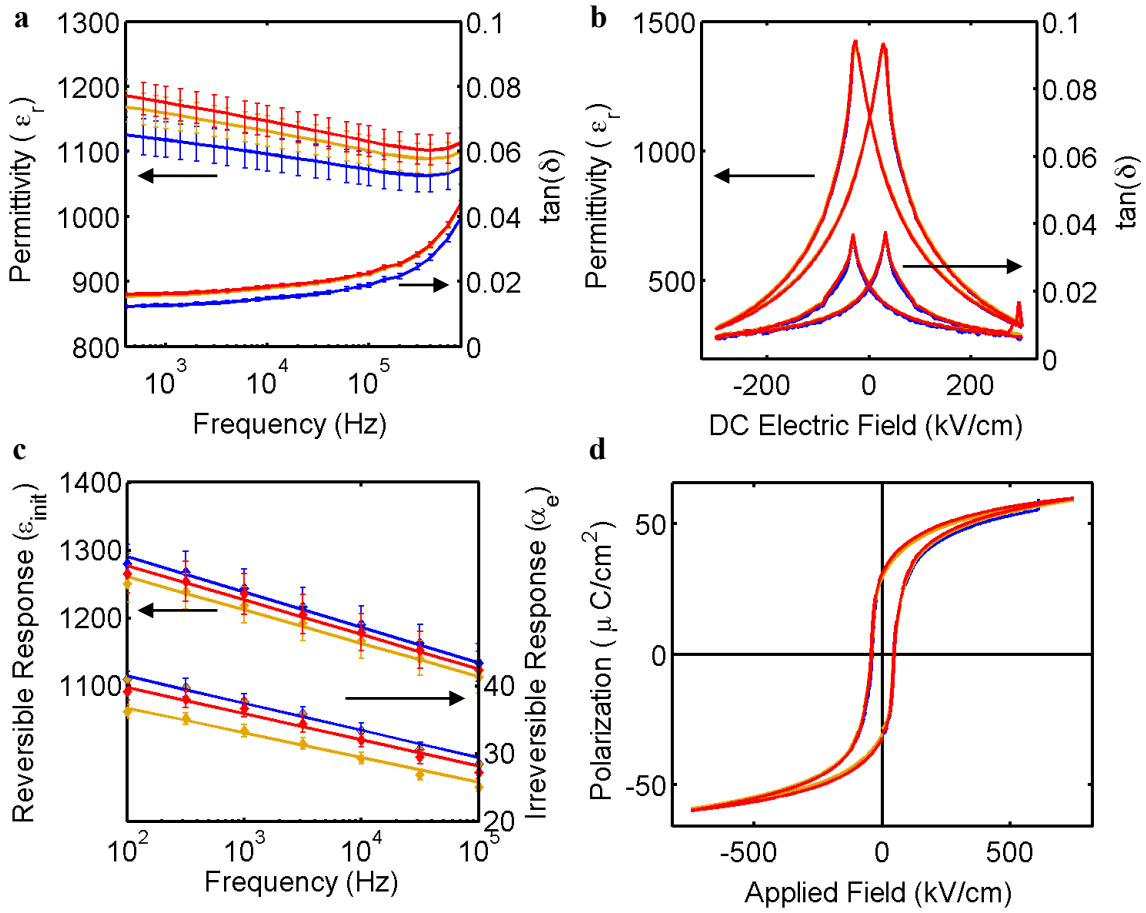

Figure 5.4: Electrical properties of PZT 52/48 with various PbO contents.

(a) ε_r and $\tan(\delta)$ vs. frequency, (b) ε_r and $\tan(\delta)$ vs. electric field, (c) $\varepsilon_{r,init}$ and α_e at various frequencies, and (d) polarization vs. electric field for various PbO partial pressures (blue) low, (yellow) intermediate, and (red) high, all showing comparable electrical properties.

Minor hysteresis loops collected at a maximum field of 50 kV/cm are presented in Figure 5.6 (a,b). The variation in remanent polarization and hysteresis for PZT 52/48 with maximum drive field from 5 kV/cm to 50 kV/cm is reported in Figure 5.6(c,d). The systematic decrease in remanent polarization with increasing PbO content for excitation fields of 25-50 kV/cm indicates that more polarization is reoriented at intermediate fields for the PbO deficient films. The

observed variation in switchable polarization with PbO content is unlikely to be associated with space charge, since the leakage does not vary with the PbO content as the electric field is increased and the major hysteresis loops in Figure 5.4(d) show full saturation with minimal "opening" at the tips at maximum field. In contrast to the observations for PZT 52/48, PZT 30/70 did not show a clear trend in hysteresis or remanent polarization for the PbO concentrations assessed.

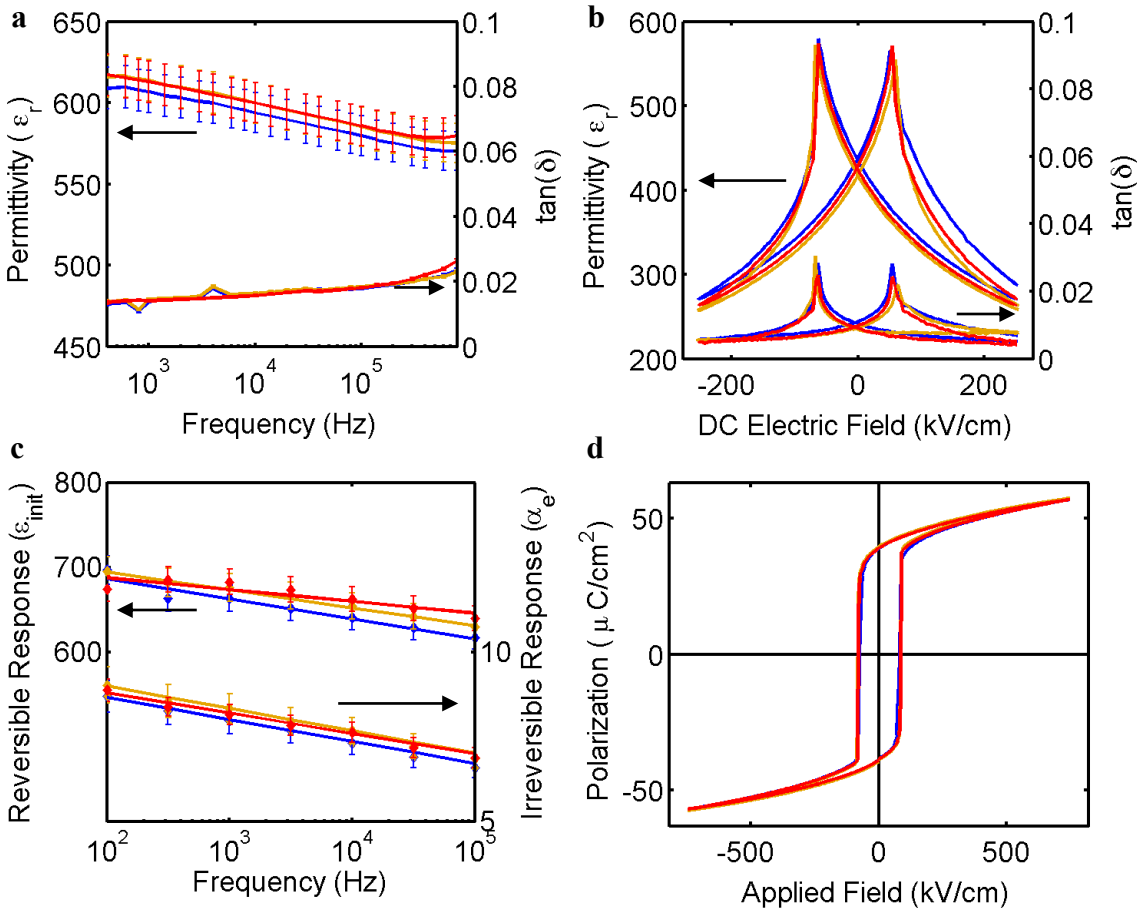

Figure 5.5: Electrical properties of PZT 30/70 with various PbO contents.

(a) ε_r and $\tan(\delta)$ vs. frequency, (b) ε_r and $\tan(\delta)$ vs. electric field, (c) $\varepsilon_{r,init}$ and α_e at various frequencies, and (d) polarization vs. electric field for various PbO partial pressures (blue) low, (yellow) intermediate, and (red) high, all showing comparable electrical properties.

Table 5.2: Dielectric permittivity, loss, and nonlinearity for PZT 52/48 and PZT 30/70 with various PbO concentrations.

Permittivity, loss, and dielectric nonlinearity for films annealed at Low, Medium, and High flow rates of TEL after poling at room temperature. 52 stands for PZT 52/48 and 30 stands for PZT 30/70.

	52 Low	**52 Medium**	**52 High**	**30 Low**	**30 Medium**	**30 High**
ε	1100±30	1130±20	1150±20	590±10	600±10	600±10
tan(δ) (%)	1.48±0.05	1.79±0.04	1.84±0.04	1.56±0.04	1.63±0.04	1.56±0.04
$\alpha_e/\varepsilon_{init}$ (10^{-3} cm/kV)	28±2	25±1	27±1	11.4±0.8	11.7±0.9	11.5±0.7

The variations in maximum polarization at intermediate fields for PZT 52/48 contrast with no variation observed in the Rayleigh parameters measured up to 17 kv/cm. However, the variation in polarization in the minor loops becomes prominent beyond the Rayleigh regime, indicating that the increased contribution to polarization is present at intermediate fields.

One model which can explain the variation in polarization with PbO content is to ascribe an intermediate pinning energy to V_{Pb}'' and/or $V_O^{\cdot\cdot}$ defects. The pinning energy is large enough that electric fields applied during Rayleigh measurements are unable to move domain walls across the pinning sites, but small enough that there is no appreciable variation in the coercive field and remanent polarization in full switching polarization – electric field hysteresis loops. With intermediate energy pinning sites, the defects will pin domain walls in new positions and increase the remanent polarization in minor loops. For the case of PZT 30/70, for which no variation in the polarization was observed with PbO content, the increased ferroelectric distortion

and increased domain size may lead to domain wall – domain wall interactions which dominate the response relative to varying PbO content.

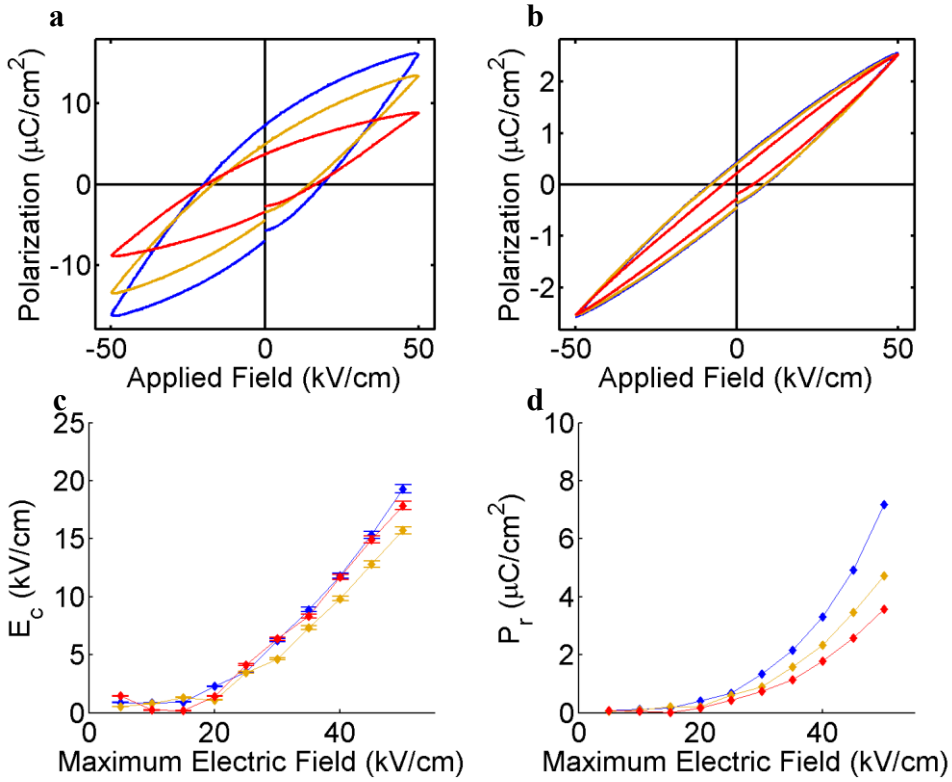

Figure 5.6: Minor polarization - electric field hysteresis loops for PZT 52/48 and PZT 30/70 with various PbO concentrations.

Minor hysteresis loops for (a) PZT 52/48 and (b) PZT 30/70 collected at a maximum electric field of 50 kV/cm. (c) Coercive field (E_c) and (d) remanent polarization (P_r) for PZT 52/48. Colors represent various PbO partial pressures: (blue) low, (yellow) intermediate, and (red) high.

Table 5.3: Piezoelectric constant $e_{31,f}$ for hot and cold poled PZT 52/48 and PZT 30/70.

Piezoelectric constant $e_{31,f}$ for films annealed at Low, Medium, and High flow rates of TEL after poling at room temperature and high temperature. 52 stands for PZT 52/48 and 30 stands for PZT 30/70.

Poling	52 Low	52 Medium	52 High	30 Low	30 Medium	30 High
Cold	–5.8±0.6	–6.4±0.6	–4.6±0.5	–3.0±0.3	–3.2±0.3	–3.6±0.4
Hot	–8.5±0.9	–7.9±0.8	–7.4±0.7	–3.8±0.4	–2.9±0.3	–3.4±0.3

The $e_{31,f}$ values for the various samples are reported in Table 5.3. It was found that $e_{31,f}$ increased by 20% - 60% after hot poling for the PZT 52/48 films compared to room temperature poling. This is consistent with the observation that $e_{31,f}$ is more sensitive to the absolute polarization state than is permittivity. Thus, a 180° polarization reversal would not be expected to affect the permittivity and its aging, but it should significantly affect $e_{31,f}$. Decreasing $e_{31,f}$ is evident with increasing PbO content, suggesting that the low PbO content films could be poled more completely.

One explanation for the observed behavior is that aligned $V''_{Pb} - V^{\cdot\cdot}_{O}$ defect dipoles stabilize the poled domain structure in lead-deficient films. In order to assess this, the $e_{31,f}$ values were remeasured with an applied dc bias parallel to the poling direction. Table 5.4 shows that under bias, the $e_{31,f}$ values for films with different Pb contents vary less than the zero bias measurements. This is presumably because the domain states are more similar under bias. This, in turn, suggests that films with lower lead contents may enable more internal bias after hot poling.

Table 5.4: Piezoelectric constant $e_{31,f}$ for PZT 52/48 measured under bias.

Piezoelectric constant $e_{31,f}$ for PZT 52/48 measured with a bias applied parallel to the poling direction for films annealed at Low, Medium, and High flow rates of TEL after poling at high temperature.

Bias	52 Low	52 Medium	52 High
None	–8.5±0.9	–7.9±0.8	–7.4±0.7
½ E_c	–8.4±0.8	–8.3±0.8	–8.4±0.8
E_c	–8.5±0.9	–8.5±0.9	–8.7±0.9

Measurements of the local nonlinear response for PZT 52/48 made by BE-PFM are presented in Figure 5.7. Clusters of high and low nonlinear response were observed, as has been seen previously.[59] For these measurements, a maximum excitation field of 22 kV/cm was employed to provide sufficient amplitude of response to calculate nonlinearity. Intriguingly, this excitation is at the low end of the range where a variation in remanent polarization is observed, and thus provides unique information on the evolution of the global trend in polarization state from the local domain wall mobility.

A reduced average $\alpha_d/d_{33,init}$ response was observed for the lowest PbO content as can be seen in the histogram in Figure 5.7(d). The size of both high and low response clusters were analyzed; the results are shown in Figure 5.7(e). An increasing size of low response clusters was correlated with decreasing PbO content. This suggests that the modulations in potential energy associated with PbO defects influence the domain wall motion most significantly where domain wall motion is already low. That is, the PbO defects act to augment pinning.

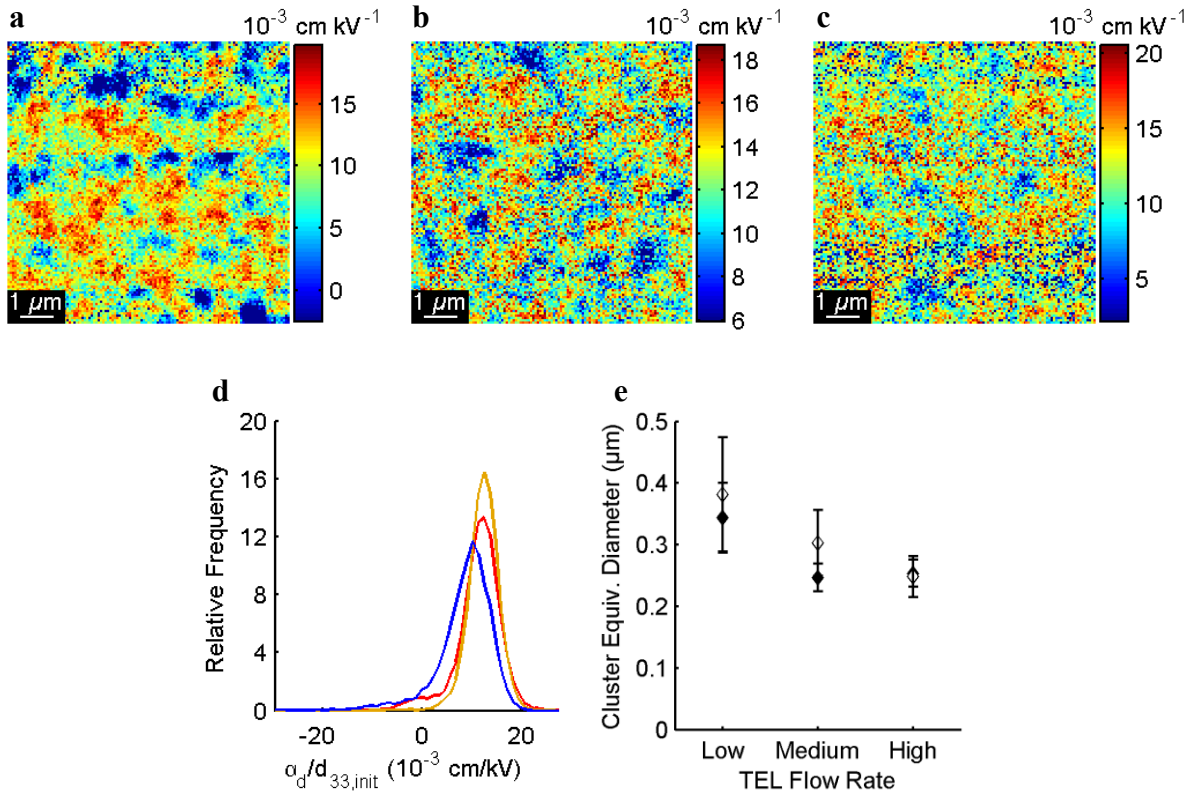

Figure 5.7: Local nonlinear response for PZT 52/48 with various PbO contents.

(a-c) Maps of the local nonlinear piezoelectric response $\alpha_d/d_{33,init}$ for PZT 52/48 at (a) low, (b) medium, and (c) high flow rates of TEL. (d) Distribution of nonlinear response for low (blue), medium (yellow), and high (red) flow rates of TEL. (e) Mean equivalent diameter of high (filled) and low (empty) response clustering in the local nonlinear response.

Aging data for the permittivity are presented in Figure 5.8(a,d). In both cases, the "zero" time was the time at which the electric field was removed. Minimal variation in the permittivity aging rate was observed between samples of the same composition regardless of poling conditions. The variation shown for PZT 30/70 permittivity aging is within the error for multiple measurements. Minimal change in the aging rates between low and high temperature poling

indicates that V_{Pb}'' and/or $V_O^{\cdot\cdot}$ defects, or defect dipoles as previously reported to exist in the PZT system,[159]–[161] do not dominate aging of permittivity in these films.

Aging data for $e_{31,f}$ after room temperature and after hot poling are presented in Figure 5.8(b,e). For both PZT film compositions, the aging rate decreased significantly upon high temperature poling. In addition, the aging rate after hot poling decreases with increasing lead content for both compositions. That is, for PZT 52/48 the piezoelectric constant is highest for the lowest lead content, it also has the highest aging rate, indicating that the internal bias decays significantly at room temperature. This cannot be explained by stationary defect dipoles present in films with low PbO content, since the aging rate would be lowest for samples with the highest defect concentration. However, if the defects are mobile at room temperature, the trend in aging rates is consistent with defects returning to lower energy positions, with a commensurate reduction in the aligned remanent polarization.

If mobile defects are present, it is expected that they have a different time constant and energy required for motion when compared to domain walls. As such, high temperature poling significantly increases the imprint and piezoelectric $e_{31,f}$ constant because both domain wall motion and defect motion contribute to maximize the net polarization. Additionally, the local variation in the elastic and electric energies at the defects can pin domain walls. As domain wall motion is driven by gradients in the electric field and strain, the defect motion will be driven by gradients in the electric field, strain, and chemical potential. Aging in the piezoelectric $e_{31,f}$ constant may thus be a result of the defects responding to a chemical potential and, as they move to an equilibrium position, changing the alignment of the polarization.

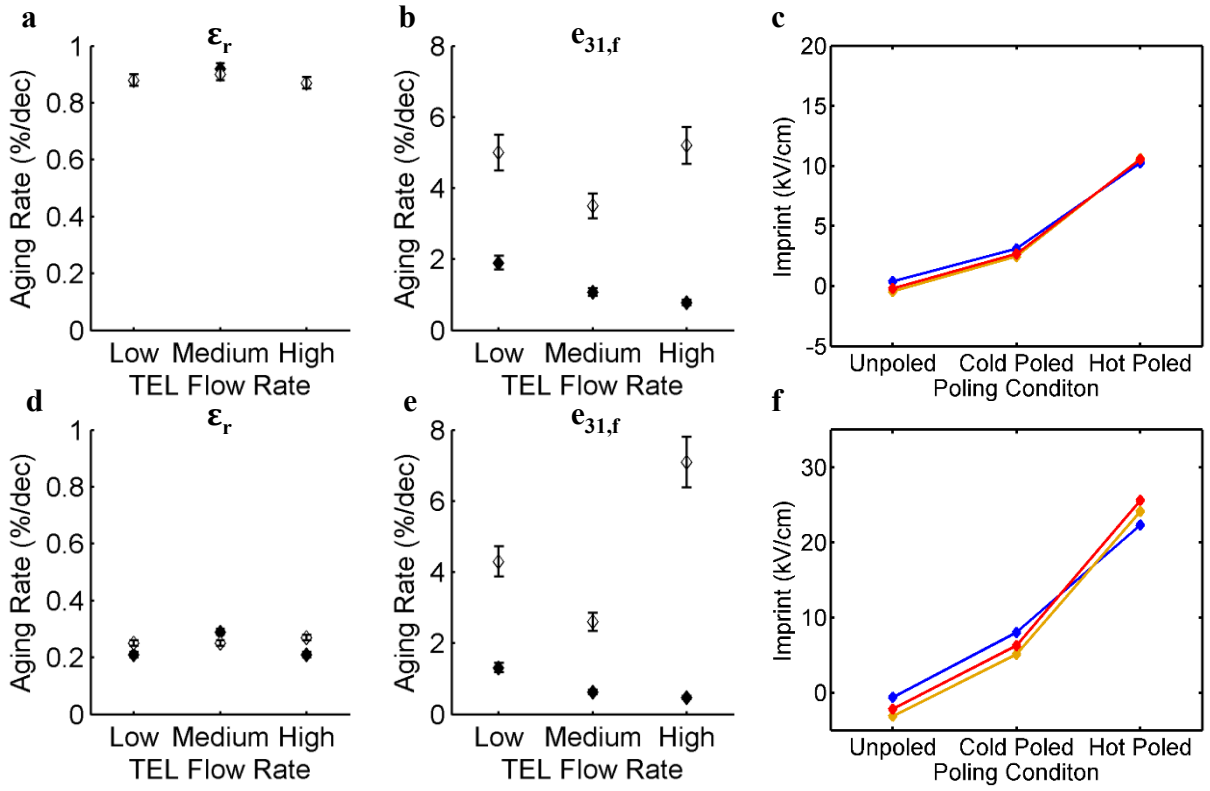

Figure 5.8: Aging in permittivity and imprint for PZT 52/48 and PZT 30/70 after hot and cold poling.

Aging rate of (a,d) permittivity and (b,e) $e_{31,f}$ for cold poled (empty) and hot poled (filled) (a,b) PZT 52/48 and (d,e) PZT 30/70. (c,f) Amount of imprint for (c) PZT 52/48 and (f) PZT 30/70 with low (blue), medium (yellow), and high (red) flow rates of TEL.

The imprint after room temperature and high temperature poling reported in Figure 5.8(c,f) was assessed from hysteresis loops collected at 200 kV/cm. All samples exhibited imprint after room temperature poling; the internal field increased significantly upon high temperature poling. The presence of imprint generally results in an improved poling of the ferroelectric with increased piezoelectric response and reduced permittivity in the direction of the dipoles and a decreased aging rate. Imprint may be caused by any factor that gives rise to an

internal field, including defect dipoles,[162] space charge, and charge injection.[61] The decreased $e_{31,f}$ aging rates after hot poling compared to room temperature poling indicate that $V_{Pb}'' - V_O^{\cdot\cdot}$ defect dipoles may cause the observed imprint character, rather than charge injected during poling.

5.4 Conclusions

A furnace was developed to permit thermodynamic control of lead partial pressure during high temperature processing of PZT thin films. Films annealed in the perovskite phase field show a high dielectric constant, low loss, saturated hysteresis loops, and high tunability. Measurements of the local nonlinear response indicate that PbO defects pin domain walls but only in regions where the nonlinear response is already low. Control of the PbO defect concentration is an additional parameter that may be used to enhance device performance. For these films, $V_{Pb}'' - V_O^{\cdot\cdot}$ defect dipoles made minor contributions to the polarization state after high temperature poling. The results suggest that PbO control during fabrication is primarily useful for preventing the formation of parasitic second phases.

Chapter 6: Conclusions and Future Work

6.1 Conclusions

6.1.1 Influence of a Single Grain Boundary on Domain Wall Motion in Ferroelectrics

Measurements of the local nonlinear response near a single 24° tilt grain boundary in PZT 45/55 indicated reduced domain wall motion for a span of 720-820 nm across the grain boundary. A maximum in the nonlinear response was observed adjacent to the region of reduced domain wall motion. Comparison with TEM measurements indicated that the region of reduced nonlinear response correlated to regions with polarization oriented parallel to the grain boundary, while the increased domain wall motion correlated to the boundary of regions with polarization oriented perpendicular to the grain boundary. It was determined that the change in domain structure near the grain boundary resulted in significant pinning of domain wall motion. Although measurements were made on a symmetric grain boundary, these results suggest that large angle asymmetric tilt grain boundaries in polycrystalline films and ceramics would influence the local domain structure (and hence the domain wall mobility), explaining the reduced nonlinear response observed in samples with sub-micron grain size.

6.1.2 Domain Pinning Near a Single Grain Boundary in Tetragonal and Rhombohedral Lead Zirconate Titanate Films

A reduced width of influence from domain wall motion near a 24° tilt grain boundary was observed for PZT 52/48 compared to PZT 45/55 and was attributed to the higher domain wall density near the morphotropic phase boundary accommodating the local strain and electric field. A more complex nonlinear response was observed near a 24° tilt grain boundary in PZT

20/80 with alternating low and high nonlinear response with distance from the grain boundary. The response observed near the PZT 20/80 grain boundary was correlated to the average domain structure imaged by TEM. Domain wall pinning was associated with the local elastic and electric fields at the grain boundary, shown by phase field models, and the correlated domain structures, observed by TEM and PFM. Measurements indicate a correlation between observed nonlinear response and domain wall – domain wall interactions. These results can be used as a starting point to model domain wall motion and the evolution of nonlinear response in polycrystalline ferroelectrics.

6.1.3 Domain Wall Motion Across Various Grain Boundaries in Ferroelectric Thin Films

Measurements of domain wall motion were conducted across a variety of tilt and twist grain boundaries for PZT 45/55 and PZT 52/48. The highest angle tilt grain boundaries had a larger width of reduced nonlinear response compared to twist grain boundaries, while the smallest angle tilt grain boundaries had a maximum in nonlinear response at the grain boundary. The reduction in domain wall motion for the highest angle tilt and twist grain boundaries was attributed to an increase in domain wall density to accommodate the local strain and electric field. It is hypothesized that the variation in width of reduced nonlinear response for tilt and twist grain boundaries is due to different distances required for the local strain energy to decay. It was determined that the pinning energy varied with the grain boundary angle, such that the small pinning energy for the smallest angle tilt grain boundary resulted in an increase in the local nonlinear response such that moderate electric fields will irreversibly move domain walls across the grain boundary.

6.1.4 A-site Stoichiometry and Clustered Domain Wall Motion in Thin Film $PbZr_{1-x}Ti_xO_3$

Annealing PZT 52/48 and PZT 30/70 films in the presence of a controlled PbO atmosphere permitted variation in the PbO concentration. The PbO concentration was found to have minimal effect on the functional properties measured, including the permittivity, the polarization – electric field hysteresis, the Rayleigh coefficients, and the aging rates. Measurements of the local nonlinear response indicate that PbO deficiencies increase the cluster size of low nonlinear response, thus decreasing domain wall motion near to where it is already reduced. These results suggest that the $V_{Pb}'' - V_O^{\cdot\cdot}$ defect dipole, if it exists, does not act as a strong pinning site relative to other defects in the film.

6.2 Future Work

6.2.1 Domain Structure Dependence of Nonlinear Response

Previous work has indicated that the nonlinear response is dependent on the interactions between domain walls.[2], [40], [113] Therefore, it is interesting to consider how the clustering in local nonlinear response and the global nonlinear response varies as the concentration of non-180° domain walls is changed.

The domain structure in $Pb(Zr,Ti)O_3$ (PZT) is dependent on the strain as it cools through the Curie temperature. One method of engineering the strain state in relaxed films is by controlling the thermal expansion mismatch between the film and the substrate which develops upon cooling from the growth temperature to the Curie temperature following Equation 6.1.[163]

$$\varepsilon_{thermal} = \left(\alpha_{sub} - \alpha_{film}\right) \times (T_d - T_C) \qquad \text{Equation 6.1}$$

For Equation 6.1, α_{sub} and α_{film} are the thermal expansion coefficients of the substrate and film, respectively, and T_d and T_C are the deposition and Curie temperature, respectively.

A range of substrates is commercially available with various thermal expansion coefficients. Substrates were chosen with the widest available range of thermal expansion coefficients of 2.6 ppm/°C for $SrTiO_3$//Si[164] and 18.9 ppm/°C for CaF_2[165] along with an intermediate value of 11.2 ppm/°C for $SrTiO_3$.[166] Epitaxial PZT films grown on $SrTiO_3$//Si should be in tensile stress from the lower substrate thermal expansion relative to the film; this will lead to the polar axis being predominantly oriented in the plane of the film (*a*-axis oriented). Conversely, films grown on CaF_2 will be put into compressive stress due to a higher thermal expansion than the film, resulting in the polar axis predominantly oriented perpendicular to the surface of the film (*c*-axis oriented). Films grown on $SrTiO_3$ will have much lower stresses and will have a combination of *a*-axis and *c*-axis orientations.

Using the same deposition parameters from previous reports[2] resulted in poorly oriented PZT films on CaF_2 with the presence of {110} and {111} oriented crystallites (see Figure 6.1(a,b)). The deposition parameters reported in Table 6.1 were found to provide epitaxial, {001} oriented films, with x-ray diffraction θ-2θ scans and scanning electron micrographs in Figure 6.1(c,d). The deposition conditions reported in Table 6.1 were used to deposit PZT 45/55 and PZT 52/48 on $SrRuO_3$ buffered CaF_2, $SrTiO_3$, and $SrTiO_3$//Si. All films had 100/001 out of plane as measured by x-ray diffraction θ-2θ and were epitaxial according to φ scans on the PZT 110 peaks. X-ray diffraction θ-2θ scans shown in Figure 6.2 indicate that the films grown on CaF_2 are predominantly *c*-oriented and films grown on $SrTiO_3$//Si are predominantly *a*-oriented with maximum 002/200 peak position reported in Table 6.2.

Table 6.1: $SrRuO_3$ and PZT deposition parameters.

Deposition parameters for PZT 45/55 and PZT 52/48 for growth on CaF_2.

Composition	Pressure (mTorr)	Temperature (°C)	Substrate Distance (cm)	Laser Energy (J/cm^2)	Repetition Rate (Hz)	# Pulses
$SrRuO_3$	160	680	8	1.1	10	600
$Pb(Zr,Ti)O_3$	100	650	5	1.2	10	600

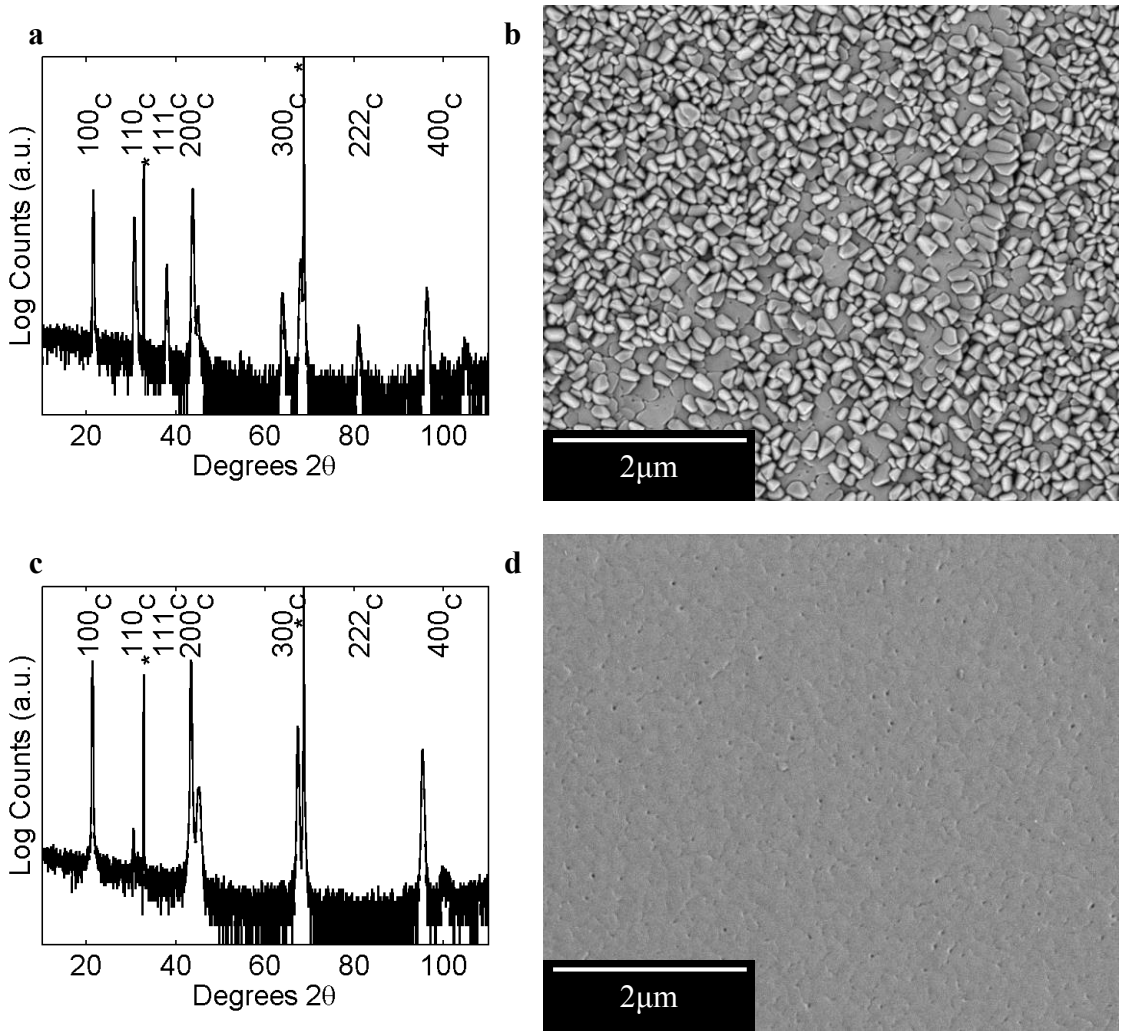

Figure 6.1: Quality of film growth on CaF_2.

(a,c) X-ray diffraction and (b,d) SEM of PZT 45/55 on CaF_2 deposited under (a,b) old and (c,d) new conditions. For x-ray diffraction plots, peak indices are reported for the cubic PZT peak positions and substrate peaks are marked with *.

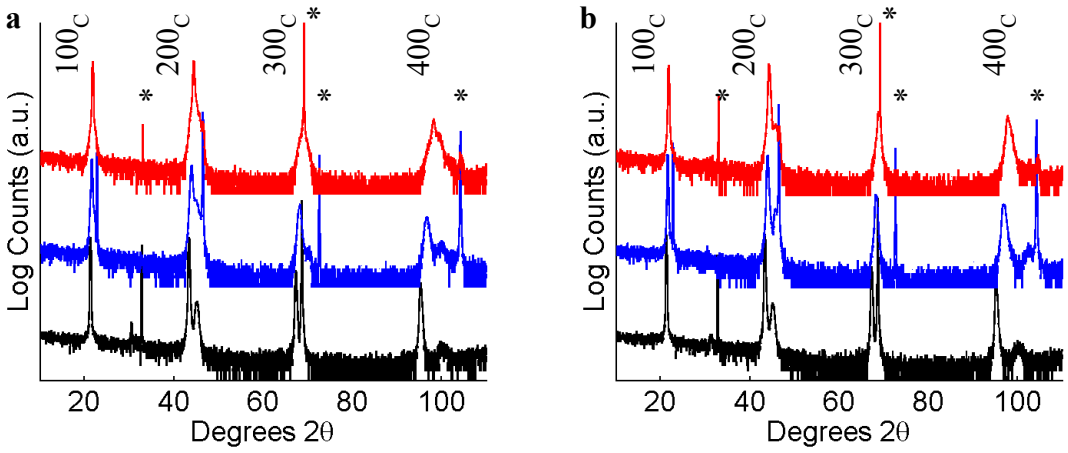

Figure 6.2: X-ray diffraction of strained PZT films.

θ-2*θ* x-ray diffraction scans of (a) PZT 45/55 and (b) PZT 52/48 on CaF_2 (black), $SrTiO_3$ (blue), and $SrTiO_3$//Si (red).

Table 6.2: XRD and electrical properties of strained PZT films.

Relative integrated intensities for 002 and 200 peaks of PZT 45/55 and PZT 52/48 grown on CaF_2, $SrTiO_3$, and $SrTiO_3$//Si.

Measurement	PZT 45/55			PZT 52/48		
	CaF_2	$SrTiO_3$	$SrTiO_3$//Si	CaF_2	$SrTiO_3$	$SrTiO_3$//Si
Peak Position (2θ)	43.37°	43.95°	44.45°	43.33°	43.95°	44.27°
Thickness (nm)	587	560	683	730	708	594
ε_r	180	467	716	174	450	883
tan(δ)	0.04	0.04	0.03	0.04	0.04	0.04
P_r (μC/cm^2)	65.6	30.0	25.6	65.0	49.0	44.8
ε_{init}	140±1	384±4	637±6	149±2	363±4	597±6
α_e (10^{-3} cm/kV)	498±7	1564±51	3675±39	643±10	4380±52	7267±81

Global electrical measurements (see Table 6.2) also indicated *c*-orientation for films on CaF_2, *a*-orientation for films on $SrTiO_3$, and a combination for films on $SrTiO_3$//Si. Films on CaF_2 exhibited an increased remanent polarization and decreased permittivity, while films on

$SrTiO_3$//Si exhibited a decreased remanent polarization and increased permittivity, all indicating that films on CaF_2 are predominantly *c*-oriented and films on $SrTiO_3$//Si are predominantly *a*-oriented. Additionally, films on CaF_2 exhibited a decreased Rayleigh regime with decreased nonlinear contribution relative to films on $SrTiO_3$, indicating that domain wall motion is significantly reduced as the film approaches a single polarization state.

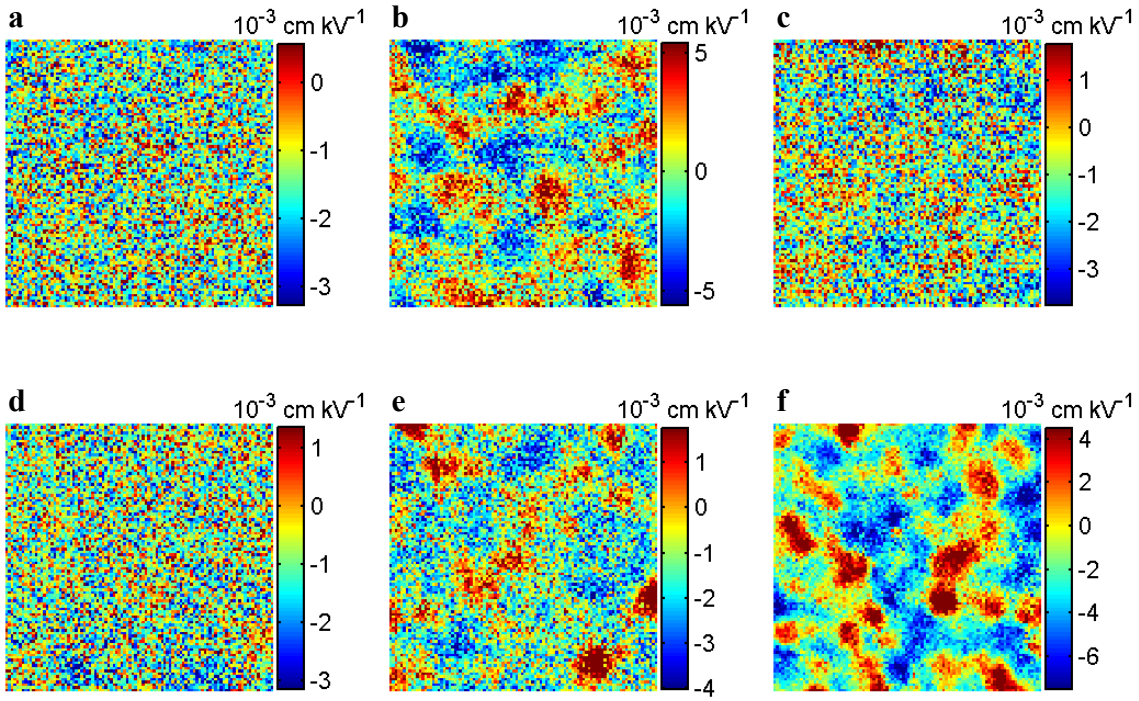

Figure 6.3: Local nonlinear response for strained PZT films.

Maps of local nonlinear response $\alpha_d/d_{33,init}$ for (a-c) PZT 45/55 and (d-f) PZT 52/48 on (a,d) CaF_2, (b,e) $SrTiO_3$, and (c,f) $SrTiO_3$//Si.

Measurements of the *local* nonlinear response were conducted using band excitation piezoresponse force microscopy (BE-PFM). Plots of measurements collected on 5 μm x 5 μm for all six samples are provided in Figure 6.3. It is evident that the PZT 45/55 film on $SrTiO_3$ exhibits clustering of the nonlinear response, while clustering is not as easily evident in the other

two PZT 45/55 films. Full statistical analysis must be conducted to determine whether significant clustering is present.

However, in the PZT 52/48 films, no clustering is evident for the film on CaF_2, but the intensity of the clustering increases as the strain becomes more tensile, with the largest range between low and high response evident for the film on $SrTiO_3$//Si. The PZT 52/48 films are near the morphotropic phase boundary, meaning that small changes in strain can shift the phase from tetragonal to rhombohedral.[165] PZT 52/48 films deposited on $SrTiO_3$ were previously shown to be rhombohedral,[113] but deposition on CaF_2 may result in sufficient strain to make the film tetragonal with few non-180° domain walls, resulting in reduced clustering in the *local* nonlinear response. Films deposited on $SrTiO_3$, however, have active domain walls which produce clustering in the nonlinear response. Under tensile strain on $SrTiO_3$//Si, the films may have active non-180° domain walls, resulting in evident clustering in the nonlinear response. The increased range of nonlinear response may be due to the higher maximum excitation field permitted by the extended Rayleigh regime observed in the dielectric nonlinear response.

Other authors have shown that the morphotropic phase boundary can shift with strain.[165] In order to assess the phase present for PZT 52/48 under the different thermal strains, high resolution XRD must be conducted. Primarily, this will provide information of what types of domain walls may be active in the various strain states. In addition, statistical analysis must be completed to determine whether cascaded movement of domain walls is different for the different strain states.

The domain structure of the films must also be characterized. PFM on the bare surface of the film will provide information about the concentration of in-plane versus out-of-plane domains, the average domain size, and whether domain wall interactions are likely controlling

the local nonlinear properties observed. In addition, the frequency dispersion of dielectric Rayleigh response will be collected to see if the different strain states, and resulting domain structures, contribute to a time-dependence of domain wall pinning.

6.2.2 Domain Wall Motion Near Grain Boundaries in Large-Grained Ferroelectrics

Previous measurements indicate that domain wall motion is significantly reduced near symmetric large angle grain boundaries. However, the influence of asymmetric grain boundaries on domain wall motion is unknown. Will domain wall motion be reduced symmetrically around the grain boundary when the crystal lattice orientation is asymmetrically rotated from the grain boundary? Does the ratio of tilt and twist components in the grain boundary significantly influence domain wall motion?

Measurements should be conducted both in pure tilt systems and in systems with a component of both twist and tilt. Samples composed of pure tilt grain boundaries could be deposited with the assistance of an orienting layer of $LaNiO_3$, while polycrystalline films could be utilized for both tilt and twist components of grain boundaries. Attempts should be made to reduce the nucleation density so that large-grained (~500-1000 nm diameter) films can be fabricated. Large grains are necessary so that clustering in the local nonlinear response in individual grains can be resolved.

6.2.3 Breakdown Characteristics of PZT Films with Controlled PbO Defect Concentrations

Measurements of the nonlinear response and aging rates of PZT films annealed under controlled PbO atmosphere indicated weak dependence on the PbO concentration. Many models

for breakdown in PZT attribute the primary event to $V_O^{\cdot\cdot}$ migration and accumulation at the cathode,[167] and some attribute a contribution from V_{Pb}'' to breakdown.[168] If V_{Pb}'' are to play a role in breakdown, it is essential that failure is measured by highly accelerated life-time testing.

6.2.4 Analysis of the Distribution of Local Nonlinear Response

Clustering in the local nonlinear response has previously focused on masking the regions of high and low response to determine equivalent cluster diameters. However, this method ignores the complex structure and interconnectivity that may occur between clusters. In order to create a more complete picture of how the local nonlinear response is distributed, it is necessary to utilize a more advanced analysis technique.

For example, autocorrelation is a technique commonly used in signal processing to determine how well various data points are correlated in time. A similar analysis has already been applied to PFM images collected from relaxor ferroelectric materials to determine domain size.[169] This technique has not yet been applied to analyzing the local nonlinear response, but its use would improve analysis of correlated domain wall motion. Autocorrelation will primarily provide superior information on the distribution of cluster sizes in ferroelectric materials.

However, it is evident from the maps of nonlinear response that it is important to consider a range of amplitudes of nonlinear response, as the regions of high nonlinear response are generally connected by tendrils of higher than average nonlinear response, indicating some coupling of domain wall motion between clusters. In order to better understand how domain wall motion is correlated between clusters, it is necessary to better analyze the spatial distribution of nonlinear response. Collaboration with experts in statistics and data analysis may provide insight for possible analysis techniques.

Appendix A: MATLAB Code for Calculating Nonlinearity Maps

```
% % Modified to quadratic / linear normalized by thickness (cm/kV).
% % multiply m1, m2, max_out, bin_size by 2 to get back to a/d33

close all
clear all
clc

file_path = 'C:\Users\Daniel\Desktop\CNMS\2014.01\Data\PZT52_19';
file_name = 'nl_0001';
fit_suffix = 'nlinfit ri SHO parms';

% load([ file_path '\' file_name ])
load([ file_path '\' file_name '\' file_name ' ' fit_suffix ])

% % To use data from fast SHO fit, change SHO_fit above to fast_SHO_fit and
% % uncomment following line.

coef_mat4 = squeeze(cat(5, A, w.*(10^-3), q, p.*(pi/180)));
coef_mat4(isinf(coef_mat4)) = NaN;

% coef_mat4 = coef_mat4(6:end,:,:,:);

dc_amp_vec_full = V;

% % size_x and size_y are the dimensions of the measured region. These are
% % used to set the dimensions of the spatial plots.

size_x = 5;
size_y = 5;

% coef_mat4 = coef_mat4(1:60,:,:,:);
% size_y = 3;

% % min_ind is the index of the starting voltage for fit, n_std is the
% % number of standard deviations the colorbar shows in plots, max_out is
% % the maximum a/d33 before start removing data, bin_size is the size of
% % bins for a/d33 histogram

min_ind = 3;
n_std = 2;
max_out = 0.05;
bin_size = 0.0005;

% % First part here is to remove noise at low voltage steps.
```

```
Oldsize = size(coef_mat4,3)/2;
Newsize = Oldsize - min_ind +1;
coef_mat4_01(:,:,1:Newsize,:) = coef_mat4(:,:,min_ind:Oldsize,:);
coef_mat4_01(:,:,Newsize+1:2*Newsize,:) =
coef_mat4(:,:,Oldsize+min_ind:2*Oldsize,:);

dc_amp_vec_full_01(1:Newsize) = dc_amp_vec_full(min_ind:Oldsize);
dc_amp_vec_full_01(Newsize+1:2*Newsize) =
dc_amp_vec_full(Oldsize+min_ind:2*Oldsize);

coef_mat4 = coef_mat4_01;
dc_amp_vec_full = dc_amp_vec_full_01;


% % Plot spatial map of mean resonance frequency with respect to voltage

[num_rows,num_cols,num_steps,num_coefs] = size(coef_mat4);

res_mat3 = coef_mat4 (:,:,:,2);

mean_res_1 = nanmean(res_mat3(:,:,1:num_steps/2),3);
mean_res_2 = nanmean(res_mat3(:,:,num_steps/2+1:end),3);
std_res_1 = nanstd(res_mat3(:,:,1:num_steps/2),0,3);
std_res_2 = nanstd(res_mat3(:,:,num_steps/2+1:end),0,3);

mean_res = reshape([mean_res_1 mean_res_2],2*num_rows*num_cols,1);
m_mean_res = nanmean(mean_res);
std_mean_res = nanstd(mean_res,1);

std_res = reshape([std_res_1 std_res_2],2*num_rows*num_cols,1);
m_std_res = nanmean(std_res);
std_std_res = nanstd(std_res,1);

fh1 = figure(1);
set(fh1, 'color','white');
clf

subplot(3,2,1)
imagesc([0 size_x],[0 size_y],mean_res_1)
colorbar
% set(colorbar,'fontsize',20);
title('Resonance Map Chirp Up in kHz');
caxis([m_mean_res-n_std*std_mean_res m_mean_res+n_std*std_mean_res])
axis image

subplot(3,2,2)
imagesc([0 size_x],[0 size_y],mean_res_2)
colorbar
% set(colorbar,'fontsize',20);
title('Resonance Map Chirp Down in kHz');
caxis([m_mean_res-n_std*std_mean_res m_mean_res+n_std*std_mean_res])
axis image
```

```
% % Plot spatial map of mean quality factor with respect to voltage

q_mat3 = coef_mat4 (:,:,:,3);

mean_q_1 = nanmean(q_mat3(:,:,1:num_steps/2),3);
mean_q_2 = nanmean(q_mat3(:,:,num_steps/2+1:end),3);
std_q_1 = nanstd(q_mat3(:,:,1:num_steps/2),0,3);
std_q_2 = nanstd(q_mat3(:,:,num_steps/2+1:end),0,3);

mean_q = reshape([mean_q_1 mean_q_2],2*num_rows*num_cols,1);
m_mean_q = nanmean(mean_q);
std_mean_q = nanstd(mean_q,1);

subplot(3,2,3)
imagesc([0 size_x],[0 size_y],mean_q_1)
colorbar
% set(colorbar,'fontsize',20);
title('Quality Factor Chirp Up');
caxis([m_mean_q-n_std*std_mean_q m_mean_q+n_std*std_mean_q])
axis image

subplot(3,2,4)
imagesc([0 size_x],[0 size_y],mean_q_2)
colorbar
% set(colorbar,'fontsize',20);
title('Quality Factor Chirp Down');
caxis([m_mean_q-n_std*std_mean_q m_mean_q+n_std*std_mean_q])
axis image

% % Plot spatial map of mean phase with respect to voltage

phase_mat3 = coef_mat4 (:,:,:,4);

mean_phase_1 = nanmean(phase_mat3(:,:,1:num_steps/2),3);
mean_phase_2 = nanmean(phase_mat3(:,:,num_steps/2+1:end),3);
std_phase_1 = nanstd(phase_mat3(:,:,1:num_steps/2),0,3);
std_phase_2 = nanstd(phase_mat3(:,:,num_steps/2+1:end),0,3);

% % Flatten the phase map to reduce influence from changes in tip; this is
% % generally not plotted or used in further calculations

x = 0 : size_x / (num_cols - 1) : size_x;
flat_phase_1 = zeros(size(mean_phase_1));
flat_phase_2 = zeros(size(mean_phase_2));
for k = 1 : num_rows

    y_1 = mean_phase_1(k,:);
    y_2 = mean_phase_2(k,:);

    p_1 = polyfit(x,y_1,1);
    p_2 = polyfit(x,y_2,1);
    p_fit_1 = x*p_1(1) + p_1(2);
    p_fit_2 = x*p_2(1) + p_2(2);
```

```
    flat_phase_1(k,:) = y_1-p_fit_1;
    flat_phase_2(k,:) = y_2-p_fit_2;
end

mean_phase = reshape([mean_phase_1 mean_phase_2],2*num_rows*num_cols,1);
m_mean_phase = nanmean(mean_phase);
std_mean_phase = nanstd(mean_phase,1);

flat_phase = reshape([flat_phase_1 flat_phase_2],2*num_rows*num_cols,1);
m_flat_phase = nanmean(flat_phase);
std_flat_phase = nanstd(flat_phase,1);

subplot(3,2,5)
imagesc([0 size_x],[0 size_y],mean_phase_1)
colorbar
% set(colorbar,'fontsize',20);
title('Phase Chirp Up');
caxis([m_mean_phase-n_std*std_mean_phase m_mean_phase+n_std*std_mean_phase])
axis image

subplot(3,2,6)
imagesc([0 size_x],[0 size_y],mean_phase_2)
colorbar
% set(colorbar,'fontsize',20);
title('Phase Chirp Down');
caxis([m_mean_phase-n_std*std_mean_phase m_mean_phase+n_std*std_mean_phase])
axis image

% % Now fit amplitude to quadratic equation and extract coefficients

amp_mat3 = coef_mat4(:,:,:,1);

include_vec = 1 : num_steps/2;
p_1 = zeros(num_rows,num_cols,3);
p_2 = zeros(num_rows,num_cols,3);

amp_fit_mat3 = zeros(num_rows,num_cols);

for k1 = 1 : num_rows
    disp(k1)
    for k2 = 1 : num_cols

        amp_vec_1 = squeeze(amp_mat3(k1,k2,1:num_steps/2));
        amp_vec_2 = squeeze(amp_mat3(k1,k2,num_steps/2+1:end));

        Vac_1 = dc_amp_vec_full(1:num_steps/2);
        Vac_2 = dc_amp_vec_full(num_steps/2+1:end);

        if sum(~isnan(amp_vec_1(include_vec))) < 3
            p_1(k1,k2,:) = NaN;
            amp_fit_mat3(k1,k2,1:num_steps/2) = NaN;
        else
```

```
            p_1(k1,k2,:) =
polyfit(Vac_1(~isnan(amp_vec_1(include_vec))),amp_vec_1(~isnan(amp_vec_1(incl
ude_vec)))',2);
            amp_fit_1 = p_1(k1,k2,1)*Vac_1.^2 + p_1(k1,k2,2)*Vac_1 +
p_1(k1,k2,3);
            amp_fit_mat3(k1,k2,1:num_steps/2) = amp_fit_1;
        end

        if sum(~isnan(amp_vec_2(include_vec))) < 3
            p_2(k1,k2,:) = NaN;
            amp_fit_mat3(k1,k2,(num_steps/2) + 1:num_steps) = NaN;
        else
            p_2(k1,k2,:) =
polyfit(Vac_2(~isnan(amp_vec_2(include_vec))),amp_vec_2(~isnan(amp_vec_2(incl
ude_vec)))',2);
            amp_fit_2 = p_2(k1,k2,1)*Vac_2.^2 + p_2(k1,k2,2)*Vac_2 +
p_2(k1,k2,3);
            amp_fit_mat3(k1,k2,(num_steps/2) + 1:num_steps) = amp_fit_2;
        end

    end
end

% % Plot the quadratic, linear, and offset

fh2 = figure(2);
clf
set(fh2, 'color','white');
title_cell = { 'Quadratic' ; 'Linear' ; 'Offset' };
p_3 = zeros(2*num_rows*num_cols,3);

for k1 = 1 : 3

    p_3(:,k1) = reshape([p_1(:,:,k1) p_2(:,:,k1)],2*num_rows*num_cols,1);

    p_mean3 = nanmean(p_3(:,k1));
    p_std3 = nanstd(p_3(:,k1),1);

    subplot(3,2,k1*2-1)
    imagesc([0 size_x],[0 size_y],p_1(:,:,k1))
    colorbar
    axis image
    title([ title_cell{k1} ' Chirp Up' ])
    caxis([p_mean3-n_std.*p_std3 p_mean3+n_std.*p_std3]);

    subplot(3,2,k1*2)
    imagesc([0 size_x],[0 size_y],p_2(:,:,k1))
    colorbar
    axis image
    title([ title_cell{k1} ' Chirp Down' ])
    caxis([p_mean3-n_std.*p_std3 p_mean3+n_std.*p_std3]);

end

% % Determine and plot alpha / d33
```

```
thickness = input(['What is the thickness (' texlabel('mu') 'm)?']);


m1 = p_1(2:end,:,1)./p_1(2:end,:,2)/10*thickness;
m_mean1_full = nanmean(nanmean(m1));
threshold1 = find(abs(m1)>max_out);
m1(threshold1) = NaN;
m_mean1 = nanmean(nanmean(m1));

m2 = p_2(2:end,:,1)./p_2(2:end,:,2)/10*thickness;
% m2(isnan(m2)) = nanmean(nanmean(m2));
m_mean2_full = nanmean(nanmean(m2));
threshold2 = find(abs(m2)>max_out);
m2(threshold2) = NaN;
m_mean2 = nanmean(nanmean(m2));

m3 = reshape([m1 m2],numel([m1 m2]),1);
m_mean3 = nanmean(m3);
m_std3 = nanstd(m3,1);


fh3 = figure(3);
clf
set(fh3, 'color','white');

subplot(2,2,1)
imagesc([0 size_x],[0 size_y],m1)
title([ 'Chirp Up, mean = ' num2str(m_mean1,3) 'cm/kV'])
% % To display average with outliers, add full to above line (m_mean1_full)
caxis([ m_mean3-n_std*m_std3 m_mean3+n_std*m_std3 ])
colormap(jet)
colorbar
axis image


subplot(2,2,2)
imagesc([0 size_x],[0 size_y],m2)
title([ 'Chirp Down, mean = ' num2str(m_mean2,3) 'cm/kV'])
% % To display average with outliers, add full to above line (m_mean2_full)
caxis([ m_mean3-n_std*m_std3 m_mean3+n_std*m_std3 ])
colormap(jet)
colorbar
axis image


subplot(2,2,3)

m = m1 - m2;
m_mean = nanmean(nanmean(m));
m_std = nanstd(reshape(m,numel(m),1));

imagesc([0 size_x],[0 size_y],m)
title('Difference (cm/kV)')
```

```
caxis([ m_mean-n_std*m_std m_mean+n_std*m_std ])
colormap(jet)
colorbar
axis image

subplot(2,2,4)

m_tog = zeros(size(m1,1),size(m1,2),2);
m_tog(:,:,1) = m1;
m_tog(:,:,2) = m2;
m = nanmean(m_tog,3);

m_mean = nanmean(nanmean(m));
m_std = nanstd(reshape(m,numel(m),1));

imagesc([0 size_x],[0 size_y],m)
title(['Mean, mean = ' num2str(m_mean,3) 'cm/kV'])
caxis([ m_mean-n_std*m_std m_mean+n_std*m_std ])
colormap(jet)
colorbar
axis image

% % Plot histogram of a/d33
fh4 = figure(4);
clf
set(fh4, 'color','white');

m1D = reshape(m,numel(m),1);
bins = ceil((max(m1D) - min(m1D)) / bin_size);
inc = (max(m1D) - min(m1D))/bins;
edges = zeros(bins,1);

for k1 = 1 : bins

    edges(k1) = min(m1D) + (k1-1)*inc;

end

meana = nanmean(m1D);
stda = nanstd(m1D);
[~,~,ci] = ztest(m1D,meana,stda);
confa = meana-ci(1);
edgesc = edges';

[N,X] = hist(m1D,edgesc);
N = N' / sum(N) * 100;
X = X';
max_N = 10*ceil(max(N)/10);

n_elements = histc(m1D,edgesc);
c_elements = cumsum(n_elements)./(num_rows * num_cols)*100;

[ax h1 h2] = plotyy(X,N,edgesc,c_elements,'plot');
set(h1,'color','b')
```

```
set(h2,'color','r')
title(['Histogram, maximum = ' num2str(max(N),3) ', mean = ' num2str(meana,3)
' +/- ' num2str(confa,3) 'cm/kV'])

set(get(ax(1),'Ylabel'),'String','Relative Frequency','Color','k')
ylimits = get(ax(1),'YLim');
yinc = (ylimits(2)-ylimits(1))/5;
set(ax(1),'YColor','k','YTick',(ylimits(1):yinc:ylimits(2)))

set(get(ax(2),'Ylabel'),'String','Cumulative Frequency','Color','k')
ylimits = get(ax(2),'YLim');
yinc = (ylimits(2)-ylimits(1))/5;
set(ax(2),'YColor','k','YTick',(ylimits(1):yinc:ylimits(2)))

xlabel('quadratic / linear (cm/kV)');
axis(ax(1),[-max_out max_out 0 max_N])
axis(ax(2),[-max_out max_out 0 100])

% % Save figures and fit data

sav = input('Save fit data and figures? (y/n) ','s');

while ~((strcmpi(sav,'y')) || (strcmpi(sav,'n')))
    disp('Error: Invalid input.')
    sav = input('Save fit data and figures? (y/n) ','s');
end

if strcmpi(sav,'y')
    save([file_path '\' file_name
'\NLdata.mat'],'Vac_1','Vac_2','amp_mat3','p_1','p_2');
end
```

Appendix B: MATLAB Code for Bicrystal Analysis

```
close all
clear all
clc

% % comp is the composition (2, 4, 5) so maps can be plotted on same scale,
% % thick is the thickness of the film in µm,
% % boundary is the location of the g.b. in µm relative to the left edge of
% % the map, mean_film and std_film are the mean and std determined from
% % maps far from the g.b.

sample = 'SW510';
comp = 5;
thick = 0.3901;
boundary = 2.424;
mean_film = -1.2127*10^-3;
std_film = 3.9837*10^-3;

% % low_x is the minimum x when masking near the boundary, high_x is the
% % maximum x for the same, max_out and max_out_2 define beyond what values
% in nl to change to NaN, min_size is the minimum size of clusters

low_x = 0;
high_x = 2.778;
max_out = 0.05;
min_size = 10;

% % connect is connectivity of clusters (4 or 8), range is how many indices
% ± boundary clusters must be in, size_x and size_y are the size of the
% map, n_std is the # std for plotting colorbar; frac_low is the # std for
% defining high / low clusters

max_out_2 = 0.002;
connect = 4;
range = 2;
cut_nl = 0.5;
cut_px = 40;
size_x = 5;
size_y = 5;
n_std = 2;
frac_low = 1/2;

file_path = ['/Users/SilverMonarch/Desktop/CNMS/BicrystalData/' sample
'/boundary_nl'];
file_name = 'NLdata.mat';
load([ file_path '/' file_name ])
txtsize = 10;

nl_1 = p_1(2:end,:,1)./p_1(2:end,:,2)/10*thick;
```

```
nl_2 = p_2(2:end,:,1)./p_2(2:end,:,2)/10*thick;
threshold1 = find(abs(nl_1)>max_out);
nl_1(threshold1) = NaN;
threshold2 = find(abs(nl_2)>max_out);
nl_2(threshold2) = NaN;
nl = (nl_1+nl_2)/2;

if strcmp(sample,'SW530')
    threshold3 = find(nl(:,low_x*20:high_x*20)>max_out_2)+(low_x*20-1)*99;
    nl(threshold3) = NaN;
end

[u,v] = size(nl);

ind_y = (u-1)/size_y;
ind_x = (v-1)/size_x;

b_x = round(ind_x*boundary + 1);
min_x = round(ind_x*low_x + 1);
max_x = round(ind_x*high_x + 1);

high_x = (max_x-1)/ind_x;
low_x = (min_x-1)/ind_x;
boundary = (b_x-1)/ind_x;

bound_x = ones(101,1)*boundary;
bound_y = [0:0.05:5];

nl_mat1 = reshape(nl,u*v,1);
mean_nl = nanmean(nl_mat1);
std_nl = nanstd(nl_mat1);
[~, ~, ci] = ztest(nl_mat1,mean_nl,std_nl,0.05);
conf_nl = ci(2)-mean_nl;

% disp(['Mean: ' num2str(mean_nl*10^3) '+/-' num2str(conf_nl*10^3) ' x10^-3
cm/kV']);
% disp(['STDev: ' num2str(std_nl*10^3) ' x10^-3 cm/kV']);

mean_nl = mean_film;
std_nl = std_film;


%% Reduce map to boundary region to search for influence of boundary

nl_squish = nl(:,min_x:max_x);
b_squish = b_x-min_x+1;

[num_rows num_cols] = size(nl_squish);

% fh1 = figure(1);
% clf
% set(fh1, 'color','white');
% imagesc([low_x high_x],[0 size_y],nl_squish)
% caxis([ mean_nl-n_std*std_nl mean_nl+n_std*std_nl ])
```

```
% colormap(jet)
% a = colorbar;
% set(a,'FontName','Arial','FontSize',28,'LineWidth',1);
% axis image off


%% Find region with low nonlinearity

threshold_lo = mean_nl - frac_low*std_nl;

if strcmp(sample,'SW530')
    nl_lo = (nl_squish < threshold_lo) + isnan(nl_squish);
else
    nl_lo = (nl_squish < threshold_lo);
end
nl_lo = imfill(nl_lo, 'holes');

nl_total_lo = sum(sum(nl_lo));
nl_lo_per_row = nl_total_lo / num_rows;
nl_bound_influence = nl_lo_per_row / ind_x;

[m_lo n] = bwlabel(nl_lo,connect);
mall_lo = m_lo;

for k = 1:n
    [y,x] = find(m_lo == k);
    if size(x,1) < min_size
        m_lo(y,x) = 0;
        mall_lo(y,x) = 0;
    end

    a = x > b_squish - range;
    b = x < b_squish + range;
    c = a + b;
    z = find(c == 2);
    if size(z,1) == 0
        m_lo(y,x) = 0;
    end
end

m_lo = m_lo >= 1;
mall_lo = mall_lo >= 1;
m_total_lo = sum(sum(m_lo));
m_lo_per_row = m_total_lo / num_rows;
m_lo_calc = sum(m_lo,2) / (v/size_x);
m_mean_influence = mean(m_lo_calc);
m_std_influence = std(m_lo_calc);
[h p ci] = ztest(m_lo_calc,m_mean_influence,m_std_influence,0.05);
m_conf_influence = ci(2)-m_mean_influence;

% disp(['No. Pixels Low Per Row: ' num2str(m_lo_per_row)]);
disp(['Influence of Boundary: ' num2str(m_mean_influence) '+/-'
num2str(m_conf_influence)]);
disp(['Stdev of influence: ' num2str(m_std_influence)]);
```

```
% % % Plot all region boundaries on map
% fh2 = figure(2);
% clf
% set(fh2, 'color','white');
% imagesc([0 size_x],[0 size_y],nl)
% caxis([ mean_nl-n_std*std_nl mean_nl+n_std*std_nl ])
% colormap(jet)
% a = colorbar;
% set(a,'FontName','Arial','FontSize',28,'LineWidth',1);
% axis image off
%
% nl_lo_bound = bwboundaries(nl_lo);
% for k = 1 : size(nl_lo_bound)
%     this_bound = nl_lo_bound{k};
%     this_bound(:,2) = (this_bound(:,2)-1) / ind_x + low_x;
%     this_bound(:,1) = (this_bound(:,1)-1) / ind_y;
%     hold on;
%     plot(this_bound(:,2), this_bound(:,1), 'k', 'LineWidth', 2);
% end
% hold on;
% plot(bound_x,bound_y, 'k', 'LineStyle', '--', 'LineWidth', 2)
% hold off;


%% Plot large region boundaries on map

fh3 = figure(3);
clf
set(fh3,'Units','inches','Position',[1 6 2.333 2.333],'PaperPosition',[0 0
2.333 2.333],'color','white');

imagesc([0 size_x],[0 size_y],nl*10^3)
col = colorbar('FontName','Arial','FontSize',txtsize,'LineWidth',1);
title(col,'(10^{-3}
cm/kV)','FontName','Arial','FontSize',txtsize,'HorizontalAlignment','center',
'VerticalAlignment','top','Position',[1.5 (mean_nl+n_std*std_nl*1.3)*10^3 1])
caxis([ mean_nl-n_std*std_nl mean_nl+n_std*std_nl ]*10^3)
axis image off
set(gca,'OuterPosition',[-0.075 0 0.9 1])
ca = get(col,'Position');
set(col,'Position',[0.75 0.175 ca(3) 0.68])

m_lo_bound = bwboundaries(m_lo);
for k = 1 : size(m_lo_bound)
    this_bound = m_lo_bound{k};
    this_bound(:,2) = (this_bound(:,2)-1) / ind_x + low_x;
    this_bound(:,1) = (this_bound(:,1)-1) / ind_y;
    hold on;
    plot(this_bound(:,2), this_bound(:,1), 'k', 'LineWidth', 1);
end
hold on;
plot(bound_x,bound_y, 'k', 'LineStyle', '--', 'LineWidth', 1)
hold off;
```

```
% Below for 5x5µm scale bar
rectangle('Position',[0 4.4 1.6 0.6],'FaceColor','k')
rectangle('Position',[0.3 4.85 1 0.1],'FaceColor','w')
text(0.8,4.625,'1
µm','FontSize',txtsize,'Color','w','HorizontalAlignment','center','VerticalAl
ignment','middle')

saveas(fh3,[file_path '/' file_name '_' 'nl_cluster' '.png'],'png');
print(fh3,'-dtiff','-r300','-painters',[file_path '/' file_name
'_nl_cluster.tiff'])


%% Plot large region boundaries on scaled map

if comp == 4
    map_mean = 1.84301*10^-3;
    map_std = 5.06486*10^-3;
else if comp == 5
        map_mean = -1.5557*10^-3;
        map_std = 1.4648*2*10^-3;
    else
        map_mean = -0.66035*10^-3;
        map_std = 1.7328*10^-3;
    end
end

fh4 = figure(4);
clf
set(fh4,'Units','inches','Position',[1 3 2.333 2.333],'PaperPosition',[0 0
2.333 2.333],'color','white');

imagesc([0 size_x],[0 size_y],nl*10^3)
col = colorbar('FontName','Arial','FontSize',txtsize,'LineWidth',1);
title(col,'(10^{-3}
cm/kV)','FontName','Arial','FontSize',txtsize,'HorizontalAlignment','center',
'VerticalAlignment','top','Position',[1.5 (map_mean+n_std*map_std*1.3)*10^3
1])
caxis([ map_mean-n_std*map_std map_mean+n_std*map_std ]*10^3)
axis image off
set(gca,'OuterPosition',[-0.075 0 0.9 1])
ca = get(col,'Position');
set(col,'Position',[0.75 0.175 ca(3) 0.68])

m_lo_bound = bwboundaries(m_lo);
for k = 1 : size(m_lo_bound)
    this_bound = m_lo_bound{k};
    this_bound(:,2) = (this_bound(:,2)-1) / ind_x + low_x;
    this_bound(:,1) = (this_bound(:,1)-1) / ind_y;
    hold on;
    plot(this_bound(:,2), this_bound(:,1), 'k', 'LineWidth', 1);
end
hold on;
plot(bound_x,bound_y, 'k', 'LineStyle', '--', 'LineWidth', 1)
hold off;
```

```
% Below for 5x5µm scale bar
rectangle('Position',[0 4.4 1.6 0.6],'FaceColor','k')
rectangle('Position',[0.3 4.85 1 0.1],'FaceColor','w')
text(0.8,4.625,'1
µm','FontSize',txtsize,'Color','w','HorizontalAlignment','center','VerticalAl
ignment','middle')

saveas(fh4,[file_path '/' file_name '_' 'nl_cluster_scaled' '.png'],'png');
print(fh4,'-dtiff','-r300','-painters',[file_path '/' file_name
'_nl_cluster_scaled.tiff'])


%% Plot mean nonlinear response across x direction

x = ([0:1:v-1])/ind_x - bound_x(1);
x_nl = nanmean(nl,1)*10^3;

fh6 = figure(6);
clf
set(fh6,'Units','inches','Position',[1 0 2.333 2.333],'PaperPosition',[0 0
2.333 2.333],'color','white');

plot(x,x_nl,'LineWidth',1,'Color','k');
axis([x(1) x(end) floor(min(x_nl)) ceil(max(x_nl))])
hold on;
ylimits = get(gca,'YLim');
xlimits = get(gca,'XLim');
plot([0 0],ylimits,'--','color','k','LineWidth',1);
hold on;
plot(xlimits,[mean_nl mean_nl]*10^3,'--','color','k','LineWidth',1);
xlabel('x Position (\mum)','FontSize',txtsize)
ylabel('quadratic/linear (10^{-3} cm/kV)','FontSize',txtsize)
set(gca,'FontSize',txtsize,'LineWidth',1,'OuterPosition',[0 0 1 1],'XTick',[-
5 -4 -3 -2 -1 0 1 2 3 4 5])

saveas(fh6,[file_path '/' file_name '_' 'nl_average' '.png'],'png');
print(fh6,'-dtiff','-r300','-painters',[file_path '/' file_name
'_nl_average.tiff'])


fh7 = figure(7);
clf
set(fh7,'Units','inches','Position',[1 0 2.333 2.333],'PaperPosition',[0 0
2.333 2.333],'color','white');

plot(x,x_nl,'LineWidth',1,'Color','k');
axis([x(1) x(end) floor(min(x_nl)) ceil(max(x_nl))])
hold on;
ylimits = get(gca,'YLim');
xlimits = get(gca,'XLim');
plot([0 0],ylimits,'--','color','k','LineWidth',1);
hold on;
plot(xlimits,[mean_nl mean_nl]*10^3,'--','color','k','LineWidth',1);
hold on;
```

```
plot(xlimits,[mean_nl-0.25*std_nl mean_nl-0.25*std_nl]*10^3,'--
','color','r','LineWidth',1);
hold on;
plot(xlimits,[mean_nl+0.25*std_nl mean_nl+0.25*std_nl]*10^3,'--
','color','r','LineWidth',1);
% hold on;
% plot(xlimits,[mean_nl-0.5*std_nl mean_nl-0.5*std_nl]*10^3,'--
','color','r','LineWidth',1);
% hold on;
% plot(xlimits,[mean_nl+0.5*std_nl mean_nl+0.5*std_nl]*10^3,'--
','color','r','LineWidth',1);
xlabel('x Position (\mum)','FontSize',txtsize)
ylabel('quadratic/linear (10^{-3} cm/kV)','FontSize',txtsize)
set(gca,'FontSize',txtsize,'LineWidth',1,'OuterPosition',[0 0 1 1],'XTick',[-
5 -4 -3 -2 -1 0 1 2 3 4 5])

saveas(fh7,[file_path '/' file_name '_' 'nl_average_lines' '.png'],'png');
print(fh7,'-dtiff','-r300','-painters',[file_path '/' file_name
'_nl_average_lines.tiff'])

% % Plot mean nonlin across x direction on smaller scale

min_s = round(ind_x * (bound_x(1)-1.5)) + 1;
max_s = round(ind_x * (bound_x(1)+1.5)) + 1;

if min_s < 0
    min_s = 1;
    max_s = ind_x*3+1;
end

x_nl_s = x_nl(1,min_s:max_s);
v_s = size(x_nl_s,2);
x_s = ([min_s:1:max_s] - 1) / ind_x - bound_x(1);

fh8 = figure(8);
clf
set(fh8,'Menubar','none','Units','inches','OuterPosition',[3.5 1 6
2],'PaperPosition',[0 0 6 2],'color','white')
plot(x_s,x_nl_s,'LineWidth',1);
axis([-1.5 1.5 floor(min(x_nl)) ceil(max(x_nl))])
hold on;
ylimits = get(gca,'YLim');
xlimits = get(gca,'XLim');
plot([0 0],ylimits,'--','color','k','LineWidth',1);
hold on;
plot(xlimits,[mean_nl mean_nl]*10^3,'--','color','k','LineWidth',1);
xlabel('x Position (\mum)','FontSize',18)
ylabel('10^{-3} cm/kV','FontSize',18)
set(gca,'FontSize',18,'LineWidth',1)

saveas(fh8,[file_path '/' file_name '_' 'nl_average_short' '.png'],'png');
print(fh8,'-dtiff','-r300','-painters',[file_path '/' file_name
'_nl_average_short.tiff'])
```

```
b_mean = nanmean(nanmean(nl(:,b_x-range:b_x+range)));
variation = (mean_nl-b_mean)/std_nl;
disp(['Mean at boundary: ' num2str(b_mean*10^3) 'x10^-3 cm/kV    #std below
mean: ' num2str(variation)])

% % Calculate low response region based on mean-0.25*std

cut = (mean_nl - cut_nl*std_nl)*10^3;

if strcmp(sample,'SW530') || strcmp(sample,'SW510') || strcmp(sample,'SW430')
    Xp = x((x>-0.9) + (x<0.5)==2);
    Np = x_nl((x>-0.9) + (x<0.5)==2);
else
    Xp = x((x>-0.9) + (x<1)==2);
    Np = x_nl((x>-0.9) + (x<1)==2);
end

z_val = find(round(Xp*1000)==0);
bound_l = find(abs(Np(1:z_val)-cut)==min(abs(Np(1:z_val)-cut)));
bound_r = find(abs(Np(z_val:end)-cut)==min(abs(Np(z_val:end)-cut)))+z_val-1;

if Np(bound_l(1)) < cut
    bound_l = bound_l(1);
    bound_lp = bound_l - 1;
else
    bound_l = bound_l(end);
    bound_lp = bound_l + 1;
end

if Np(bound_r(1)) < cut
    bound_r = bound_r(end);
    bound_rp = bound_r + 1;
else
    bound_r = bound_r(1);
    bound_rp = bound_r - 1;
end

lim_l = (Xp(bound_l)*(Np(bound_lp)-cut)+Xp(bound_lp)*(cut-
Np(bound_l)))/(Np(bound_lp)-Np(bound_l));
lim_r = (Xp(bound_r)*(Np(bound_rp)-cut)+Xp(bound_rp)*(cut-
Np(bound_r)))/(Np(bound_rp)-Np(bound_r));

cut_width = lim_r-lim_l;

cconf_l = abs((Xp(bound_l)-Xp(bound_lp))/(Np(bound_l)-
Np(bound_lp))*0.05*std_nl*10^3);
cconf_r = abs((Xp(bound_r)-Xp(bound_rp))/(Np(bound_r)-
Np(bound_rp))*0.05*std_nl*10^3);

cut_conf = cconf_l+cconf_r;

lim_l_sl = lim_l;
lim_r_sl = lim_r;
cconf_l_sl = cconf_l;
cconf_r_sl = cconf_r;
```

```
disp([num2str(cut_nl*100) '% std low width: ' num2str(cut_width) '±'
num2str(cut_conf) ' um'])

% % Calculate high response region based on mean+0.25*std

cut = (mean_nl + cut_nl*std_nl)*10^3;

z_val = find(round(Xp*1000)==0);
bound_l = find(abs(Np(1:z_val)-cut)==min(abs(Np(1:z_val)-cut)));
bound_r = find(abs(Np(z_val:end)-cut)==min(abs(Np(z_val:end)-cut)))+z_val-1;

if Np(bound_l(1)) > cut
    bound_l = bound_l(1);
    bound_lp = bound_l - 1;
else
    bound_l = bound_l(end);
    bound_lp = bound_l + 1;
end

if Np(bound_r(1)) > cut
    bound_r = bound_r(end);
    bound_rp = bound_r + 1;
else
    bound_r = bound_r(1);
    bound_rp = bound_r - 1;
end

lim_l = (Xp(bound_l)*(Np(bound_lp)-cut)+Xp(bound_lp)*(cut-
Np(bound_l)))/(Np(bound_lp)-Np(bound_l));
lim_r = (Xp(bound_r)*(Np(bound_rp)-cut)+Xp(bound_rp)*(cut-
Np(bound_r)))/(Np(bound_rp)-Np(bound_r));

cut_width = lim_r-lim_l;

cconf_l = abs((Xp(bound_l)-Xp(bound_lp))/(Np(bound_l)-
Np(bound_lp))*0.05*std_nl*10^3);
cconf_r = abs((Xp(bound_r)-Xp(bound_rp))/(Np(bound_r)-
Np(bound_rp))*0.05*std_nl*10^3);

cut_conf = cconf_l+cconf_r;

lim_l_sh = lim_l;
lim_r_sh = lim_r;
lim_l_sh = lim_l;
lim_r_sh = lim_r;

disp([num2str(cut_nl*100) '% std high width: ' num2str(cut_width) '±'
num2str(cut_conf) ' um'])

%% Plot lateral histogram of low nonlinear response

m_lo = mall_lo;
```

```
[para_dist perp_dist] = find(m_lo == 1);
perp_dist_full = perp_dist + min_x - 1;
perp_dist_abs = (perp_dist_full - 1) / (v/size_x);
perp_dist_rel = perp_dist_abs - boundary*(v-1)/v;

bins = max(perp_dist) - min(perp_dist) + 1;
inc = (max(perp_dist_rel) - min(perp_dist_rel)) / (bins - 1);
edges = zeros(1,bins);

for k1 = 1 : bins + 2

    edges(k1) = min(perp_dist_rel) + (k1-2)*inc;

end

meana = nanmean(perp_dist_rel);
stda = nanstd(perp_dist_rel);
[~,~,ci] = ztest(perp_dist_rel,meana,stda);
confa = meana-ci(1);

[N,X] = hist(perp_dist_rel,edges);
N = N';
X = X';
max_N = 10*ceil(max(N)/10);

c_elements = cumsum(N)./size(perp_dist_rel,1)*100;

m_bins = max(N);
gbcenter = find(round(X*1000)==0);
z_bins = sum(N(gbcenter-1:gbcenter+1))/3;
ml_bins = X(N == m_bins);


cut = cut_px;

Xp = X((X>-1) + (X<1)==2);
Np = N((X>-1) + (X<1)==2);

z_val = find(round(Xp*1000)==0);
bound_l = find(abs(Np(1:z_val)-cut)==min(abs(Np(1:z_val)-cut)));
bound_r = find(abs(Np(z_val:end)-cut)==min(abs(Np(z_val:end)-cut)))+z_val-1;

if Np(bound_l(1)) > cut
    bound_l = bound_l(1);
    bound_lp = bound_l - 1;
else
    bound_l = bound_l(end);
    bound_lp = bound_l + 1;
end

if Np(bound_r(1)) > cut
    bound_r = bound_r(end);
    bound_rp = bound_r + 1;
else
```

```
    bound_r = bound_r(1);
    bound_rp = bound_r - 1;
end

lim_l = (Xp(bound_l)*(Np(bound_lp)-cut)+Xp(bound_lp)*(cut-
Np(bound_l)))/(Np(bound_lp)-Np(bound_l));
lim_r = (Xp(bound_r)*(Np(bound_rp)-cut)+Xp(bound_rp)*(cut-
Np(bound_r)))/(Np(bound_rp)-Np(bound_r));

cut_width = lim_r-lim_l;

cconf_l = abs((Xp(bound_l)-Xp(bound_lp))/(Np(bound_l)-Np(bound_lp))*5);
cconf_r = abs((Xp(bound_r)-Xp(bound_rp))/(Np(bound_r)-Np(bound_rp))*5);

cut_conf = cconf_l+cconf_r;

disp([num2str(cut) ' pixel width: ' num2str(cut_width) '±' num2str(cut_conf)
' um'])
disp(['# low pixels at GB: ' num2str(z_bins)])

cut = 35;
bound_l = find(abs(Np(1:z_val)-cut)==min(abs(Np(1:z_val)-cut)));
bound_r = find(abs(Np(z_val:end)-cut)==min(abs(Np(z_val:end)-cut)))+z_val-1;
bound_l = bound_l(1);
bound_r = bound_r(end);
if Np(bound_l(1)) > cut
    bound_l = bound_l(1);
    bound_lp = bound_l - 1;
else
    bound_l = bound_l(end);
    bound_lp = bound_l + 1;
end
if Np(bound_r(1)) > cut
    bound_r = bound_r(end);
    bound_rp = bound_r + 1;
else
    bound_r = bound_r(1);
    bound_rp = bound_r - 1;
end
lim_l = (Xp(bound_l)*(Np(bound_lp)-cut)+Xp(bound_lp)*(cut-
Np(bound_l)))/(Np(bound_lp)-Np(bound_l));
lim_r = (Xp(bound_r)*(Np(bound_rp)-cut)+Xp(bound_rp)*(cut-
Np(bound_r)))/(Np(bound_rp)-Np(bound_r));
cut_35 = lim_r-lim_l;

cut = 45;
bound_l = find(abs(Np(1:z_val)-cut)==min(abs(Np(1:z_val)-cut)));
bound_r = find(abs(Np(z_val:end)-cut)==min(abs(Np(z_val:end)-cut)))+z_val-1;
bound_l = bound_l(1);
bound_r = bound_r(end);
if Np(bound_l(1)) > cut
    bound_l = bound_l(1);
    bound_lp = bound_l - 1;
else
    bound_l = bound_l(end);
```

```
    bound_lp = bound_l + 1;
end
if Np(bound_r(1)) > cut
    bound_r = bound_r(end);
    bound_rp = bound_r + 1;
else
    bound_r = bound_r(1);
    bound_rp = bound_r - 1;
end
lim_l = (Xp(bound_l)*(Np(bound_lp)-cut)+Xp(bound_lp)*(cut-
Np(bound_l)))/(Np(bound_lp)-Np(bound_l));
lim_r = (Xp(bound_r)*(Np(bound_rp)-cut)+Xp(bound_rp)*(cut-
Np(bound_r)))/(Np(bound_rp)-Np(bound_r));
cut_45 = lim_r-lim_l;

cut_conf2 = (cut_35-cut_45) / 2;

disp(['Confidence on 40p width by 35 to 45: ' num2str(cut_conf2)]);

fh9 = figure(9);
clf
set(fh9,'Units','inches','Position',[10 0 2.333 2.333],'PaperPosition',[0 0
2.333 2.333],'color','white');

plot(X,N,'LineWidth',1,'Color','k');
axis([X(1) X(end) 0 100])
hold on;
ylimits = get(gca,'YLim');
xlimits = get(gca,'XLim');
plot([0 0],ylimits,'--','color','k','LineWidth',1);
hold on;
plot(xlimits,[40 40],'--','color','r','LineWidth',1);
xlabel('x Position (\mum)','FontSize',txtsize)
ylabel('Number of Low Response Pixels','FontSize',txtsize)
set(gca,'FontSize',txtsize,'LineWidth',1)

saveas(fh9,[file_path '/' file_name '_' 'GB_hist' '.png'],'png');
print(fh9,'-dtiff','-r300','-painters',[file_path '/' file_name
'_GB_hist.tiff'])
```

References

[1] R. Vasudevan, D. Marincel, S. Jesse, Y. Kim, A. Kumar, S. Kalinin, and S. Trolier-McKinstry, "Polarization dynamics in ferroelectric capacitors: Local perspective on emergent collective behavior and memory effects," *Adv. Funct. Mater.*, vol. 23, no. 20, pp. 2490–2508, Apr. 2013.

[2] D. M. Marincel, H. Zhang, A. Kumar, S. Jesse, S. V Kalinin, W. M. Rainforth, I. M. Reaney, C. A. Randall, and S. Trolier-McKinstry, "Influence of a single grain boundary on domain wall motion in ferroelectrics," *Adv. Funct. Mater.*, vol. 24, no. 10, pp. 1409–1417, Mar. 2014.

[3] B. Jaffe, W. R. Cook, and H. Jaffe, *Piezoelectric Ceramics*. New York, NY: Academic Press, 1971.

[4] M. E. Lines and A. M. Glass, *Principles and Applications of Ferroelectrics and Related Materials*. New York, NY: Oxford University Press, Inc., 1977.

[5] R. E. Newnham, *Properties of Materials: Anisotropy, Symmetry, Structure*. New York, NY: Oxford University Press, Inc., 2005.

[6] J. F. Scott, "Ferroelectrics go bananas," *J. Phys. Condens. Matter*, vol. 20, no. 2, p. 021001, Jan. 2008.

[7] J. S. Speck, A. Seifert, W. Pompe, and R. Ramesh, "Domain configurations due to multiple misfit relaxation mechanisms in epitaxial ferroelectric thin films. II. Experimental verification and implications," *J. Appl. Phys.*, vol. 76, no. 1, p. 477, 1994.

[8] G. Arlt, "Twinning in ferroelectric and ferroelastic ceramics: stress relief," *J. Mater. Sci.*, vol. 25, p. 2655, 1990.

[9] J. Fousek, "Permissible domain walls in ferroelectric species," *Czechoslov. J. Phys.*, vol. 21, no. 9, pp. 955–968, Sep. 1971.

[10] S. Trolier-McKinstry, "Crystal chemistry of piezoelectric materials," in *Piezoelectric and Acoustic Materials for Transducer Applications*, A. Safari and E. K. Akdogan, Eds. New York, NY: Springer New York, 2008, pp. 39–56.

[11] I. D. Mayergoyz, "Mathematical models of hysteresis," *Phys. Rev. Lett.*, vol. 56, no. 15, pp. 1518–1521, 1986.

[12] A. J. Moulson and J. M. Herbert, *Electroceramics*. England: John Wiley & Sons Ltd, 2003.

[13] P. B. Jamieson, S. C. Abrahams, and J. L. Bernstein, "Ferroelectric tungsten bronze-type crystal structures. I. Barium strontium niobate $Ba_{0.27}Sr_{0.75}Nb_2O_{5.78}$," *J. Chem. Phys.*, vol. 48, no. 11, p. 5048, 1968.

[14] M. Ueda, H. Yasuda, and Y. Umakoshi, "Effect of grain boundary on martensite transformation behaviour in Fe–32 at.%Ni bicrystals," *Sci. Technol. Adv. Mater.*, vol. 3, no. 2, pp. 171–179, Mar. 2002.

[15] X. L. Zhang, Z. X. Chen, L. E. Cross, and W. A. Schulze, "Dielectric and piezoelectric properties of modified lead titanate zirconate ceramics from 4.2 to 300K," *J. Mater. Sci.*, vol. 18, pp. 968–972, 1983.

[16] D. Damjanovic and M. Demartin, "Contribution of the irreversible displacement of domain walls to the piezoelectric effect in barium titanate and lead zirconate titanate ceramics," *J. Phys. Condens. Matter*, vol. 9, pp. 4943–4953, 1997.

[17] A. Pramanick, D. Damjanovic, J. E. Daniels, J. C. Nino, and J. L. Jones, "Origins of electro-mechanical coupling in polycrystalline ferroelectrics during subcoercive electrical loading," *J. Am. Ceram. Soc.*, vol. 94, no. 2, pp. 293–309, Feb. 2011.

[18] D. V. Taylor and D. Damjanovic, "Domain wall pinning contribution to the nonlinear dielectric permittivity in Pb(Zr, Ti)O3 thin films," *Appl. Phys. Lett.*, vol. 73, no. 14, pp. 2045–2047, 1998.

[19] S. Trolier-McKinstry, N. Bassiri-Gharb, and D. Damjanovic, "Piezoelectric nonlinearity due to motion of 180° domain walls in ferroelectric materials at subcoercive fields: A dynamic poling model," *Appl. Phys. Lett.*, vol. 88, no. 20, p. 202901, 2006.

[20] R. Bechmann, "Elastic and piezoelectric constants of alpha-quartz," *Phys. Rev.*, vol. 110, no. 5, pp. 1060–1061, 1958.

[21] O. Boser, "Statistical theory of hysteresis in ferroelectric materials," *J. Appl. Phys.*, vol. 62, no. 4, p. 1344, 1987.

[22] D. Damjanovic and M. Demartin, "The Rayleigh law in piezoelectric ceramics," *J. Phys. D. Appl. Phys.*, vol. 29, no. 7, pp. 2057–2060, Jul. 1996.

[23] D. Damjanovic, S. S. N. Bharadwaja, and N. Setter, "Toward a unified description of nonlinearity and frequency dispersion of piezoelectric and dielectric responses in $Pb(Zr,Ti)O_3$," *Mater. Sci. Eng. B*, vol. 120, no. 1–3, pp. 170–174, Jul. 2005.

[24] M. I. Morozov, D. Damjanovic, and N. Setter, "The nonlinearity and subswitching hysteresis in hard and soft PZT," *J. Eur. Ceram. Soc.*, vol. 25, no. 12, pp. 2483–2486, Jan. 2005.

[25] I. Fujii, M. Ugorek, Y. Han, and S. Trolier-McKinstry, “Effect of oxygen partial pressure during firing on the high AC field response of $BaTiO_3$ dielectrics,” *J. Am. Ceram. Soc.*, vol. 93, no. 4, pp. 1081–1088, Apr. 2010.

[26] M. Demartin and D. Damjanovic, “Dependence of the direct piezoelectric effect in coarse and fine grain barium titanate ceramics on dynamic and static pressure,” *Appl. Phys. Lett.*, vol. 68, no. 21, p. 3046, 1996.

[27] I. Fujii, M. Ugorek, and S. Trolier-McKinstry, “Grain size effect on the dielectric nonlinearity of $BaTiO_3$ ceramics,” *J. Appl. Phys.*, vol. 107, no. 10, p. 104116, 2010.

[28] D. Damjanovic, “Logarithmic frequency dependence of the piezoelectric effect due to pinning of ferroelectric-ferroelastic domain walls,” *Phys. Rev. B*, vol. 55, no. 2, pp. 649–652, 1997.

[29] D. A. Hall, “Nonlinearity in piezoelectric ceramics,” *J. Mater. Sci.*, vol. 36, pp. 4575–4601, 2001.

[30] N. Bassiri-Gharb, I. Fujii, E. Hong, S. Trolier-McKinstry, D. V. Taylor, and D. Damjanovic, “Domain wall contributions to the properties of piezoelectric thin films,” *J. Electroceramics*, vol. 19, no. 1, pp. 49–67, Mar. 2007.

[31] F. Griggio, S. Jesse, A. Kumar, O. Ovchinnikov, H. Kim, T. N. Jackson, D. Damjanovic, S. V. Kalinin, and S. Trolier-McKinstry, “Substrate clamping effects on irreversible domain wall dynamics in lead zirconate titanate thin films,” *Phys. Rev. Lett.*, vol. 108, no. 15, p. 157604, Apr. 2012.

[32] V. Nagarajan, A. Roytburd, A. Stanishevsky, S. Prasertchoung, T. Zhao, L. Chen, J. Melngailis, O. Auciello, and R. Ramesh, “Dynamics of ferroelastic domains in ferroelectric thin films.,” *Nat. Mater.*, vol. 2, no. 1, pp. 43–7, Jan. 2003.

[33] P. Gao, C. T. Nelson, J. R. Jokisaari, S.-H. Baek, C. W. Bark, Y. Zhang, E. Wang, D. G. Schlom, C.-B. Eom, and X. Pan, “Revealing the role of defects in ferroelectric switching with atomic resolution,” *Nat. Commun.*, vol. 2, p. 591, Jan. 2011.

[34] P. Paruch, A. B. Kolton, X. Hong, C. H. Ahn, and T. Giamarchi, “Thermal quench effects on ferroelectric domain walls,” *Phys. Rev. B*, vol. 85, no. 21, p. 214115, Jun. 2012.

[35] P. Jakes, E. Erdem, R.-A. Eichel, L. Jin, and D. Damjanovic, “Position of defects with respect to domain walls in Fe^{3+}-doped $Pb[Zr_{0.52}Ti_{0.48}]O_3$ piezoelectric ceramics,” *Appl. Phys. Lett.*, vol. 98, no. 7, p. 072907, 2011.

[36] A. Chandrasekaran, D. Damjanovic, N. Setter, and N. Marzari, “Defect ordering and defect–domain-wall interactions in $PbTiO_3$: A first-principles study,” *Phys. Rev. B*, vol. 88, no. 21, p. 214116, Dec. 2013.

[37] S. Choudhury, Y. L. Li, C. Krill III, and L.-Q. Chen, “Effect of grain orientation and grain size on ferroelectric domain switching and evolution: Phase field simulations,” *Acta Mater.*, vol. 55, no. 4, pp. 1415–1426, Feb. 2007.

[38] G. Arlt, D. F. Hennings, and G. de With, “Dielectric properties of fine-grained barium titanate ceramics,” *J. Appl. Phys.*, vol. 58, no. 4, p. 1985, 1985.

[39] D. A. Hall, A. Steuwer, B. Cherdhirunkorn, T. Mori, and P. J. Withers, “A high energy synchrotron x-ray study of crystallographic texture and lattice strain in soft lead zirconate titanate ceramics,” *J. Appl. Phys.*, vol. 96, no. 8, p. 4245, 2004.

[40] P. Gao, J. Britson, J. R. Jokisaari, C. T. Nelson, S.-H. Baek, Y. Wang, C.-B. Eom, L.-Q. Chen, and X. Pan, “Atomic-scale mechanisms of ferroelastic domain-wall-mediated ferroelectric switching,” *Nat. Commun.*, vol. 4, no. 2791, p. 2791, Jan. 2013.

[41] B. D. Huey and R. Nath, “High-speed piezo force microscopy: novel observations of ferroelectric domain poling, nucleation, and growth,” in *Scanning Probe Microscopy of Functional Materials: Nanoscale Imaging and Spectroscopy*, S. V. Kalinin and A. Gruverman, Eds. New York, NY: Springer New York, 2011, pp. 329–344.

[42] G. Arlt and N. A. Pertsev, “Force constant and effective mass of 90° domain walls in ferroelectric ceramics,” *J. Appl. Phys.*, vol. 70, no. 4, p. 2283, 1991.

[43] A. Pramanick, A. D. Prewitt, J. S. Forrester, and J. L. Jones, “Domains, domain walls and defects in perovskite ferroelectric oxides: A review of present understanding and recent contributions,” *Crit. Rev. Solid State Mater. Sci.*, vol. 37, no. 4, pp. 243–275, Dec. 2012.

[44] A. Y. Emelyanov and N. A. Pertsev, “Abrupt changes and hysteretic behavior of 90º domains in epitaxial ferroelectric thin films with misfit dislocations,” *Phys. Rev. B*, vol. 68, no. 21, p. 214103, Dec. 2003.

[45] X. Tan and J. K. Shang, “Partial dislocations at domain intersections in a tetragonal ferroelectric crystal,” *J. Phys. Condens. Matter*, vol. 16, no. 8, pp. 1455–1466, Mar. 2004.

[46] J. P. Sethna, K. A. Dahmen, and C. R. Myers, “Crackling noise,” *Nature*, vol. 410, pp. 242–250, 2001.

[47] O. Perkovic, K. Dahmen, and J. P. Sethna, “Avalanches, barkhausen noise, and plain old criticality,” *Phys. Rev. Lett.*, vol. 75, no. 24, pp. 4528–4531, 1995.

[48] X. Ding, T. Lookman, Z. Zhao, a. Saxena, J. Sun, and E. K. H. Salje, “Dynamically strained ferroelastics: Statistical behavior in elastic and plastic regimes,” *Phys. Rev. B*, vol. 87, no. 9, p. 094109, Mar. 2013.

[49] S. Choudhury, Y. Li, C. Krill III, and L.-Q. Chen, “Phase-field simulation of polarization switching and domain evolution in ferroelectric polycrystals,” *Acta Mater.*, vol. 53, no. 20, pp. 5313–5321, Dec. 2005.

[50] P. Marton, T. Shimada, T. Kitamura, and C. Elsässer, “First-principles study of the interplay between grain boundaries and domain walls in ferroelectric $PbTiO_3$,” *Phys. Rev. B*, vol. 83, no. 6, p. 064110, Feb. 2011.

[51] P. Paruch, T. Tybell, and J.-M. Triscone, “Nanoscale control of ferroelectric polarization and domain size in epitaxial $Pb(Zr_{0.2}Ti_{0.8})O_3$ thin films,” *Appl. Phys. Lett.*, vol. 79, no. 4, p. 530, 2001.

[52] T. Tybell, P. Paruch, T. Giamarchi, and J.-M. Triscone, “Domain wall creep in epitaxial ferroelectric $Pb(Zr_{0.2}Ti_{0.8})O_3$ thin films,” *Phys. Rev. Lett.*, vol. 89, no. 9, p. 097601, Aug. 2002.

[53] P. Paruch, T. Giamarchi, and J.-M. Triscone, “Domain wall creep in mixed c-a axis $Pb(Zr_{0.2}Ti_{0.8})O_3$ thin films,” *Ann. Phys.*, vol. 13, no. 1–2, pp. 95–96, Jan. 2004.

[54] J. Guyonnet, H. Béa, and P. Paruch, “Lateral piezoelectric response across ferroelectric domain walls in thin films,” *J. Appl. Phys.*, vol. 108, no. 4, p. 042002, 2010.

[55] J. Guyonnet, I. Gaponenko, S. Gariglio, and P. Paruch, “Conduction at domain walls in insulating $Pb(Zr_{0.2}Ti_{0.8})O_3$ thin films.,” *Adv. Mater.*, vol. 23, no. 45, pp. 5377–82, Dec. 2011.

[56] P. Paruch and J.-M. Triscone, “High-temperature ferroelectric domain stability in epitaxial $PbZr_{0.2}Ti_{0.8}O_3$ thin films,” *Appl. Phys. Lett.*, vol. 88, no. 16, p. 162907, 2006.

[57] S. Jesse, S. V Kalinin, R. Proksch, A. P. Baddorf, and B. J. Rodriguez, “The band excitation method in scanning probe microscopy for rapid mapping of energy dissipation on the nanoscale,” *Nanotechnology*, vol. 18, no. 43, p. 435503, Oct. 2007.

[58] S. Jesse, P. Maksymovych, and S. V Kalinin, “Rapid multidimensional data acquisition in scanning probe microscopy applied to local polarization dynamics and voltage dependent contact mechanics,” *Appl. Phys. Lett.*, vol. 93, no. 11, p. 112903, 2008.

[59] P. Bintachitt, S. Jesse, D. Damjanovic, Y. Han, I. M. Reaney, S. Trolier-McKinstry, and S. V Kalinin, “Collective dynamics underpins Rayleigh behavior in disordered polycrystalline ferroelectrics,” *Proc. Natl. Acad. Sci. U. S. A.*, vol. 107, no. 16, pp. 7219–24, Apr. 2010.

[60] F. Griggio, S. Jesse, A. Kumar, D. M. Marincel, D. S. Tinberg, S. V. Kalinin, and S. Trolier-McKinstry, “Mapping piezoelectric nonlinearity in the Rayleigh regime using band excitation piezoresponse force microscopy,” *Appl. Phys. Lett.*, vol. 98, no. 21, p. 212901, 2011.

[61] N. Setter, D. Damjanovic, L. Eng, G. Fox, S. Gevorgian, S.-K. Hong, A. I. Kingon, H. Kohlstedt, N. Y. Park, G. B. Stephenson, I. Stolichnov, A. K. Tagantsev, D. V. Taylor, T. Yamada, and S. K. Streiffer, "Ferroelectric thin films: Review of materials, properties, and applications," *J. Appl. Phys.*, vol. 100, no. 5, p. 051606, 2006.

[62] I. Fujii, E. Hong, and S. Trolier-McKinstry, "Thickness dependence of dielectric nonlinearity of lead zirconate titanate films," *IEEE Trans. Ultrason. Ferroelectr. Freq. Control*, vol. 57, no. 8, pp. 1717–1723, 2010.

[63] N. a. Pertsev and G. Arlt, "Forced translational vibrations of 90° domain walls and the dielectric dispersion in ferroelectric ceramics," *J. Appl. Phys.*, vol. 74, no. 6, p. 4105, 1993.

[64] P. Bintachitt, S. Trolier-McKinstry, K. Seal, S. Jesse, and S. V Kalinin, "Switching spectroscopy piezoresponse force microscopy of polycrystalline capacitor structures," *Appl. Phys. Lett.*, vol. 94, no. 4, p. 042906, 2009.

[65] F. Griggio, S. Jesse, W. Qu, A. Kumar, O. Ovchinnikov, D. S. Tinberg, S. V Kalinin, and S. Trolier-McKinstry, "Composition dependence of local piezoelectric nonlinearity in $(0.3)Pb(Ni_{0.33}Nb_{0.67})O_3$-$(0.7)Pb(Zr_xTi_{1-x})O_3$ films," *J. Appl. Phys.*, vol. 110, no. 4, p. 044109, 2011.

[66] S. Bühlmann, B. Dwir, J. Baborowski, and P. Muralt, "Size effect in mesoscopic epitaxial ferroelectric structures: Increase of piezoelectric response with decreasing feature size," *Appl. Phys. Lett.*, vol. 80, no. 17, p. 3195, 2002.

[67] S. Bharadwaja, P. Moses, S. Trolier-McKinstry, T. Mayer, P. Bettotti, and L. Pavesi, "Ferroelectric and ferroelastic domain wall motion in unconstrained $Pb(Zr,Ti)O_3$ microtubes and thin films.," *IEEE Trans. Ultrason. Ferroelectr. Freq. Control*, vol. 57, no. 4, pp. 792–800, Apr. 2010.

[68] A. Bernal, A. Tselev, S. Kalinin, and N. Bassiri-Gharb, "Free-standing ferroelectric nanotubes processed via soft-template infiltration.," *Adv. Mater.*, vol. 24, no. 9, pp. 1160–5, Mar. 2012.

[69] A. Pramanick, D. Damjanovic, J. C. Nino, and J. L. Jones, "Subcoercive cyclic electrical loading of lead zirconate titanate ceramics I: Nonlinearities and losses in the converse piezoelectric effect," *J. Am. Ceram. Soc.*, vol. 92, no. 10, pp. 2291–2299, Oct. 2009.

[70] L. W. Chang, M. McMillen, and J. M. Gregg, "The influence of point defects and inhomogeneous strain on the functional behavior of thin film ferroelectrics," *Appl. Phys. Lett.*, vol. 94, no. 21, p. 212905, 2009.

[71] C. T. Nelson, P. Gao, J. R. Jokisaari, C. Heikes, C. Adamo, A. Melville, S.-H. Baek, C. M. Folkman, B. Winchester, Y. Gu, Y. Liu, K. Zhang, E. Wang, J. Li, L.-Q. Chen, C.-B.

Eom, D. G. Schlom, and X. Pan, “Domain dynamics during ferroelectric switching,” *Science (80).*, vol. 334, no. 6058, pp. 968–71, Nov. 2011.

[72] W. Cao and C. A. Randall, “Grain size and domain size relations in bulk ceramic materials,” *J. Phys. Chem. Solids*, vol. 57, no. 10, pp. 1499–1505, 1996.

[73] J. W. Jang, H.-J. Youn, C. Byun, I.-T. Kim, and K. S. Hong, “Ferroelectric domain structures of polycrystalline $PbTiO_3$ thin films prepared by MOCVD,” *Ferroelectrics*, vol. 227, pp. 15–28, 1999.

[74] W. Zhang and K. Bhattacharya, “A computational model of ferroelectric domains. Part II: grain boundaries and defect pinning,” *Acta Mater.*, vol. 53, no. 1, pp. 199–209, Jan. 2005.

[75] C. A. Randall, N. Kim, J.-P. Kucera, W. Cao, and T. R. Shrout, “Intrinsic and extrinsic size effects in fine-grained morphotropic-phase-boundary lead zirconate titanate ceramics,” *J. Am. Ceram. Soc.*, vol. 81, no. 3, pp. 677–88, 1998.

[76] F. Griggio and S. Trolier-McKinstry, “Grain size dependence of properties in lead nickel niobate-lead zirconate titanate films,” *J. Appl. Phys.*, vol. 107, no. 2, p. 024105, 2010.

[77] Y. W. So, D. J. Kim, T. W. Noh, J.-G. Yoon, and T. K. Song, “Polarization-switching mechanisms for epitaxial ferroelectric $Pb(Zr,Ti)O_3$ films,” *J. Korean Phys. Soc.*, vol. 46, no. 1, pp. 40–43, 2005.

[78] B. D. Huey, R. Nath, S. Lee, and N. A. Polomoff, “High speed SPM applied for direct nanoscale mapping of the influence of defects on ferroelectric switching dynamics,” *J. Am. Ceram. Soc.*, vol. 95, no. 4, pp. 1147–1162, Apr. 2012.

[79] R. Nath, R. E. García, J. E. Blendell, and B. D. Huey, “The influence of grain boundaries and texture on ferroelectric domain hysteresis,” *JOM*, vol. 59, no. 1, pp. 17–21, 2007.

[80] S. V. Kalinin, S. Jesse, B. J. Rodriguez, Y. H. Chu, R. Ramesh, E. A. Eliseev, and A. N. Morozovska, “Probing the role of single defects on the thermodynamics of electric-field induced phase transitions,” *Phys. Rev. Lett.*, vol. 100, no. 15, p. 155703, Apr. 2008.

[81] V. Nagarajan, S. Aggarwal, A. Gruverman, R. Ramesh, and R. Waser, “Nanoscale polarization relaxation in a polycrystalline ferroelectric thin film: Role of local environments,” *Appl. Phys. Lett.*, vol. 86, no. 26, p. 262910, 2005.

[82] A. Bernal, A. Tselev, S. V. Kalinin, and N. Bassiri-Gharb, “Effects of lateral and substrate constraint on the piezoresponse of ferroelectric nanostructures,” *Appl. Phys. Lett.*, vol. 101, no. 11, p. 112901, 2012.

[83] D. S. Tinberg, R. L. Johnson-Wilke, D. D. Fong, T. T. Fister, S. K. Streiffer, Y. Han, I. M. Reaney, and S. Trolier-McKinstry, “Octahedral tilt transitions in relaxed epitaxial $Pb(Zr_{1-x}Ti_x)O_3$ films,” *J. Appl. Phys.*, vol. 109, no. 9, p. 094104, 2011.

[84] B. M. Park and S. J. Chung, “Optical, electron microscopic, and x-ray topographic studies of ferroic domains in barium titanate crystals grown from high-temperature solution,” *J. Am. Ceram. Soc.*, vol. 77, no. 12, pp. 3193–3201, Dec. 1994.

[85] I. A. Cutter and R. McPherson, “Surface domain reorientation produced by abrasion and annealing of polycrystalline BaTiO3,” *J. Am. Ceram. Soc.*, vol. 55, no. 7, pp. 334–336, 1972.

[86] I. B. Misirlioglu, A. L. Vasiliev, S. P. Alpay, M. Aindow, and R. Ramesh, “Defect microstructures in epitaxial $PbZr_{0.2}Ti_{0.8}O_3$ films grown on (001) $SrTiO_3$ by pulsed laser deposition,” *J. Mater. Sci.*, vol. 41, no. 3, pp. 697–707, Feb. 2006.

[87] C. J. Lu, L. A. Bendersky, K. Chang, and I. Takeuchi, “Dissociation and evolution of threading dislocations in epitaxial $Ba_{0.3}Sr_{0.7}TiO_3$ thin films grown on (001) $LaAlO_3$,” *J. Appl. Phys.*, vol. 93, no. 1, p. 512, 2003.

[88] J. Fousek and V. Janovec, “The orientation of domain walls in twinned ferroelectric crystals,” *J. Appl. Phys.*, vol. 40, no. 1, p. 135, 1969.

[89] G. Arlt, “Microstructure and domain effects in ferroelectric ceramics,” *Ferroelectrics*, vol. 91, pp. 3–7, 1989.

[90] J. F. Scott, “Cylinder stress in nanostructures: effect on domains in nanowires, nanotubes, and nano-disks.,” *J. Phys. Condens. Matter*, vol. 26, no. 21, p. 212202, May 2014.

[91] J. F. Ihlefeld, A. M. Vodnick, S. P. Baker, W. J. Borland, and J.-P. Maria, “Extrinsic scaling effects on the dielectric response of ferroelectric thin films,” *J. Appl. Phys.*, vol. 103, no. 7, p. 074112, 2008.

[92] R. E. García, B. D. Huey, and J. E. Blendell, “Virtual piezoforce microscopy of polycrystalline ferroelectric films,” *J. Appl. Phys.*, vol. 100, no. 6, p. 064105, 2006.

[93] B. Meyer and D. Vanderbilt, “Ab initio study of ferroelectric domain walls in $PbTiO_3$,” *Phys. Rev. B*, vol. 65, no. 10, p. 104111, Mar. 2002.

[94] P. Paruch, T. Giamarchi, T. Tybell, and J.-M. Triscone, “Nanoscale studies of domain wall motion in epitaxial ferroelectric thin films,” *J. Appl. Phys.*, vol. 100, no. 5, p. 051608, 2006.

[95] Y. Kim, Y. Cho, S. Hong, S. Bühlmann, H. Park, D.-K. Min, S.-H. Kim, and K. No, “Tip traveling and grain boundary effects in domain formation using piezoelectric force microscopy for probe storage applications,” *Appl. Phys. Lett.*, vol. 89, no. 17, p. 172909, 2006.

[96] B. J. Rodriguez, Y. H. Chu, R. Ramesh, and S. V. Kalinin, “Ferroelectric domain wall pinning at a bicrystal grain boundary in bismuth ferrite,” *Appl. Phys. Lett.*, vol. 93, no. 14, p. 142901, 2008.

[97] H. Chang, S. V. Kalinin, S. Yang, P. Yu, S. Bhattacharya, P. P. Wu, N. Balke, S. Jesse, L. Q. Chen, R. Ramesh, S. J. Pennycook, and A. Y. Borisevich, “Watching domains grow: In-situ studies of polarization switching by combined scanning probe and scanning transmission electron microscopy,” *J. Appl. Phys.*, vol. 110, no. 5, p. 052014, 2011.

[98] Y. Ivry, D. Chu, J. F. Scott, and C. Durkan, “Domains beyond the grain boundary,” *Adv. Funct. Mater.*, vol. 21, no. 10, pp. 1827–1832, May 2011.

[99] A. Pramanick, J. E. Daniels, and J. L. Jones, “Subcoercive cyclic electrical loading of lead zirconate titanate ceramics II: Time-resolved x-ray diffraction,” *J. Am. Ceram. Soc.*, vol. 92, no. 10, pp. 2300–2310, Oct. 2009.

[100] D. Damjanovic, “Contributions to the piezoelectric effect in ferroelectric single crystals and ceramics,” *J. Am. Ceram. Soc.*, vol. 88, no. 10, pp. 2663–2676, Oct. 2005.

[101] L. Q. Chen, “Phase-field method of phase transitions/domain structures in ferroelectric thin films: A review,” *J. Am. Ceram. Soc.*, vol. 91, no. 6, pp. 1835–1844, Jun. 2008.

[102] Y. L. Li, S. Y. Hu, Z. K. Liu, and L. Q. Chen, “Effect of substrate constraint on the stability and evolution of ferroelectric domain structures in thin films,” *Acta Mater.*, vol. 50, no. 2, pp. 395–411, Jan. 2002.

[103] L. Q. Chen and J. Shen, “Applications of semi-implicit Fourier-spectral method to phase field equations,” *Comput. Phys. Commun.*, vol. 108, no. 2–3, pp. 147–158, Feb. 1998.

[104] M. J. Haun, Z. Q. Zhuang, E. Furman, S. J. Jang, and L. E. Cross, “Thermodynamic theory of the lead zirconate-titanate solid solution system, part III: Curie constant and sixth-order polarization interaction dielectric stiffness coefficients,” *Ferroelectrics*, vol. 99, pp. 45–54, 1989.

[105] A. Tagantsev, “The role of the background dielectric susceptibility in uniaxial ferroelectrics,” *Ferroelectrics*, vol. 69, p. 321, 1986.

[106] Y. L. Li, S. Y. Hu, Z. K. Liu, and L. Q. Chen, “Effect of electrical boundary conditions on ferroelectric domain structures in thin films,” *Appl. Phys. Lett.*, vol. 81, no. 3, p. 427, 2002.

[107] P. Yu, S. Y. Hu, L. Q. Chen, and Q. Du, “An iterative-perturbation scheme for treating inhomogeneous elasticity in phase-field models,” *J. Comput. Phys.*, vol. 208, no. 1, pp. 34–50, Sep. 2005.

[108] S. Yokoyama, Y. Honda, H. Morioka, S. Okamoto, H. Funakubo, T. Iijima, H. Matsuda, K. Saito, T. Yamamoto, H. Okino, O. Sakata, and S. Kimura, "Dependence of electrical properties of epitaxial $Pb(Zr,Ti)O_3$ thick films on crystal orientation and $Zr/(Zr+Ti)$ ratio," *J. Appl. Phys.*, vol. 98, no. 9, p. 094106, 2005.

[109] G. A. Rossetti and A. G. Khachaturyan, "Inherent nanoscale structural instabilities near morphotropic boundaries in ferroelectric solid solutions," *Appl. Phys. Lett.*, vol. 91, no. 7, p. 072909, 2007.

[110] C. H. Peng, J.-F. Chang, and S. B. Desu, "Optical properties of PZT, PLZT, and PNZT thin films," *Mater. Res. Soc. Symp. Proc.*, vol. 243, pp. 21–26, 1992.

[111] W. Heywang, "Semiconducting Barium Titanate," *J. Mater. Sci.*, vol. 6, pp. 1214–1226, 1971.

[112] R. K. Vasudevan, M. B. Okatan, I. Rajapaksa, Y. Kim, D. Marincel, S. Trolier-McKinstry, S. Jesse, N. Valanoor, and S. V Kalinin, "Higher order harmonic detection for exploring nonlinear interactions with nanoscale resolution," *Sci. Rep.*, vol. 3, p. 2677, Jan. 2013.

[113] D. M. Marincel, H. Zhang, A. Belianinov, S. Jesse, S. V Kalinin, W. M. Rainforth, I. M. Reaney, C. A. Randall, and S. Trolier-McKinstry, "Domain pinning near a single grain boundary in tetragonal and rhombohedral Lead Zirconate Titanate films," no. In Press.

[114] D. Su, Q. Meng, C. A. F. Vaz, M.-G. Han, Y. Segal, F. J. Walker, M. Sawicki, C. Broadbridge, and C. H. Ahn, "Origin of 90° domain wall pinning in $Pb(Zr_{0.2}Ti_{0.8})O_3$ heteroepitaxial thin films," *Appl. Phys. Lett.*, vol. 99, no. 10, p. 102902, 2011.

[115] S. Jesse, B. J. Rodriguez, S. Choudhury, A. P. Baddorf, I. Vrejoiu, D. Hesse, M. Alexe, E. A. Eliseev, A. N. Morozovska, J. Zhang, L.-Q. Chen, and S. V Kalinin, "Direct imaging of the spatial and energy distribution of nucleation centres in ferroelectric materials.," *Nat. Mater.*, vol. 7, no. 3, pp. 209–15, Mar. 2008.

[116] B. J. Rodriguez, S. Choudhury, Y.-H. H. Chu, A. Bhattacharyya, S. Jesse, K. Seal, A. P. Baddorf, R. Ramesh, L.-Q. Q. Chen, and S. V. Kalinin, "Unraveling deterministic mesoscopic polarization switching mechanisms: Spatially resolved studies of a tilt grain boundary in bismuth ferrite," *Adv. Funct. Mater.*, vol. 19, no. 13, pp. 2053–2063, Jul. 2009.

[117] P. Dang and M. Grujicic, "An atomistic simulation study of the effect of crystal defects on the martensitic transformation in Ti - V BCC alloys," *Model. Simul. Mater. Sci. Eng.*, vol. 4, no. 2, pp. 123–136, Mar. 1996.

[118] S. M. Ueland and C. A. Schuh, "Grain boundary and triple junction constraints during martensitic transformation in shape memory alloys," *J. Appl. Phys.*, vol. 114, no. 5, p. 053503, 2013.

[119] N. Benedek, A. Chua, C. Elsässer, A. Sutton, and M. Finnis, "Interatomic potentials for strontium titanate: An assessment of their transferability and comparison with density functional theory," *Phys. Rev. B*, vol. 78, no. 6, p. 064110, Aug. 2008.

[120] M. Imaeda, T. Mizoguchi, Y. Sato, H.-S. Lee, S. D. Findlay, N. Shibata, T. Yamamoto, and Y. Ikuhara, "Atomic structure, electronic structure, and defect energetics in [001](310)Σ5 grain boundaries of $SrTiO_3$ and $BaTiO_3$," *Phys. Rev. B*, vol. 78, no. 24, p. 245320, Dec. 2008.

[121] T. Shimada, Y. Umeno, and T. Kitamura, "Ab initio study of stress-induced domain switching in $PbTiO_3$," *Phys. Rev. B*, vol. 77, no. 9, p. 094105, Mar. 2008.

[122] D. Damjanovic, F. Brem, and N. Setter, "Crystal orientation dependence of the piezoelectric d_{33} coefficient in tetragonal $BaTiO_3$ as a function of temperature," *Appl. Phys. Lett.*, vol. 80, no. 4, p. 652, 2002.

[123] T. Oikawa, M. Aratani, H. Funakubo, K. Saito, and M. Mizuhira, "Composition and orientation dependence of electrical properties of epitaxial $Pb(Zr_xTi_{1-x})O_3$ thin films grown using metalorganic chemical vapor deposition," *J. Appl. Phys.*, vol. 95, no. 6, p. 3111, 2004.

[124] E. Sun, R. Zhang, F. Wu, and W. Cao, "Complete matrix properties of [001](c) and [011](c) poled $0.33Pb(In_{1/2}Nb_{1/2})O_3$-$0.38Pb(Mg_{1/3}Nb_{2/3})O_3$-$0.29PbTiO_3$ single crystals.," *J. Alloys Compd.*, vol. 553, pp. 267–269, Mar. 2013.

[125] S. Zhang and F. Li, "High performance ferroelectric relaxor-$PbTiO_3$ single crystals: Status and perspective," *J. Appl. Phys.*, vol. 111, no. 3, p. 031301, 2012.

[126] S.-E. Park, S. Wada, L. E. Cross, and T. R. Shrout, "Crystallographically engineered $BaTiO_3$ single crystals for high-performance piezoelectrics," *J. Appl. Phys.*, vol. 86, no. 5, p. 2746, 1999.

[127] S. Wada, K. Yako, H. Kakemoto, T. Tsurumi, and T. Kiguchi, "Enhanced piezoelectric properties of barium titanate single crystals with different engineered-domain sizes," *J. Appl. Phys.*, vol. 98, no. 1, p. 014109, 2005.

[128] R. Xu, J. Karthik, A. R. Damodaran, and L. W. Martin, "Stationary domain wall contribution to enhanced ferroelectric susceptibility," *Nat. Commun.*, vol. 5, p. 3120, Jan. 2014.

[129] D. Wolf, "Correlation between structure, energy, and ideal cleavage fracture for symmetrical grain boundaries in FCC metals," *J. Mater. Res.*, vol. 5, no. 8, pp. 1708–1730, 1990.

[130] S. Aggarwal, S. Madhukar, B. Nagaraj, I. G. Jenkins, R. Ramesh, L. Boyer, and J. T. Evans, "Can lead nonstoichiometry influence ferroelectric properties of $Pb(Zr,Ti)O_3$ thin films?," *Appl. Phys. Lett.*, vol. 75, no. 5, p. 716, 1999.

[131] G. L. Brennecka and B. A. Tuttle, "Fabrication of ultrathin film capacitors by chemical solution deposition," *J. Mater. Res.*, vol. 22, no. 10, pp. 2868–2874, Jan. 2011.

[132] J. S. Cross, M. Tomotani, and Y. Kotaka, "$(Pb,La)(Zr,Ti)O_3$ film grain-boundary conduction with $SrRuO_3$ top electrodes," *Jpn. J. Appl. Phys.*, vol. 40, pp. L346–L348, 2001.

[133] G. L. Brennecka, C. M. Parish, B. A. Tuttle, L. N. Brewer, and M. A. Rodriguez, "Reversibility of the perovskite-to-fluorite phase transformation in lead-based thin and ultrathin films," *Adv. Mater.*, vol. 20, no. 8, pp. 1407–1411, Apr. 2008.

[134] M. J. Lefevre, J. S. Speck, R. W. Schwartz, D. Dimos, and S. J. Lockwood, "Microstructural development in sol-gel derived lead zirconate titanate thin films: The role of precursor stoichiometry and processing environment," *J. Mater. Res.*, vol. 11, no. 8, p. 2076, 1996.

[135] R. W. Schwartz, "Chemical solution deposition of perovskite thin films," *Chem. Mater.*, vol. 9, pp. 2325–2340, 1997.

[136] T. Tani and D. A. Payne, "Lead oxide coatings on sol-gel-derived lead lanthanum zirconium titanate thin layers for enhanced crystallization into the perovskite structure," *J. Am. Ceram. Soc.*, vol. 77, no. 5, pp. 1242–1248, 1994.

[137] R. L. Holman and R. M. Fulrath, "Intrinsic nonstoichiometry in single-phase $Pb(Zr_{0.5}Ti_{0.5})O_3$," *J. Am. Ceram. Soc.*, vol. 55, no. 4, pp. 192–195, 1972.

[138] A. D. Polli, F. F. Lange, and C. G. Levi, "Metastability of the fluorite, pyrochlore, and perovskite structures in the $PbO\text{-}ZrO_2\text{-}TiO_2$ system," *J. Am. Ceram. Soc.*, vol. 83, no. 4, pp. 873–881, 2000.

[139] V. V Prisedsky, V. I. Shishkovsky, and V. V Klimov, "High-temperature electrical conductivity and point defects in lead zirconate-titanate," *Ferroelectrics*, vol. 17, pp. 465–468, 1978.

[140] J. Chen, M. P. Harmer, and D. M. Smyth, "Compositional control of ferroelectric fatigue in perovskite ferroelectric ceramics and thin films," *J. Appl. Phys.*, vol. 76, no. 9, pp. 5394–5398, 1994.

[141] W. Liu and C. A. Randall, "Thermally stimulated relaxation in Fe-doped $SrTiO_3$ systems: II. Degradation of $SrTiO_3$ dielectrics," *J. Am. Ceram. Soc.*, vol. 91, no. 10, pp. 3251–3257, Oct. 2008.

[142] R. Wang, D. Fong, F. Jiang, M. Highland, P. Fuoss, C. Thompson, A. Kolpak, J. Eastman, S. Streiffer, A. Rappe, and G. Stephenson, "Reversible chemical switching of a ferroelectric film," *Phys. Rev. Lett.*, vol. 102, no. 4, pp. 2–5, Jan. 2009.

[143] G. Robert, D. Damjanovic, and N. Setter, "Preisach modeling of ferroelectric pinched loops," *Appl. Phys. Lett.*, vol. 77, no. 26, p. 4413, 2000.

[144] M. Kohli, P. Muralt, and N. Setter, "Removal of 90° domain pinning in (100) $Pb(Zr_{0.15}Ti_{0.85})O3$ thin films by pulsed operation," *Appl. Phys. Lett.*, vol. 72, no. 24, p. 3217, 1998.

[145] C. A. Randall, G. A. Rossetti, and W. Cao, "Spatial variations of polarization in ferroelectrics and related materials," *Ferroelectrics*, vol. 150, pp. 163–169, 1993.

[146] J. Han and W. Cao, "Interweaving domain configurations in [001]-poled rhombohedral phase $0.68Pb(Mg_{1/3}Nb_{2/3})O_3–0.32PbTiO_3$ single crystals," *Appl. Phys. Lett.*, vol. 83, no. 10, p. 2040, 2003.

[147] J. Yin and W. Cao, "Coercive field of $0.955Pb(Zn_{1/3}Nb_{2/3})O_3–0.045PbTiO_3$ single crystal and its frequency dependence," *Appl. Phys. Lett.*, vol. 80, no. 6, p. 1043, 2002.

[148] K. H. Härdtl and H. Rau, "PbO vapour pressure in the $Pb(Ti_{1-x}Zr_x)O_3$ system," *Solid State Commun.*, vol. 7, pp. 41–45, 1969.

[149] C. M. Parish, G. L. Brennecka, B. A. Tuttle, and L. N. Brewer, "Quantitative X-ray spectrum imaging of lead lanthanum zirconate titanate PLZT thin-films," *J. Am. Ceram. Soc.*, vol. 91, no. 11, pp. 3690–3697, Nov. 2008.

[150] T. N. Jackson, J. F. Degelormo, and G. Pepper, "Arsine ambient rapid thermal annealing," *Mater. Res. Soc. Symp. Proc.*, vol. 144, pp. 403–408, 1989.

[151] P. K. Baumann, G. R. Bai, S. K. Streiffer, O. Auciello, K. Ghosh, S. Stemmer, A. Munkholm, C. Thompson, D.-J. Kim, J.-P. Maria, and A. I. Kingon, "Ferroelectric and piezoelectric properties of MOCVD $Pb(Mg_{1/3}Nb_{2/3})O_3$-$PbTiO_3$ epitaxial thin films," *Mater. Res. Soc. Symp. Proc.*, vol. 596, pp. 517–522, 2000.

[152] D. D. Fong and C. Thompson, "in Situ synchrotron X-ray studies of ferroelectric thin films," *Annu. Rev. Mater. Res.*, vol. 36, no. 1, pp. 431–465, Aug. 2006.

[153] S. J. W. Price, "The decomposition of metal alkyls, aryls, carbonyls and nitrosyls," in *Comprehensive Chemical Kinetics*, C. H. Bamford, Ed. Amsterdam, The Netherlands: Tipper, C F H, 1972, p. 248.

[154] M. de Keijser and G. J. M. Dormans, "Modelling of organometallic chemical vapour deposition of lead titanate," *J. Cryst. Growth*, vol. 149, no. 3–4, pp. 215–228, Apr. 1995.

[155] E. J. Buckler and R. G. W. Norrish, “The vapour-pressure curve of tetraethyl-lead from 0° to 70°,” pp. 1567–1569, 1935.

[156] K. Budd, S. Dey, and D. A. Payne, “Sol-Gel processing of $PbTiO_3$, $PbZrO_3$, PZT, and PLZT thin films,” *Proc. Br. Ceram. Soc.*, vol. 36, pp. 107–21, 1985.

[157] J. F. Shepard Jr., P. J. Moses, and S. Trolier-McKinstry, “The wafer flexure technique for the determination of the transverse piezoelectric coefficient (dyl) of PZT thin films,” *Sensors Actuators A*, vol. 71, pp. 133–138, 1998.

[158] T. Mihara and H. Watanabe, “Electronic conduction characteristics of sol-gel ferroelectric $Pb(Zr_{0.4}Ti_{0.6})O_3$ thin-film capacitors: Part I,” *Jpn. J. Appl. Phys.*, vol. 34, no. 10, pp. 5664–5673, 1995.

[159] D. J. Keeble, B. Nielsen, A. Krishnan, K. G. Lynn, S. Madhukar, R. Ramesh, and C. F. Young, “Vacancy defects in $(Pb,La)(Zr,Ti)O_3$ capacitors observed by positron annihilation,” *Appl. Phys. Lett.*, vol. 73, no. 3, p. 318, 1998.

[160] M. V. Raymond and D. M. Smyth, “Defect chemistry and transport properties of $Pb(Zr_{1/2}Ti_{1/2})O_3$,” *Integr. Ferroelectr.*, vol. 4, no. 2, pp. 145–154, 1994.

[161] E. Cockayne and B. Burton, “Dipole moment of a Pb-O vacancy pair in $PbTiO_3$,” *Phys. Rev. B*, vol. 69, no. 14, p. 144116, Apr. 2004.

[162] W. L. Warren, G. E. Pike, D. Dimos, K. Vanheusden, H. N. Al-Shareef, B. A. Tuttle, R. Ramesh, and J. T. Evans, “Voltage shifts and defect-dipoles in ferroelectric capacitors,” *Mater. Res. Soc. Symp. Proc.*, vol. 433, pp. 257–266, 1996.

[163] K. Lee, K. S. Lee, and S. Baik, “Finite element analysis of domain structures in epitaxial $PbTiO_3$ thin films,” *J. Appl. Phys.*, vol. 90, no. 12, p. 6327, 2001.

[164] R. A. Wolf and S. Trolier-McKinstry, “Temperature dependence of the piezoelectric response in lead zirconate titanate films,” *J. Appl. Phys.*, vol. 95, no. 3, p. 1397, 2004.

[165] Y. Ehara, T. Oikawa, T. Yamada, and H. Funakubo, “Phase boundary shift by thermal strain in {100}-oriented epitaxial $Pb(Zr_xTi_{1-x})O_3$ film grown on CaF_2 substrates,” *Jpn. J. Appl. Phys.*, vol. 52, pp. 1–5, 2013.

[166] M.-T. Chentir, S. Utsugi, T. Fujisawa, Y. Ehara, M. Ishikawa, H. Morioka, T. Yamada, M. Matsushima, and H. Funakubo, “Small-strain (100)/(001)-oriented epitaxial $PbTiO_3$ films with film thickness ranging from nano- to micrometer order grown on $(100)CaF_2$ substrates by metal organic chemical vapor deposition,” *J. Mater. Res.*, vol. 28, no. 05, pp. 696–701, Feb. 2013.

[167] H. N. Al-Shareef and D. Dimos, “Leakage and reliability characteristics of lead zirconate titanate thin-film capacitors,” *J. Am. Ceram. Soc.*, vol. 80, no. 12, pp. 3127–3132, 1997.

[168] V. Chikarmane, C. Sudhama, J. Kim, J. Lee, A. Tasch, and S. Novak, "Comparative study of the perovskite phase microstructure evolution and electrical properties of lead airconate titanate thin-film capacitors annealed in oxygen and nitrogen ambients," *Appl. Phys. Lett.*, vol. 59, no. 22, pp. 2850–2852, 1991.

[169] V. V. Shvartsman and A. L. Kholkin, "Evolution of nanodomains in $0.9PbMg_{1/3}Nb_{2/3}O_3$-$0.1PbTiO_3$ single crystals," *J. Appl. Phys.*, vol. 101, no. 6, p. 064108, 2007.

Vita

Dan Marincel was born in St. Louis, MO on May 13th, 1988. He received summa cum laude in Ceramic Engineering from the Missouri University of Science & Technology in Rolla, MO in 2010. During his undergraduate career, he obtained research experience at the University of Missouri – Rolla, Sandia National Laboratories, and Iowa State University and decided he would like to pursue a research career. He began to work towards his doctorate in Materials Science and Engineering at the Pennsylvania State University in fall 2010. Dr. Marincel received his PhD in fall 2014.